

**THE TIMESCALES OF TRANSFORMATION ACROSS BRAIN STRUCTURES
IN THE THALAMOCORTICAL CIRCUIT**

A Thesis
Presented to
The Academic Faculty

by

Yi Juin Liew

In Partial Fulfillment
of the Requirements for the Degree
Doctor of Philosophy in the
Wallace H. Coulter Department of Biomedical Engineering

Georgia Institute of Technology
Emory University
Peking University
December 2022

Copyright © 2022 by Yi Juin Liew

THE TIMESCALES OF TRANSFORMATION ACROSS BRAIN STRUCTURES IN THE THALAMOCORTICAL CIRCUIT

Approved by:

Dr. Garrett Stanley, Advisor
Department of Biomedical Engineering
*Georgia Institute of Technology & Emory
University*

Dr. Michael Borich
Department of Emory Rehabilitation
Medicine & Biomedical Engineering
*Georgia Institute of Technology &
Emory University*

Dr. Annabelle Singer
Department of Biomedical Engineering
*Georgia Institute of Technology & Emory
University*

Dr. Yong Zhang
IDG/McGovern Institute for Brain
Research
PKU Health Science Center

Dr. Bilal Haider
Department of Biomedical Engineering
*Georgia Institute of Technology & Emory
University*

Dr. Xiaojie Duan
Department of Biomedical Engineering
*Georgia Institute of Technology &
Emory University & Peking University*

Date Approved: June 30, 2022

To my beloved parents – Fook Ming & Kwee Lan

ACKNOWLEDGEMENTS

PhD is a very personal journey. Throughout this time, I have received immeasurable support from many wonderful people to make this thesis my reality. I would like to first and foremost thank my advisor, Dr. Garrett Stanley who has given what felt like a mountain of support throughout all these years. Thank you for giving me all the essential training to do great science and the unbelievable guidance that has helped me through challenging times. I will always be grateful for all the coffee that we have shared together and the meaningful conversations that we have had over the years.

I would like to thank my thesis committee members, Dr. Michael Borich, Dr. Annabelle Singer, Dr. Bilal Haider, Dr. Yong Zhang, and Dr. Xiaojie Duan for their constant support and feedback in advancing my research. Their advice and recommendations have aided my growth and significantly improved the work presented here.

Over the years, I also had the opportunities to work with many outstanding scientists including Dr. Craig Forest, Dr. Gregory Holst, Dr. Will Stoy, Dr. Bo Yang from the Forest Lab, Dr. LinLin Lu, Dr. Xuefeng Fu from the Duan Lab (PKU), Dr. Yong Zhang from the PKU Health Science Center and Dr. Yao Li from Beijing Normal University. Interactions with them provided opportunities for me to learn highly technical experimental skills that have further increased the impact of my research.

I would like to personally thank the past and current members of the Stanley Lab including Dr. Clarissa Whitmire, Dr. Aurélie Pala, Dr. Peter Borden, Dr. Nathaniel (Caleb) Wright, Dr. Michael Bolus, Dr. He Zheng, Dr. Christian Waiblinger, Dr. Audrey Sederberg, Adam Willats, Elaida Dimwamwa, Adriano Borsa, Jacqueline Zhu, and David Weiss. I have received help from each of these lab members and this thesis would not be possible without their constant feedback. I would like to express special gratitude to my two mentors in the Stanley Lab, Dr. Clarissa Whitmire and Dr. Aurélie Pala, who taught me everything I know about performing research as a scientist and the role models that showed me how to face challenges head-on and have the discipline to pursue goals.

I would also like to take this opportunity to thank my close friends Andrew Toh, Zhen Kang Pang, Shea Chee Tan, Chun Qi Lim, Kelvin Tan, and Windy Ng, who are like my family here in Atlanta. Thanks for brightening up my weekends with lots of laughter and food. I would like to thank my OSU (Ohio State University) family: Yee Shwen Hoh, Anthony Phung, Jiunn Xhiong Boon, Samantha Ravindrasingam, Syn Dee Chua, and Yen Yee Piong for supporting me since the very beginning.

Throughout graduate school, there were moments when I had to deal with my deepest fears and insecurities. I am extremely grateful that I have my support system, Yong Cheng Soo (Michelle) and Jason Syu, who are always able to melt my anxieties away through conversations and encouragement. I am deeply indebted to Michelle for her unending

support at each step along the way. She had to endure my frustrations and doubts for the past 8 years yet never stop believing in me. I would like to express my deepest gratitude to my boyfriend, Jason Syu, who shares closely the ups and downs of this journey and always empowers me to tackle difficult things.

Above all, I owe this to my family, my parents who have made great sacrifices to support me mentally and financially to pursue a goal that is 15,081 km (9,371 miles) away from home, and my brothers and sisters (Yi Wen, Chun Sam, Zheng Yi, Siew Yee, and Yi Ling) who have been my biggest fans to see me succeed.

Lastly, I would like to recognize the sacrifices of the animals used in this research.

TABLE OF CONTENTS

ACKNOWLEDGEMENTS	IV
LIST OF FIGURES	IX
LIST OF SYMBOLS AND ABBREVIATIONS	XI
SUMMARY	XII
CHAPTER 1. INTRODUCTION	1
1.1 Transformation of sensory representation in the somatosensory pathway	2
1.1.1 Simultaneous, paired recording as a tool to study signalling across brain structures	3
1.1.2 The rodent vibrissae system as a model system to study transformation....	7
1.2 Thalamocortical processing in the primary sensory pathway	10
1.2.1 Transformation in the somatosensory thalamus.....	11
1.2.2 Transformation in the cortex	14
1.3 Changes in sensory representation	16
1.3.1 The timescales of thalamocortical synapses and corticocortical interaction	16
1.3.2 Mechanisms for adaptation and plasticity in the sensory system.....	17
1.4 Thesis Organization	20
CHAPTER 2. SYNAPTIC CONNECTIVITY IN THE THALAMOCORTICAL CIRCUIT 21	
2.1 Introduction	22
2.2 Methods	24
2.2.1 Animals	24
2.2.2 Animal preparation, surgery and craniotomies.	25
2.2.3 Electrophysiology.....	30
2.2.4 Whisker Stimulation.....	33
2.2.5 Post-mortem Histology	35
2.2.6 Analytical Methods	35
2.3 Results	41

2.3.1	Experimental workflow to establish paired recordings	44
2.3.2	Sensory response in topographically aligned VPM – S1 layer 4 regions..	49
2.3.3	Inferring connectivity in the context of a signal detection framework	52
2.3.4	Probabilistic measure of connectivity inference across brain structures in large-scale recordings	58
2.3.5	Data-length effect on monosynaptic connection inference	62
2.3.6	Thalamic synchrony effects on monosynaptic connection inference.....	67
2.4	Discussion.....	78

CHAPTER 3. MULTIPLE TIMESCALES OF RAPID SENSORY ADAPTATION IN THE THALAMOCORTICAL CIRCUIT..... 88

3.1	Introduction	90
3.2	Methods	93
3.2.1	Animals	93
3.2.2	Experimental Procedures.....	93
3.2.3	Anesthetized electrophysiology	96
3.2.4	Sensory Stimulus.....	98
3.2.5	Optogenetic Stimulation of Neural Activity	100
3.2.6	Post-mortem histology	101
3.2.7	Analytical Methods	101
3.3	Results	108
3.3.1	Diversity of adaptation dynamics in the thalamus and cortex	108
3.3.2	Signature of adaptation dynamics with multiple timescales in the thalamus and cortex.....	111
3.3.3	Role of thalamocortical synaptic depression and thalamic synchrony as adaptation mechanisms across timescales	116
3.3.4	Selective activation of synaptic depression of thalamocortical synapse removes multi-timescale adaptive dynamics	124
3.3.5	Adaptation over multiple timescales differentially modulates velocity tuning properties in the cortex	128
3.4	Discussion.....	136

CHAPTER 4. CONCLUSIONS AND FUTURE DIRECTIONS	141
4.1 Overview of thesis result	141
4.1.1 Key conditions for synaptic connectivity inference.....	142
4.1.2 Multiple timescales of adaptation in the TC circuit	143
4.1.3 Functional consequences of adaptation on detection and discrimination	145
4.2 Limitations.....	146
4.2.1 Stimulus paradigm limitations	146
4.2.2 Large-scale surveying of neuronal dynamics over time.....	147
4.2.3 Tracking of synaptic transmission using extracellular spiking	148
4.3 Speculations of findings & future directions	149
4.3.1 Decoupling thalamocortical interactions across timescales	149
4.3.2 Extension of findings to awake conditions	152
4.3.3 Results that are generalizable to larger context.....	154
4.4 Concluding remarks.....	155
APPENDIX A.....	157
REFERENCES.....	160

LIST OF FIGURES

Figure 1-1. Transformation of sensory representation in rhesus monkey.	3
Figure 1-2. Paired intracellular recording in hippocampal slice.....	6
Figure 1-3. Tracing of functional connections in cortical network using 4-shank silicon probes.....	7
Figure 1-4. Rodent somatosensory system.	10
Figure 1-5. Thalamic transformations of the lemniscal and paralemniscal pathways.....	13
Figure 1-6. Disynaptic feedforward inhibition in the thalamocortical microcircuit.	15
Figure 2-1. Experimental approach used to estimate monosynaptic connectivity between somatotopically-organized areas of the rodent somatosensory pathway.....	43
Figure 2-2. Targeting topographical alignment in vivo.	46
Figure 2-3. Monosynaptic connectivity inference using cross-correlation analysis.....	52
Figure 2-4. Evaluation of monosynaptic connection inference in the context of a signal detection framework.	55
Figure 2-5. Raw and shuffled-corrected cross-correlograms of ‘connected’ pairs in rat and mouse.	61
Figure 2-6. Connectivity matrix for topographically aligned simultaneous multi-site recordings.....	62
Figure 2-7. Data length dependence effect on monosynaptic connection inference.	64
Figure 2-8. Thalamic synchrony effect on monosynaptic connection inference.	70
Figure 2-9. Potential errors in connectivity inference due to thalamic synchrony.	75
Figure 2-10. Effect of data-length on monosynaptic connectivity inference for rat and mouse data.	82
Figure 2-11. Single-unit isolation quality of probe recordings during spontaneous and stimulus-driven conditions.....	83
Figure 3-1. Experimental approach and differential adaptation across VPM – S1.....	110
Figure 3-2. Adaptation dynamics of thalamic population in response to repetitive stimulation.....	113
Figure 3-3. Evolution of adaptation dynamics of cortical cells during exposure to repetitive stimulation.	115
Figure 3-4. Conceptual framework of potential mechanisms underlying cortical adaptation.	117
Figure 3-5. Adaptation reduces synaptic efficacy monotonically in synaptically connected thalamocortical neurons.	120
Figure 3-6. Adaptation reduces timing precision and pairwise synchrony in the thalamic population.	123
Figure 3-7. Optogenetic manipulation of short-term synaptic depression of thalamocortical synapse.	126
Figure 3-8. Contribution of short-term depression of thalamocortical synapse to cortical adaptation.	128
Figure 3-9. Adaptation degrades stimulus detection for ideal observer of cortical activity.	131
Figure 3-10 Adaptation modulates velocity sensitivity of cortical population.....	134

Figure 3-11. Adaptation enhances stimulus discrimination for ideal observer of cortical activity.....	135
---	-----

LIST OF SYMBOLS AND ABBREVIATIONS

VPm	Ventro-posteromedial nucleus of the thalamus
S1	Primary somatosensory nucleus
TC	Thalamocortical
POm	Posterior nucleus of the thalamus
ROC	Receiver operating characteristic
LFP	Local field potential
CC	Cross-correlation
SC	Shuffled-corrected
SEM	Standard error of the mean
SNR	Signal-to-Noise Ratio
FS	Fast Spiking (Inhibitory Interneuron)
RS	Regular Spiking Cell (Excitatory)
PSTH	Peri-stimulus time histogram
PCA	Principle Component analysis
PBS	Phosphate Buffered Saline
PW	Principal Whisker
AW	Adjacent Whisker

SUMMARY

Sensory processing requires reliable transmission of sensory information across multiple brain regions, from peripheral sensors, through sub-cortical structures, to sensory cortex, ultimately producing the sensory representations that drive perception and behavior. Despite decades of research, we do not yet have a mechanistic understanding of how neural representations are transformed across these critical brain structures. This is primarily due to the fact that what we know at the circuit level has been mainly derived from electrophysiological recordings targeted at single regions and upon gross anatomical connection patterns across brain regions without specific, precise knowledge of synaptic connectivity. To fill this gap in knowledge and to uncover how signaling changes across brain regions in response to changes in the sensory environment, this thesis work has two primary contributions. First, we developed a work-flow of topographic mapping and histological validation for extracellular multi-electrode recordings of neurons in the thalamocortical circuit in rodents, followed by a novel statistical approach for inferring synaptic connectivity across the brain regions. Specifically, we developed a signal-detection based classification of synaptic connectivity in the thalamus and S1 cortex, with an assessment of classification confidence that is scalable to the large-scale recording approaches that are emerging in the field. Utilizing this experimental and computational framework, we next investigated the neural mechanisms that underlie an important sensory phenomenon that emerges in this early sensory circuit: rapid sensory adaptation. While this phenomenon has been well-studied over very rapid timescales of hundreds of milliseconds, other studies suggest that longer time scales of 10's of seconds may also be relevant. Here,

we demonstrated that the thalamus and the thalamorecipient layer 4 excitatory and inhibitory neurons in S1 exhibit differential adaptation dynamics, and that the neuronal dynamics across these different regions and cell types show common signatures of multiple timescales in response to sensory adaptation. We characterized the adaptation profiles at the thalamocortical synaptic junction and further identified several mechanisms that potentially underlie the adaptation effects on the circuit dynamics, including synaptic depression of the thalamocortical synapse in identified monosynaptically connected thalamic and cortical neurons, and changes in spike timing and synchronization in the thalamic population. Using optogenetic approaches to manipulate thalamic firing, we found evidence that suggests thalamic synchrony plays a bigger role in adaptive dynamics of longer timescales. These mechanisms together mediate a dynamic trade-off in the theoretical detectability and discriminability of stimulus inputs. These results suggest that adaptation of the thalamocortical circuit across timescales results from a complex interaction between distinct mechanisms, and notably the engagement of different mechanisms can shift depending on the timescale of environmental changes.

CHAPTER 1. INTRODUCTION

How does sensation arise, and what does it mean when we sense something in our surroundings? Our interaction with the world begins when our biological sensors detect a stimulus at the periphery and transduce the physical energy into a neural code that is hierarchically relayed across the brainstem, thalamus, and cortex for cognition and decision-making (Kandel et al. 2000). As sensory information progresses through these different stages of processing in the pathway, the neural representation becomes more abstract, and explodes with complexity at the thalamocortical (TC) junction (Sherman and Guillery 1996). Surprisingly, despite decades of research, we still do not have a clear understanding of the neural mechanisms that underlie sensation. Additionally, much of what we know at this level primarily comes from studies focusing on a single brain region at a time. As new electrophysiological tools emerge for simultaneous recording from neuronal populations spanning multiple brain regions (Jun et al. 2017), this presents unique opportunities to study signaling across brain structures and ask how sensory signals might be modulated and altered along the pathway.

Therefore, the objectives of this thesis were to characterize the response properties of neuronal populations from multiple brain regions to understand the dynamical interactions between them and further investigate the adaptive evolution of these response dynamics across temporal scales. With that in mind, we performed simultaneous, multi-site extracellular recordings in the TC circuit and developed the experimental and computational tools that establish rules of connectivity between the thalamus and cortex within a signal-detection/statistical framework (Chapter 2). Furthermore, utilizing the

advanced techniques we have developed, we further unpacked one of the most fundamental brain computations, sensory adaptation, and its effects on signal transformation across the thalamocortical junction (Chapter 3). Although this work was focused on the tactile pathway in rodents, we believe the methodology and general principles of the neural mechanisms documented in this thesis are generalizable to other sensory modalities and species, given the commonality of brain function and neural processing. In the next section, I have outlined the pertinent background materials for understanding this work.

1.1 Transformation of sensory representation in the somatosensory pathway

As information about the external world is transformed into electrical signals and propagated along different stages of the early sensory pathway, the transformation of neural representation has been shown to become increasingly complex (Kandel et al. 2000). This is clearly demonstrated in a classic rhesus monkey study conducted by Phillips et al. (1988) where they presented embossed letters to the fingertips of the monkey with a rotating drum and compared neural spiking response from the peripheral afferent fibers and the primary somatosensory cortex (Figure 1-1). They found that the fine spatial details of the letters were preserved at the peripheral sensors (specifically slow-adapting type 1 fiber), but the representation becomes much more abstract at the level of primary somatosensory cortex and there was a greater diversity in responses across different cortical neurons. This suggests that information about a physical stimulus is deconstructed, processed, and transformed across different brain structures to form distinct neural representations at higher processing areas that ultimately lead to perception and behavior. Therefore, the ability to analyze patterns of activity across neuronal populations of multiple stages of the

early sensory pathway is the cornerstone of understanding neural mechanisms underlying sensory processing (Muniak et al. 2007; Phillips et al. 1988; Salinas et al. 2000).

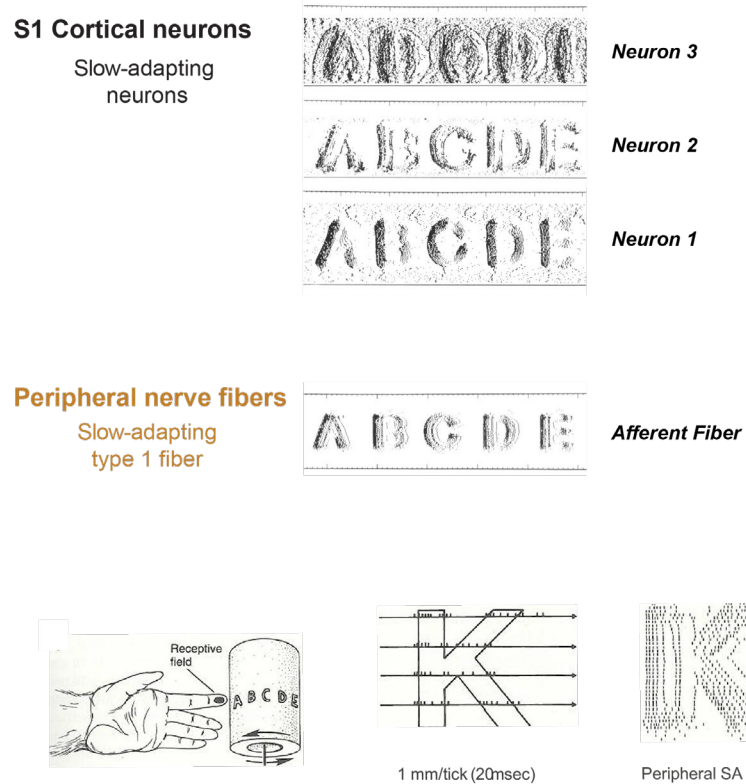


Figure 1-1. Transformation of sensory representation in rhesus monkey.

Every letter was presented repeatedly to construct a 2-dimensional plot of the spikes (represented in vertical bars from left to right here), evoked in response to different alphabets. Shown is an example of the spiking response with respect to the letter K in the periphery. Afferent fiber in the periphery can convey the fine spatial details of the letters but the representation becomes much more abstract when it gets to cortex. Note the greater diversity in response across different cortical neurons. Figure adapted from (Phillips et al. 1988).

1.1.1 Simultaneous, paired recording as a tool to study signalling across brain structures

Despite the fact that every brain function relies on signaling across brain regions, what we know about the brain comes from studies that mostly record from a single brain

region at a time. To address this, in the past decade, there were many efforts dedicated to discovering tools that would track brain signaling at different scales. The Human Connectome Project was launched by the NIH in 2009, and the goal was to construct a map of the complete structural and functional connections in the human brain (Van Essen et al. 2012). As a continued effort, in 2013, the white house launched the Brain Initiative Project and the mission was to accelerate development of new technologies to track neural signaling at the network level as well as the cellular level that will enable the study of dynamic interactions between individual cells and the neural networks (Insel et al. 2013). These government initiatives have yielded a recent explosion of tools and research that enables better insight about communications across brain structure. At the macro level, fMRI studies have provided many useful mappings of functional connection between brain regions like the thalamus and cortex. However, these studies are at a relatively coarse spatial and temporal scale, largely correlational, and there are many important aspects of signaling that cannot currently be gained from this approach. For example, underlying all signaling pathways, the majority of connections are cell-type specific and are known to play different functional roles in the circuit. Furthermore, the downstream brain regions can be highly sensitive to aspects of the projecting inputs, such as timing and synchrony, which is lost in the macroscopic measures. To establish causality and understand how one brain region affects the other, it is therefore imperative to track long range circuits like the thalamocortical (TC) pathway with high specificity with single-cell resolution of the neuronal populations. Our work in Chapter 2, which is also supported by the NIH Brain Initiative Project, is dedicated to address this gap in knowledge.

Traditionally, simultaneous, paired recordings are used to study information flow at the most fundamental level, specifically tracking synaptic transmission across a pair of connected neurons either within or across neuronal population (Debanne et al. 2008). Paired, whole-cell recordings (shown in Figure 1-2) of a neuronal pair enable causal investigation of the effect of presynaptic firing on the postsynaptic neuron. Note that this is the gold standard for tracking neural signaling at the finest resolution, where the subthreshold activity of a single neuron can be manipulated and monitored. However, given the complexity of targeting a pair of neurons that form a synaptic connection with each other, this kind of experiment is typically performed on brain slices or organoids, and a comparatively small number of laboratories can achieve this in the intact brain, in-vivo. With the advent of better electrophysiological techniques, however, paired recording can also be achieved with silicon probe recordings within and across neuronal populations (shown in Figure 1-3). From extracellular recordings one can infer synaptic connections by using statistical inference based on the coactivation probability of neuronal firing across neuronal pairs, through analysis of spike cross-correlograms. At the expense of precise tracking of subthreshold activity, the ability to perform large-scale recordings using extracellular techniques offers monitoring of neuronal spiking activity across a neural ensemble and a more uniform and unbiased sampling of key players in brain signaling. While some methods exist in this direction, they are ad-hoc and have not been rigorously developed. In this work, I have established a framework to specifically optimize paired, extracellular recordings in the feedforward thalamocortical (TC) pathway, detailed in Chapter 2.

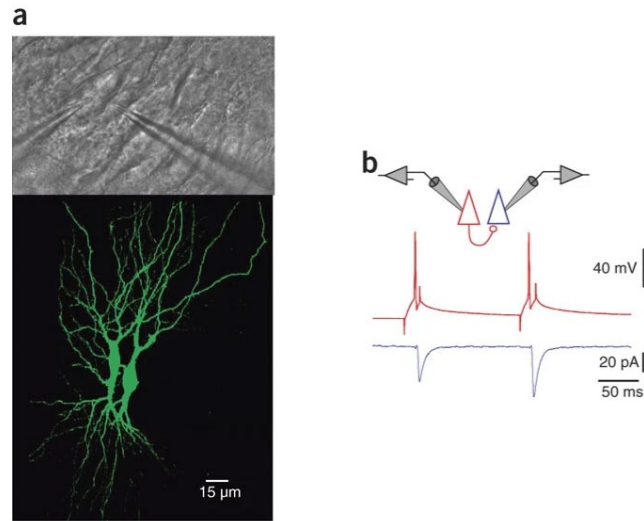


Figure 1-2. Paired intracellular recording in hippocampal slice.

(a) Paired whole-cell recordings via patch pipettes in a slice culture visualized using differential interference contrast (DIC) optics in combination with infra-red illumination (IR-DIC) of the hippocampal CA3 region (top) and confocal reconstruction of neuronal pairs filled with biocytin (bottom). (b) Action potentials triggered in the presynaptic neuron (shown in red) and the effect on the postsynaptic neurons can be detected as electrical currents (shown in dark blue) as voltage-clamp signal. Figure adapted from (Debanne et al. 2008).

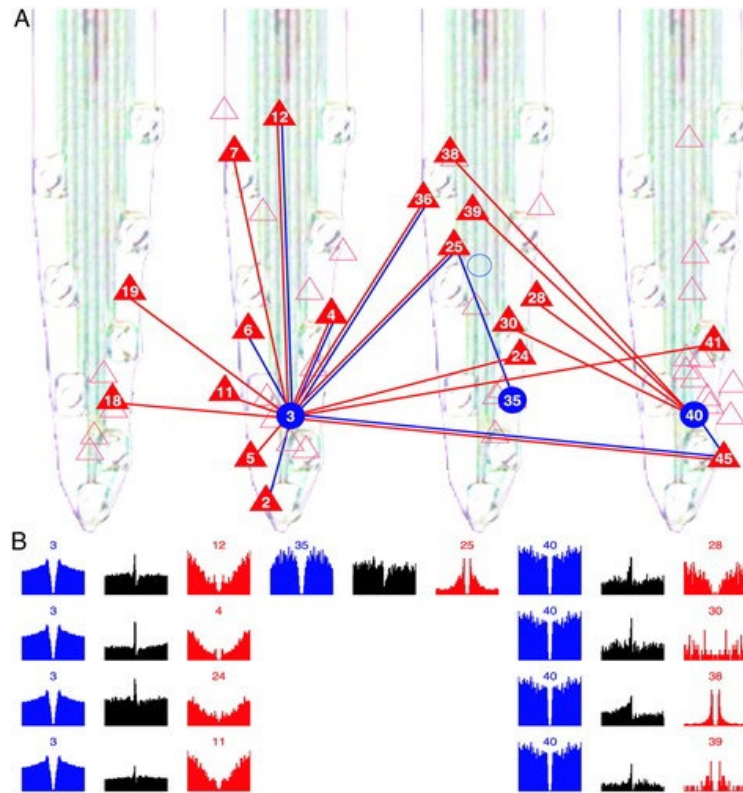


Figure 1-3. Tracing of functional connections in cortical network using 4-shank silicon probes.

(a) Multiple cells can be recorded simultaneously at single-cell resolution. Red triangles are denoting participating cortical pyramidal cells and blue filled circles are denoting interneurons. Horizontal lines connecting cells are depicting putative monosynaptic connections between neuronal pairs. (b) Autocorrelograms (blue and red) and cross-correlograms (black) constructed using spiking activities from cells shown in (a). Figure adapted from (Barthó et al. 2004).

1.1.2 The rodent vibrissae system as a model system to study transformation

Rodents have developed a sense of touch via their large facial whiskers to navigate through and investigate their environments, similar to ways humans palpate objects in the sensory environment with fingertips. While rodents also have access to other senses for navigation, like vision, smell, and other aspects of somatosensation like footpad mechanosensory, it has been shown that a particularly important sensory modality for them

is the vibrissa system. When a sensory stimulus is detected, sensory information is conveyed from the periphery sensors (whiskers) to the brainstem, thalamus and eventually primary somatosensory cortex (S1), parallel to stages of processing in the human somatosensory pathway. Due to high ethological relevance of the rodent whisker system, the representation of the largest whiskers (macro vibrissa) is enlarged relative to other body parts and each whisker is discretely represented at every processing stage of the pathway and arranged in a topographically-aligned manner (Kandel et al. 2000). This provides a powerful model system for studying sensory processing and transformation across brain structures because there are populations of neurons at each level that respond principally to a single whisker. Additionally, there are extensive studies in the past several decades that have explored the neural circuitry of this pathway, providing a rich database and wealth of knowledge about the anatomy and projections from and to other brain areas (Petersen 2007). It has been found that there are at least three parallel thalamocortical pathways that transmit whisker-related sensory information from the periphery to cortex, specifically the lemniscal, paralemniscal and extralemniscal pathways (see Figure 1-4) and these pathways encode different attributes of the whisker inputs (see review from Adibi (2019)). The lemniscal pathway is the major pathway through which the touch signal is relayed to the cortex and conveys a combination of touch and whisking (active movement of whiskers) signals. In contrast, the paralemniscal pathway conveys primarily whisking signals for sensory-motor coordination and the extralemniscal pathway conveys object location (Yu et al. 2006). Notably, the thalamocortical targets for these pathways are distinct, summarized below:

1. Lemniscal Pathway: ventral posterior medial nucleus of the thalamus (VPMdm) (also referred to as barreloids) project to cortical barrel columns in layer IV and sparsely to Layer VI in SI.
2. Paralemniscal Pathway: posterior medial nucleus (POm) of the thalamus projects to the following cortical areas: layer I and Va of SI, the septal regions, SII, MI and superior colliculus.
3. Extralemniscal Pathway: ventral posterior medial nucleus of the thalamus (VPMvl) projects to SII and the septal regions of SI cortex.

In this project, we focused on the lemniscal thalamocortical targets where projections from the ventral posterior medial (VPm) nucleus of the thalamus ('barreloid') form one-to-one mapping to discrete clusters called 'barrels' in layer 4 of S1 cortex (Petersen 2007). Additionally, it is known that VPm thalamic projections to the barrel cortex are highly convergent, with an overall connection probability of 63% for contacting inhibitory neurons, also known as fast-spiking units (FSU) and 37% for contacting excitatory, regular-spiking units (RSU) (Bruno and Simons 2002). Note that posterior medial nucleus (POm) of the thalamus (paralemniscal) will also be frequently mentioned in Chapter 2 and 3 because it is important to identify the thalamic origins of the recorded neurons for precise targeting of the circuit.

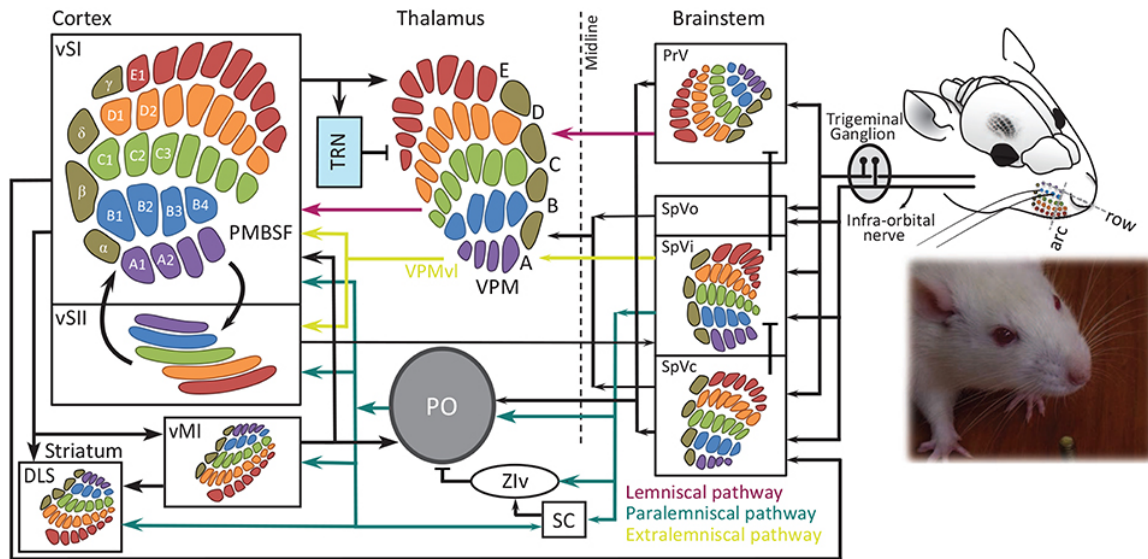


Figure 1-4. Rodent somatosensory system.

Whisker information reaches cortex in three parallel pathways: 1) Lemniscal, 2) Paramlemniscal, and 3) Extralemniscal. These pathways encode different aspects of the sensory signals. Figure adapted from (Adibi 2019). Partial original caption: “Each whisker is identified by a unique letter-number combination corresponding to its row (A to E from dorsal to ventral) and arc (identified by numbers 1, 2 and etcetera from caudal to rostral), with α , β , γ , and δ straddlers between rows. Colors indicate rows. Barrel, barreloid and barrelets are redrawn from Durham and Woolsey (1984). PMBSF, posterior-medial barrel sub-field; PO, posterior thalamic nucleus; PrV, principal trigeminal nucleus; SC, superior colliculus; SpVi, spinal trigeminal nuclei pars interpolaris; SpVo, pars oralis; SpVc, pars caudalis; TRN, thalamic reticular nucleus; VPM, ventro-posterior medial nucleus; vMI, vibrissal primary motor cortex; vSI, vibrissal primary somatosensory cortex; vSII, secondary somatosensory cortex with the somatotopic map from Benison et al. (2007); DLS, dorsolateral striatum; Zlv, ventral zona inserta.”.

1.2 Thalamocortical processing in the primary sensory pathway

For nearly every sensory pathway, the thalamocortical junction represents a critical node of early sensory processing. Except for olfaction, all sensory information passes through the thalamus before reaching the primary sensory cortex, suggesting the canonical nature of this circuit motif. In the early processing pathway, sensory cortex is well-known for its role in information processing that gives rise to cognition and behavior. However,

recent work has found that thalamus plays an important role in cortical function. Rather than acting as a simple relay station where sensory signals have to go through before reaching the cortex, it has been postulated that thalamus can dynamically gate what kind of information that reaches the cortex (Poulet et al. 2012; Sherman and Guillery 1996). There are several lines of evidence that demonstrate the key role of thalamus in regulating information transmission along the pathway. Previous studies showed that thalamus can operate in distinct firing modes i.e. burst vs tonic firing (Alitto et al. 2005; Denning and Reinagel 2005; Fanselow Erika et al. 2001; Guido et al. 1992; Lesica and Stanley 2004; Reinagel et al. 1999; Sherman 2001; Steriade and Llinás 1988; Swadlow 1989; Wang et al. 2007; Whitmire et al. 2021; Whitmire et al. 2016), as well as changing its response amplitudes (Ahissar et al. 2000a) and spike timing (Butts et al. 2007; Pinto et al. 2000; Reinagel and Reid 2000; Temereanca et al. 2008) in response to stimulus statistics. Additionally, temporal properties of thalamic population spiking have also been shown to be important for establishing feature selectivity in cortex (Wang et al. 2010). Taken together, this strongly suggests that the thalamocortical circuit plays a fundamental role in sensory perception, and hence has been chosen as the focus of this work.

1.2.1 Transformation in the somatosensory thalamus

In the rodent somatosensory thalamus, studies have shown that lemniscal and paramlemniscal pathways form parallel processing pathways to decode spatial and temporal whisker information. In the lemniscal pathway, as shown in Figure 1-5, neuronal responses exhibit a time-locked response to repetitive stimuli, which enables encoding for spatial whisker info and temporal information of high frequency stimuli. In contrast, the

less temporally precise paralemniscal system encodes low-frequency, temporal whisker information (Ahissar et al. 2000b). Notably, despite major differences in patterns of activity between the two pathways, neural representations of the thalamocortical neurons generally change in the form of spike counts ('rate code'), and/or latencies ('temporal code') and these two attributes tend to interact dynamically in the 'response window' to shape how information is transmitted to the downstream postsynaptic targets. In the somatosensory pathway, it has been shown that thalamic gating can be achieved by varying the number of spikes elicited in response to a given stimulus, the temporal properties of those spikes, and the synchrony of firing across thalamic neurons (Whitmire and Stanley 2016). Furthermore, the dynamical nature of this gating has been demonstrated in response to repetitive sensory stimulation (Bruno and Sakmann 2006; Wang et al. 2010) and thalamic state-dependent processing (Beierlein et al. 2002; Borden et al. 2022; Swadlow and Gusev 2001; Whitmire et al. 2016).

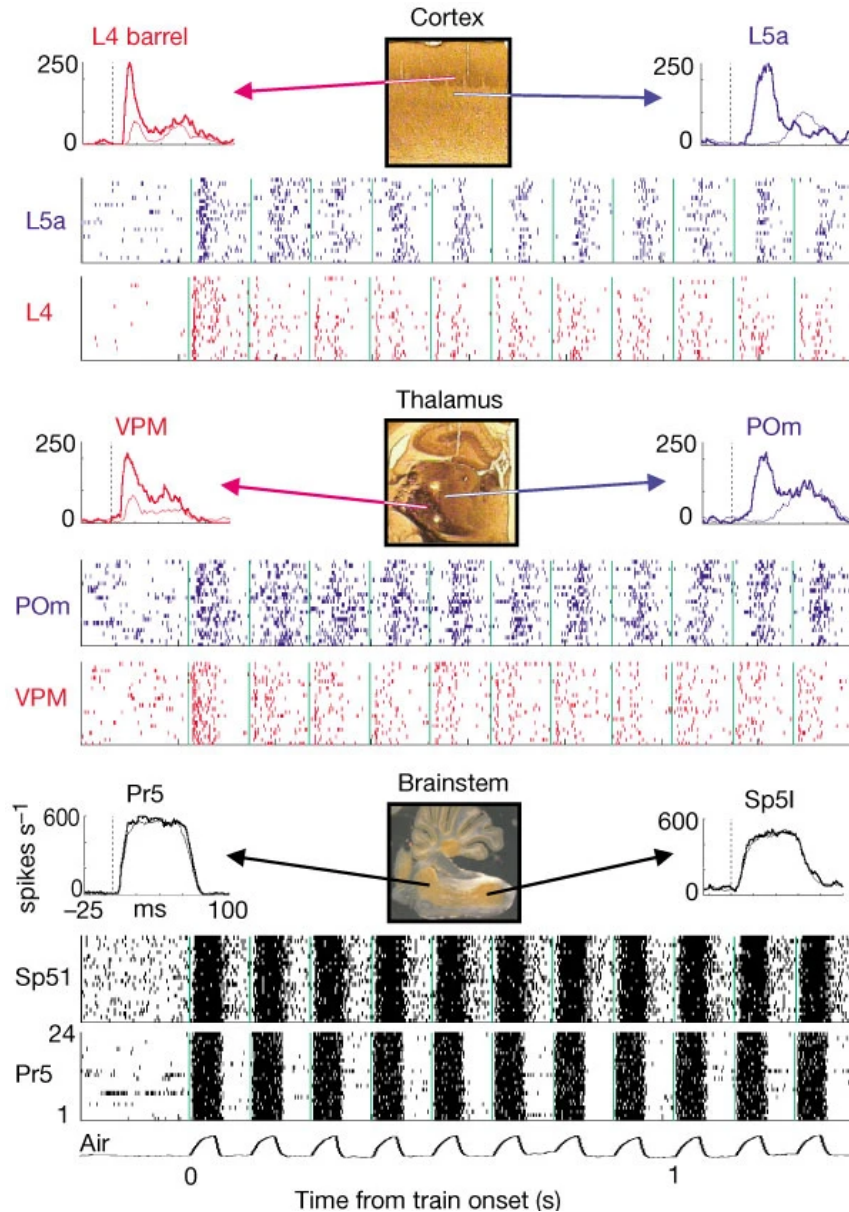


Figure 1-5. Thalamic transformations of the lemniscal and paralemniscal pathways. Raster plots (24 trials each) of spiking activities from the brainstem, thalamus and cortex along both pathways. Neural activity at the brainstem level appeared to convey afferent signals from the periphery but transformations were obvious at the level of thalamus (i.e., change in firing rate and response latencies) and cascaded to the level of cortex. Figure adapted from (Ahissar et al. 2000a).

1.2.2 Transformation in the cortex

In the lemniscal pathway, timing of the sensory stimulus is a fundamental aspect to decode and likely to be essential for proper tactile discrimination. In order to keep precise spike timing, it has been demonstrated that cortex engages disynaptic feedforward inhibition to maintain sensitivity to timing of thalamic inputs (Gabernet et al. 2005b; Hull and Scanziani 2007). When thalamic inputs enter the cortex, both excitatory and inhibitory cells in layer 4 of S1 receive direct inputs from VPM thalamus, with inhibitory cells projecting back to the same excitatory neurons. Since the onset of feedforward inhibition is delayed by one synapse, the excitatory neurons have a narrow window to integrate thalamic inputs before inhibition is activated. As previously mentioned, thalamic convergence onto RSUs is two-fold less than FSUs (Bruno and Simons 2002), therefore they receive less driving inputs from the thalamus and are highly susceptible to the robust feedforward inhibition. This setup, however, allows RSUs to act as coincidence detectors (Gabernet et al. 2005b).

Additionally, studies have shown that excitatory (RSUs) and inhibitory (FSUs) barrel neurons exhibit distinctive response properties from each other as well as from the thalamic neurons (Bruno and Simons 2002; Khatri et al. 2004; Simons and Carvell 1989). This is likely due to a number of factors such as the different biophysical properties that can readily account for differences in overall firing rates (Angulo et al. 1999; Kawaguchi and Kubota 1993), differences in connection probabilities across thalamocortical cells that can contribute to differences in receptive field properties, and the complex interactions between

the thalamic and cortical cell across different stimulus conditions that underlie thalamocortical transformation.

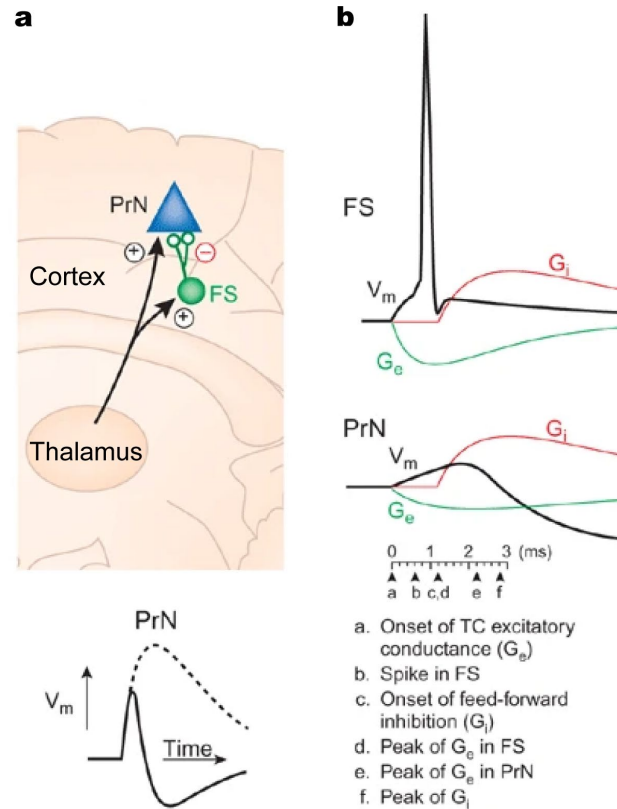


Figure 1-6. Disynaptic feedforward inhibition in the thalamocortical microcircuit.

(a) Emergence of feedforward inhibition is thalamic driven. Thalamic inputs are distributed to both excitatory (principal cells, PrN) and inhibitory (fast-spiking, FS) neurons. In turn, fast-spiking interneurons make synapses onto PrNs that evoke a delayed inhibition in PrN cells. (b) The millisecond time frame of cortical sensory processing. Original caption from figure: Time 0: thalamocortical afferents excite fast-spiking cells and PrNs. The activation of a large and fast excitatory postsynaptic conductance (G_e) onto fast-spiking neurons leads to a rapid depolarization of the membrane potential (V_m). At around 0.6 ms, this generates a spike. Meanwhile, V_m rises more slowly in PrNs as a result of a slower G_e (measured at the soma) and longer membrane time constant. Time 1.2 ms: GABA released from fast-spiking interneurons initiates a GABAA receptor-mediated conductance (G_i) in PrNs. Time 2.7 ms: G_i reaches its peak. By counteracting G_e , G_i hyperpolarizes V_m to conclude the standard EPSP-IPSP sequence. If PrNs do not reach threshold for spike generation before the onset of the IPSP, they likely never will (at least in the immediate future). Figure adapted from (Hull and Scanziani 2007).

1.3 Changes in sensory representation

1.3.1 *The timescales of thalamocortical synapses and corticocortical interaction*

As sensory information is transmitted from the periphery to cortex, both intracortical recurrent connections and the direct projection from thalamic afferents to the cortex are known to play key roles in sensory processing. For the context of this project, we will review relevant timescales for signaling across the thalamocortical synapse and for integration at the level of the cortex. Studies have shown that sensory signals conveyed to the cortex are modulated by the window of integration of the recipient cortical target. This temporal window for integration of thalamic inputs is reported to vary within a 1-10 ms range, dictated by dynamics of feedforward inhibition (Gaberet et al. 2005a). When information is transmitted through the thalamocortical synapse, repetitive whisker stimulation can induce short-term synaptic depression in the pathway. It has been shown that short-term synaptic depression of the thalamocortical synapse plays a critical role in mediating cortical adaptation of the downstream target (Chung et al. 2002). Thalamocortical synaptic depression recovers with a time constant of ~ 5 s in response to a 4Hz, 2.5s adapting whisker stimulus. However, it has also been reported that ongoing stimulation engages diverse synaptic dynamics within the thalamocortical synapse (Díaz-Quesada et al. 2014), suggesting that differential synchrony of the thalamus could also affect sensory transformation at this stage. Recent work from Reinhold et al. (2015) demonstrated that intracortical amplification dominates sensory encoding at a longer timescale (~ 250 ms), consistent with previous studies. However, more importantly, they demonstrated that thalamic inputs are required to sustain sensory evoked responses in the

visual cortex over timescales longer than a few tens of milliseconds. We will not examine corticothalamic feedback directly within the scope of this proposed work, however we note that corticothalamic (CT) feedback could also play a role in modulating sensory processing and there is some evidence that shows that cortical feedback enhances thalamic activity at the range of 3-10 ms relative to onset of thalamic responses upon CT-activation and could have long-lasting effect up to 50 ms or longer (Temereanca and Simons 2004). Taking all of this together, fast and slow alterations in synaptic and circuit dynamics of thalamocortical, corticocortical, and corticothalamic synapses affect thalamic and cortical sensory responses immensely and one of the major goals of this proposed work is to provide a framework to identify and disentangle some of these interactions in sensory processing. For the scope of this work, we will place major emphasis on the role of thalamus in mediating sensory adaptation in the downstream cortex.

1.3.2 Mechanisms for adaptation and plasticity in the sensory system

Adaptation is a well-studied phenomenon in the nervous system and is ubiquitous across sensory pathways including the visual, somatosensory and auditory system. Sensory adaptation is typically defined as a reduction of response after constant, repetitive exposure to a sensory stimulus and this change in function can happen at disparate timescales (Wark et al. 2007). Rapid sensory adaptation, sometimes also referred to as a transient form of plasticity, happens at a timescale ranging from milliseconds to seconds. Mechanisms that were proposed to underlie this phenomenon includes intrinsic mechanisms of a single neuron, inheritance from presynaptic neurons, and those generated from the local recurrent network (Whitmire and Stanley 2016). In the context of sensory encoding, these

mechanisms are thought to be associated with some important functions such as rescaling of input-output function via a neuron's intrinsic mechanism; shift in feature selectivity of postsynaptic neurons due to partial adaptation of synaptic drive from the presynaptic population (Chance and Abbott 2001; Chung et al. 2002); sharpened temporal or spatial receptive field properties as well as normalization of input-output functions due to differential adaptation within the local recurrent network (del Mar Quiroga et al. 2016; Dragoi et al. 2000; Felsen et al. 2002; Gutnisky and Dragoi 2008). For a detailed review of rapid sensory adaptation, see Whitmire and Stanley (2016). Despite the change in function, these effects are assumed to be short-lived and reversible.

Beyond rapid adaptation, both short and long-term synaptic plasticity generally involves longer lasting and more complex changes in the circuitry. Sensory cortical plasticity has been prominently studied, perhaps most commonly in the context of sensory map plasticity given the topographic nature of primary sensory areas. The sensory deprivation paradigm has been frequently used to study map plasticity and is known to engage a Hebbian form of plasticity (LTP and LTD) that involves response depression to deprived inputs and potentiation of spared inputs (Feldman 2009). In the context of this project, we will review some use-dependent plasticity across short and longer-term timescales. Characterization of activity-dependent strengthening of cortical synapses often involves LTP and this has been found in adult L4-L2/3 excitatory synapses in S1 (Hardingham et al. 2003) and appears to be NMDA-dependent. Both presynaptic and postsynaptic mechanisms have been implicated to regulate cortical synapses, which includes insertion of GluR1-containing AMPA receptors into synapses (Malinow and Malenka 2002; Takahashi et al. 2003). In primary visual cortex, tetanic stimulation

delivered directly to dLGN for 1 hour readily induced NMDA receptor-dependent LTP in an adult rat in vivo (Heynen and Bear 2001). Activation of thalamocortical synapses in an adult slice preparation of the mouse somatosensory system, on the contrary, has been found to show very little recruitment of NMDAR-mediated current in L4, and this was suggested to be blocked by the maturation of the inhibitory network (Agmon and O'Dowd 1992). Tremendous work had focused on LTP and LTD mechanisms within the excitatory network in the past decades, however plasticity in the GABAergic inhibitory circuit is receiving growing attention. Additionally, the balance of excitation and inhibition in cortical networks is shown to be critical for shaping the receptive field of cortical cells (Lee et al. 2012; Wilent and Contreras 2005). Within the context of this work, this implies that plasticity of an inhibitory network with distinct dynamics could fundamentally affect the expression of receptive fields in target neurons at distinct timescales. Consistent with this view, repeated activation of sensory input for an extended period of time (24 hours and more) is demonstrated to cause an increase in GABAergic synapses on spines in stimulated L4 cells (Knott et al. 2002; Welker et al. 1992). Additionally, there are also other forms of input-specific synaptic plasticity such as heterosynaptic and homosynaptic plasticity that are known to act as a rapid compensatory mechanism to ensure firing homeostasis within the network (Chistiakova et al. 2014). Taken together, these findings demonstrate that manifestation of adaptation at distinct stages of the sensory pathway can be a result of interaction between multiple mechanisms. We believe that quantification of adaptation effects at the timescales proposed in this work would allow us to examine some of the important interactions between mechanisms across timescales that underlie thalamocortical processing.

1.4 Thesis Organization

As we interact with the world, our brains adapt and change as a function of our experience, and this involves complex circuitry and communication across many different brain areas. In this thesis, I used the rodent vibrissa pathway as a model system to investigate the timescales of transformation across brain structures, focusing on the thalamocortical circuit which is known to play a central role in cognition and behavior. In Chapter 2, I develop the experimental methodology to perform simultaneous, multi-site recording in the topographically aligned thalamocortical (TC) circuit and establish a novel analytical framework to assess monosynaptic connectivity in those regions, laying the foundation to study transformation across brain structures. In Chapter 3, I first establish the functional timescales of sensory adaptation in the thalamus and cortex. I then assess the dynamic adaptive changes in distinct synaptic and neuronal mechanisms in the pathway and use optogenetic manipulation to causally disentangle the effects of distinct mechanisms on sensory adaptation. Lastly, I quantify the implications to theoretical detection and discrimination performance using an ideal observer analysis of extracellular electrophysiology. Finally, in Chapter 4, I discuss the significance and limitations of the research, outline some of the remaining gaps in knowledge, and identify future directions for this work.

CHAPTER 2. SYNAPTIC CONNECTIVITY IN THE THALAMOCORTICAL CIRCUIT

This chapter was originally published as an article in Journal of Neurophysiology and is presented with only minor stylistic changes ¹.

As the tools to simultaneously record electrophysiological signals from large numbers of neurons within and across brain regions become increasingly available, this opens up for the first time the possibility of establishing the details of causal relationships between monosynaptically connected neurons and the patterns of neural activation that underlie perception and behavior. Although recorded activity across synaptically connected neurons has served as the cornerstone for much of what we know about synaptic transmission and plasticity, this has largely been relegated to ex vivo preparations that enable precise targeting under relatively well-controlled conditions. Analogous studies in vivo, where image-guided targeting is often not yet possible, rely on indirect, data-driven measures, and as a result such studies have been sparse and the dependence upon important experimental parameters has not been well studied. Here, using in vivo extracellular single-unit recordings in the topographically aligned rodent thalamocortical pathway, we sought to establish a general experimental and computational framework for inferring synaptic connectivity. Specifically, attacking this problem within a statistical signal detection

¹ Liew, Y. J., Pala, A., Whitmire, C. J., Stoy, W. A., Forest, C. R., & Stanley, G. B. (2021). Inferring thalamocortical monosynaptic connectivity in vivo. *Journal of Neurophysiology*, 125(6), 2408-2431.

framework utilizing experimentally recorded data in the ventral-posterior medial (VPm) region of the thalamus and the homologous region in layer 4 of primary somatosensory cortex (S1) revealed a trade-off between network activity levels needed for the data-driven inference and synchronization of nearby neurons within the population that results in masking of synaptic relationships. Here, we provide a framework for establishing connectivity in multisite, multielectrode recordings based on statistical inference, setting the stage for large-scale assessment of synaptic connectivity within and across brain structures.

2.1 Introduction

Every aspect of brain function, from sensory and motor processing to memory and cognition, involves complex circuitry and communication across many different brain areas. Despite this fact, what we know about brain function has been derived largely from electrophysiological recordings targeted at single regions, and upon gross anatomical connection patterns across brain regions without specific precise knowledge of synaptic connectivity. Ultimately, understanding the causal interaction of neuronal dynamics that underlie perception and behavior requires ground truth evidence for synaptic connectivity that necessitates intracellular access to both pre- and post-synaptic neurons. Despite exciting advancement of a range of recording technologies such as simultaneous multi-neuron intracellular recordings in-vivo (Jouhanneau and Poulet 2019; Kodandaramaiah et al. 2018) and deep structure targeted patching (Stoy et al. 2017), targeting connections in-vivo using intracellular approaches remains a labour-intensive endeavour, is ultimately limited to a very small number of neurons, and does not scale to the circuit level.

Extracellular recordings offer solutions to some of these issues, and thus offer promise in this direction.

The field of neuroscience is now at a time where large-scale recordings of neuronal populations at cellular resolution are possible across brain structures, due to the development of multi-electrode recording technologies such as ‘Neuronexus’ (Berényi et al. 2014; Buzsáki et al. 2015) (NeuroNexus Inc.), ‘Neuropixels’ (Jun et al. 2017), ‘NeuroSeeker’ (Fiáth et al. 2018; Raducanu et al. 2016)), and 3D silicon probes (Rios et al. 2016). These technologies provide access to surveying network level information flow, driving a growing need for a rigorous experimental and analytic framework to identify functional relationships across brain structures. In previous studies, in-vivo approaches to establishing synaptic connectivity across recorded pairs of neurons have been developed based on analytic methods applied to recorded spiking data (Nowak and J 2000; Perkel et al. 1967), historically conducted in larger animals such as cats, rabbits, and rats (Reid and Alonso 1995; Swadlow and Gusev 2001; Wang et al. 2010) and only more recently in mouse (Lien and Scanziani 2018). Approaches based on spike correlations are the most common for quantifying functional interactions and inferring monosynaptic connections in-vivo. These approaches have been utilized in paired recording studies that involved measuring correlation in the spiking activity between neurons (Barthó et al. 2004; Csicsvari et al. 1998; English et al. 2017; Fujisawa et al. 2008; Reid and Alonso 1995; Swadlow and Gusev 2001; Wang et al. 2010) or between the spiking activity of a pre-synaptic neuron and the subthreshold membrane potential of a putative post-synaptic target (Bruno and Sakmann 2006; Matsumura et al. 1996) (London et al. 2010; Sedigh-Sarvestani et al. 2017; Yu and Ferster 2013). Correlational approaches are statistical in nature and thus have been

anecdotally reported to be strongly dependent upon data length and are very sensitive to a range of possible confounds, but a comprehensive understanding of these relationships and a unified approach are both lacking.

Here, using the thalamocortical circuit in rodents as a model system, we establish methodological strategies for extracellular, topographically aligned in-vivo single-unit recordings in thalamus and cortex for both rat and mouse. This analytic framework for inferring connectivity is based on signal-detection theory, and directly addresses issues of data length dependence and confounds produced by population synchrony. Specifically, we outline a work-flow of topographic mapping and histological validation, followed by a statistical approach for signal-detection based classification of putative connected and non-connected pairs with an assessment of classification confidence that is scalable to the large-scale recording approaches that are emerging in the field. We found that while the amount of spiking was a strong determinant of the accuracy of the inference of connectivity, there was an important tradeoff between the activity in the network and the underlying population synchrony that regulates the likelihood of both discovering a synaptic connection that is present and correctly classifying unconnected pairs as such. Taken together, we provide a data-driven framework for inferring connectivity and the corresponding statistical confidence that generalizes to large-scale recordings across brain structures.

2.2 Methods

2.2.1 *Animals*

Twelve female adult Sprague Dawley rats (no age restriction, 225-330g) and four adult male C57BL/6 mice (8-16 weeks, 25-35g) were used in all the experiments. All procedures were approved by the Georgia Institute of Technology Institutional Animal Care and Use Committee and followed guidelines established by the National Institutes of Health. Note that there were some major differences in animal preparation, surgery and craniotomies as well as electrophysiology for rat and mouse, as described below. However, procedures such as whisker stimulation, post-mortem histology, and analytical methods used for analysis were largely identical.

2.2.2 Animal preparation, surgery and craniotomies.

2.2.2.1 Rat

Animals were first sedated with 5% vaporized isoflurane and maintained at 3% vaporized isoflurane when transitioned to fentanyl-cocktail anesthesia via tail vein injection. Fentanyl cocktail anesthesia (fentanyl [5 µg/kg], midazolam [2 mg/kg], and dexmedetomidine [150 mg/kg])) was administered continuously via a drug pump at an initial rate of 4.5 uL/min (Ahissar et al. 2000a; Whitmire et al. 2016). During the transition, anesthesia level was monitored closely by measurement of heart rate and respiratory rate. Body temperature was maintained at 37 °C by a servo-controlled heating pad. Under the effect of both anesthetic agents, the animal's heart rate tended to decrease gradually over several minutes. The isoflurane level was then titrated down in 0.5% decrements during the transition to the fentanyl cocktail. Upon successful transition, which ranged from 5-15 min depending on the animal, the heart rate was targeted for approximately 240 -270 bpm. After the effects of fentanyl cocktail stabilized (in terms of heart rate) and the animals

showed no toe pinch response, the animals were then fixed in the stereotaxic device by securing the head of the animal in place with ear bars on a floating table in an electromagnetically shielded surgery suite. The position of the ear bars was verified with uniform eye levels and usually with eardrum penetration on both sides of the head. Eye ointment (Puralube Vet Ointment) was applied to prevent the animal's eyes from dehydration. An incision was made along the midline of the skull, and skin was removed for visibility of bregma and lambda (Paxinos and Watson 2007). Connective tissue and muscle that were close to the ridge of the skull were detached and removed to expose the skull surface that was directly above the barrel cortex. To ensure that the skull remained level throughout the recording, the height of the skull surface was measured at bregma and lambda, and the difference was minimized ($< 200 \text{ um}$) by adjusting the angle of the head with the nose cone position.

We made two craniotomies on the animal's left hemisphere above the ventro-posteromedial nucleus (VPm) and the S1 barrel cortex based on stereotaxic coordinates. For the cortical craniotomy, which usually extended over the ridge of the skull, the stereotaxic device was rotated to an angle ($\sim 40^\circ$ relative to vertical) for better visualization and drilling. Both craniotomies were drilled slowly until the skull piece appeared to be floating and mobile. We irrigated the skull surface periodically with Ringer's solution when drilling to remove debris and prevent overheating from drilling. Before removing the skull piece to expose the cortex, a small dental cement reservoir was carefully built around the craniotomies to hold the Ringer's solution for irrigation and to keep the recording site continually moist. The lateral side of the wall was built thicker and higher due to the curvature of the skull toward the ridge. To provide strong adherence to the skull,

cyanoacrylate containing adhesive (Krazy Glue, Elmer's Products Inc.) was carefully applied around the external edges of the reservoir, leaving the bregma and major skull sutures visible at all times. For grounding purposes, another hole with ~0.5 mm diameter was drilled (Henry Schein, Carbide Burr HP 2) on the right hemisphere of the skull and fastened with a skull screw and a metal wire. The skull pieces at both recording sites were then carefully removed with forceps (FST Dumont #5/45). To minimize brain swelling, the dura was left intact on both recording surfaces, and warm Ringer's solution was repeatedly added and absorbed with cotton tips until the blood was cleared. An absorbent gelatin compressed sponge (Gelfoam, Pfizer Inc.) was sometimes used to clear the blood.

2.2.2.2 Mouse

Head-plate implantation and intrinsic imaging procedure were usually performed at least three days to one week before acute experiment. A lightweight custom metal (titanium or stainless steel) head-plate was implanted on the skull of the mouse for head fixation and improved stability during recording, in accordance with a previously described protocol (Borden et al. 2017). During this survival surgical preparation, the animal was sedated with 5% vaporized isoflurane and anesthesia was maintained with 2-3% isoflurane for the head-plate procedure. We administered opioid and non-steroidal anti-inflammatory analgesic (SR-Buprenorphine 0.8 - 1 mg/kg, SC, pre-operatively, and Ketoprofen 5-10 mg/kg, IP, post-operatively) and covered the animal's eyes with ophthalmic eye ointment (Puralube Vet Ointment). Body temperature was monitored and maintained at 37 °C. After sterilizing the skin above the skull and applying topical anesthetic (lidocaine 2%, 0.05 ml, max 7mg/kg, SC), we removed the skin and scraped off periosteum and any conjunctive

tissue off the skull. We gently separated tissue and muscles close to the lateral edge of the skull using a scalpel blade (Glass Van & Technocut, size no. 15), leaving sufficient room for head-plate attachment and away from targeted recording areas. To ensure that the skull surface remained level during head fixation, we adjusted animal's head position to minimize the relative height difference ($< 150 \mu\text{m}$) between the skull surface at the bregma and lambda landmarks (Franklin and Paxinos 2008). We found this step to be critical especially for VPM targeting. We secured the metal headplate over the intact skull with C&B-Metabond (Parkell Prod Inc) and skin adhesive (Loctite 401, Henkel). The Metabond dental acrylic was chilled using ice, slowly applied to the skull surface, and allowed to cure for 5-10 minutes before we covered the rest of the attachment site and edges of the skin incision with skin adhesive (Loctite 401) to ensure that the skin edges were securely adhered to the skull. The final head-plate and dental acrylic structure created a recording well for holding Ringer solution (in mM: 135 NaCl, 5 KCl, 5 HEPES, 1 $\text{MgCl}_2 \cdot 6\text{H}_2\text{O}$, 1.8 $\text{CaCl}_2 \cdot 2\text{H}_2\text{O}$ pH 7.3) for future imaging and electrophysiological recording sessions. For grounding purposes, another hole with $\sim 0.5 \text{ mm}$ diameter was drilled (Henry Schein, Carbide Burr HP 2) on the right hemisphere of the skull and fastened with a skull screw (Miniature Self-Tapping Screws, J. I. Morrisco). A metal wire was connected to the skull screw on the day of recording to serve as animal ground. We applied a thin layer of transparent glue (Loctite 401, Henkel) over the left hemisphere to protect the skull and covered the exposed skull with a silicone elastomer (Kwik-Cast, World Precision Instruments) if there were no other additional procedures after head-plate implantation.

2.2.2.3 Intrinsic Optical Imaging in the Mouse S1 Barrel Cortex

We performed intrinsic signal optical imaging of whisker-evoked responses in mouse primary somatosensory cortex under 1-1.2% isoflurane anesthesia to functionally identify individual barrel columns (Lefort et al. 2009; Pala and Petersen 2015). All whiskers except the whiskers of interest (A2, B1, C2, D1, D3 and E2) were trimmed. We thinned the skull using a dental drill (0.1 mm diameter bit, Komet, USA) until blood vessels became visible. We applied warm Ringer's solution on top of the skull and covered it with a glass coverslip (thickness 0.13-0.17mm, Fisherbrand). We captured a reference image of the blood vasculature under green illumination (530nm) (M530F1 LED, Thorlabs). We delivered repetitive whisker stimuli (10 Hz, sawtooth pulses, 1000 deg/s) to individual whiskers using a galvanometer system (Cambridge Technologies) while performing imaging on barrel cortex under red illumination (625 nm) (M625F1 LED, Thorlabs) – see Whisker Stimulation section below. Images were acquired using a CCD Camera (MiCam02HR, SciMedia) at 10 Hz, with a field of view of approximately 4 x 2.5 mm, corresponding to 384 x 256 pixels (resolution: 100pixel/mm). Each trial lasted 10s, with 4s of baseline followed by 4s of whisker stimulation and 2s without stimulation. The inter-trial interval was 30s. Whisker-evoked responses were averaged over 10-20 trials. Intrinsic signals were measured as the relative change in reflectance by taking the overall mean reflectance during whisker stimulation (R_{stim}) and subtracted the mean baseline reflectance ($R_{stim} - R_{baseline}$). Acquisition and processing of the images were implemented using “BV_Ana” software (MiCam02HR, SciMedia, Ltd) and Matlab (MathWorks, Natick, 2015). We recorded intrinsic signals from at least three barrels and estimated location of the unmapped barrels by overlaying a template barrel map reconstructed from histology. At the end of the imaging session, we applied transparent glue (Loctite 401) directly on the

S1 site to protect the thinned skull from contamination and infection and sealed the exposed skull with a silicone elastomer (Kwik-Cast, World Precision Instruments).

On the day of recording, the head of the mouse was held in place with a head-post clamp and animal should remain in the flat skull position. We covered the eyes with ophthalmic eye ointment (Puralube Vet Ointment) to prevent dehydration. The animal was then anesthetized using 2-3% isoflurane. Before performing the craniotomies, we thinned the skull above VPm and S1 layer-by-layer with a dental drill (0.1 mm diameter bit, Komet, USA) and irrigated the skull surface with Ringer's solution frequently to remove debris and prevent overheating. When the skull was thin enough to easily puncture, we made two small craniotomies above VPm (approximately 1 mm diameter; centered at 1.8 mm caudal and 1.8 mm lateral to bregma) and S1 (approximately 0.5 mm diameter, using the intrinsic imaging signal and the blood vasculature as a landmark) by penetrating the thinned skull using an insulin syringe needle tip (at about 40-50 degree angle) to make small holes outlining the edges of the craniotomies until the circular skull piece was loosely attached. The less perforated region of the circular skull piece was used as a pivot, and we levered the skull pieces off from the more perforated edge using fine-tip forceps (FST Dumont #5SF) to expose the brain surface.

2.2.3 Electrophysiology

2.2.3.1 Neuronal recordings

Tungsten microelectrodes (FHC, impedance: 2-5 M Ω , 75 μ m in diameter) were used in thalamus and cortex to isolate single units that were responding to a single primary whisker on the contralateral side of the face. Multielectrode silicon probes with 32

recording sites (A1x32-Poly3-5mm-25s-177 or A1x32-Poly2-10mm-50s-177, NeuroNexus) were also independently lowered into the thalamus and cortex. To improve signal quality, we electroplated the silicon probes with the polymer PEDOT:PSS ([Baião 2014](#)) with a nanoZ device (Multi Channel Systems, Germany). The impedances of the contact sites were measured prior to each recording and ranged from 0.3-0.8 MOhms. After each use, the contact sites were soaked in 20% Contrad (labware detergent) overnight for cleaning and the impedances usually returned to the initial values (0.3-0.8 MOhms). The impedances for the silicon probes were always measured prior to a recording session and contact sites that were defective usually showed large fluctuations in raw voltage traces and signals detected at these sites were excluded for analysis prior to spike-sorting. Note that tungsten microelectrodes were used in rat studies and probe recordings were used in mouse studies. Data were collected using a 64-channel electrophysiological data-acquisition system (TDT Model, etc. RZ2 Bioprocessor). Neuronal signals were amplified, and bandpass filtered (500Hz-5kHz) and digitized at ~25kHz per channel. Stimulus waveform and other continuous data were digitized at 10kHz per channel. Simultaneously, the local field potential (LFP) signals were obtained by using a 0.5-200Hz bandpass filter. The LFPs were used to identify primary whisker response (see Whisker Stimulation).

2.2.3.2 Rat - VPm recordings

We targeted the VPm region of the thalamus by advancing a single tungsten microelectrode (FHC, 2 MOhm impedance) perpendicular to the pial surface into the thalamic craniotomy centered at 3.0 mm caudal and 3.0 mm lateral to bregma. We quickly advanced (~50um/s) to the depth of 4000 μ m and slowed down to the speed of ~3 μ m/s

while searching for responsive cells by manually deflecting the whisker on the contralateral side of the vibrissal pad. Whisker responsive cells were typically located at a depth of 4800-5300 μm , measured using a precision micromanipulator (Luigs & Neumann, Germany). *SI recordings*. At a position 5.8 mm lateral and 2.5 mm caudal to bregma, we inserted a single tungsten microelectrode at an angle of 40-45° (relative to the vertical axis of electrode holder). We positioned the tip of the electrode gently touching the dura and advanced slowly to create an opening in the membrane. The microelectrode was then slowly advanced into cortical tissue at a speed of $\sim 3 \mu\text{m/s}$ (measured at 1 μm resolution). All cortical units were recorded at stereotaxic depths of 700-1000 μm , corresponding to layer IV of rat barrel cortex based on literature (Bruno and Sakmann 2006; Constantinople and Bruno 2013).

2.2.3.3 Mouse - VPm recordings

For first penetration, electrode was typically lowered at 1.8 mm caudal and 1.8 mm lateral to bregma. If we could not functionally locate VPm using this method, we used the relative distance from the location of barrel cortex (usually measured 1.0-1.2mm from the B1 or Beta barrel column to find whisker responsive thalamic regions). For probe recordings, we searched for whisker responsive cells by manual whisker deflection using the deepest channel as reference. We typically found whisker responsive cells were at a depth between 2800 μm -3200 μm . *SI recordings*. Based on intrinsic imaging signal, a small craniotomy (diameter $\sim 0.5 \text{ mm}$) was created at the desired location on the barrel cortex that was distant from blood vessels. We positioned the electrode at a 35 ° angle from the vertical

axis (parallel to the barrel column) and recorded from cortical neurons at a stereotaxic depth of 300-500um from the cortical surface.

2.2.4 *Whisker Stimulation*

To identify the single whisker of interest, we first manually deflected all whiskers on the vibrissal pad while monitoring the extracellular signal. Once units were isolated by moving the electrode as close as possible to the responsive cells that primarily responded to single whisker, we delivered controlled, single whisker stimulation in the rostral-caudal plane using a computer-controlled actuator, galvo-motor (galvanometer optical scanner model 6210H, Cambridge Technology). Whiskers were trimmed ~12 mm from the face. Primary whisker (PW) was defined as whisker deflection that evoked the maximal neuronal response with shortest latency (see Transient Stimulus). The primary whisker was fed into the insertion hole at the end of an extension tube (inner diameter: ~200-300 μm , length: 15mm) that was connected to the rotor of the galvanometer stimulator. The stimulus probe was positioned at 10 mm from the vibrissal pad. The range of motion of the galvanometer was $\pm 20^\circ$, with a bandwidth of 200Hz. The galvanometer system was controlled using a custom developed hardware/software system (Matlab Real-Time Simulink System, MathWorks). Whisker evoked responses were measured using raster plots and peri-stimulus time histograms (PSTH, 1-ms bin resolution) across trials.

2.2.4.1 Transient stimulus

For mapping whisker receptive field at the recording sites, we presented high velocity (600 or 1000 $^\circ/\text{s}$) rostral-caudal whisker deflection to evoke reliable whisker responses. Trains of solo pulses, followed by a separate, pulsatile adapting stimulus at 8-

10 Hz (Borden et al. 2017; Whitmire et al. 2016) were delivered for 60-100 times. To measure whisker response to different stimulus strength, pulses with angular deflection velocities of 50, 125, 300, 600, 900, 1200 deg/s were presented randomly. Rostral-caudal pulse deflections were either a Gaussian-shaped deflection waveform or a simple exponential sawtooth (rise and fall time = 8 ms). We quantified whisker evoked activity 30 ms after stimulus onset and then further characterized onset latencies of first spike within the response window in response to non-adapting solo pulses and adapting pulsatile stimuli over 60-100 trials. Mean first spike latencies, defined as the average time delay between stimulus onset and the first spike in the response window after stimulus presentation. This metric was used for all thalamic and cortical units. For 32-channel probe recording in thalamus, we quantified the LFP response in a 30 ms post-stimulus window for each channel to identify principal whiskers (PW). Well-isolated single units that showed whisker responsiveness was verified by calculating LFP peak amplitude and peak latency to different whisker stimulation.

A neuronal pair was verified to be topographical aligned when they (1) shared maximum response (SUs max FR and LFP amplitude) to the same primary whisker under punctate stimulation and (2) latency difference of whisker response within 1-5 ms delay (LFP peak latency and SU mean FSL, or SU mean peak latency).

2.2.4.2 Weak sinusoidal stimulus

For monosynaptic connection quantification, we probed the thalamocortical circuit using a weak, desynchronizing sinusoidal whisker stimulus to elevate baseline firing rates in recorded units. We delivered 4°, 2-4Hz weak sinusoidal deflections (Bruno and

Sakmann 2006; Bruno and Simons 2002; Wang et al. 2010) for approximately 200-500 trials to obtain at least 2000 spikes for the cross-correlation analysis. Occasionally, we eliminated the first 0.5-1 s of the trials due to high firing rate at the onset of stimulus presentation.

2.2.5 Post-mortem Histology

In order to verify recording sites and the angle of penetration that was optimal for locating VPM and S1, we perfused a small subset of animals after the paired recording experiment. To label each electrode recording track, we slowly retracted the electrode along its axis of entry at the conclusion of recording and applied a few drops of DiI (2.5mg/mL, in ethanol). We then reinserted the electrode into the same penetration site and back along the same axis and left the electrode in the brain for at least 15 minutes. Following the end of the experiment, we euthanized the animal with an overdose of sodium pentobarbital (euthasol, 0.5 mL at 390mg/mL for rat, 0.1 mL at 390 mg/mL), performed a transcardial perfusion, extracted the brain, and fixed the brain in 4% paraformaldehyde (PFA, Electron Microscopy Sciences) overnight. We sliced the brain in 100 um coronal sections and performed cytochrome oxidase staining to reveal VPM (barreloid) and S1 (barrel). As an additional verification of recording site, we identified the overlap between the DiI stained recording track and the CO-stained regions.

2.2.6 Analytical Methods

2.2.6.1 Extracellular spike sorting

In assessing potential synaptic connectivity using cross-correlation analysis, the clear isolation of single unit activity from extracellularly recorded voltage signals is particular critical. In all of our paired recording experiments, we performed extracellular single-unit recordings using either Tungsten microelectrodes or 32-channel NeuroNexus probes. Although similar in approach, the sorting of recorded data into clusters were implemented using different software. For the single micro-electrodes, we performed spike sorting offline using the Plexon Offline Sorter (Plexon Inc, Dallas TX, USA), while for the 32-channel probe recordings we utilized KiloSort2 software package (<https://github.com/MouseLand/Kilosort2>) (Harris et al. 2000). For high density probe recordings, there was an additional manual curation step using *phy* (<https://github.com/cortex-lab/phy>) where we refined the output of automatic algorithm and determined if merging or splitting of specific clusters were necessary based on refractory violation, waveform shape as well as cross-correlogram between clusters. For both Tungsten microelectrode and high-density probe recordings, we classified the clusters as single- or multi-units based on the signal-to-noise ratio and inter-spike interval (ISI) distribution. We only included well-isolated clusters for further analysis. The selection of well-isolated clusters, or single units, was based on two criteria: (1) high signal-to-noise ratio (SNR) of the spike waveform: Peak-to-peak amplitude (V_{pp}) of spike waveforms greater than three standard deviations (SD) of the waveform. (2) Had a clear refractory period (Buzsáki 2004; Fiáth et al. 2019). We defined a single-unit as well-isolated if it had SNR greater than 3, ISI violation less than 1% for cortical unit and 2% for thalamic unit and spike waveform with a peak-to-peak amplitude (V_{pp}) greater than $60 \mu V$. Given that the spikes of the same neuron were usually detected on multiple sites of a 32-channel probe, the peak-to-peak amplitude and standard

deviation of the waveform were computed using channel that had the largest amplitude of spike waveform.

2.2.6.2 VPm unit verification

It is important to distinguish different thalamic nuclei from one another, and particularly so in the mouse, where the regions are very small and very close together. After recording, we used a combination of measures to classify thalamic units as VPm: (1) Average first-spike latency to punctate (non-adapting) stimuli, quantifying the average time between stimulus onset and the first spike fired during the neural response window (30 ms after stimulus onset) (Storchi et al. 2012). (2) Shift in average first-spike latency response to adapting stimuli, defined as the time difference between average response to the first adapting stimulus and last adapting stimulus (Masri et al. 2008). (3) Response reliability, defined as the percentage of trials where a response was detected within 20ms to repetitive stimulation (8-10Hz) (Mainen and Sejnowski 1995). We excluded thalamic units with average first-spike latency of more than 12 ms (see Figure_A-2A), latency shift of more than 20ms, or response reliability of less than 20%.

2.2.6.3 Cortical unit classification

It was known that S1 layer IV is the major thalamocortical recipient from VPm projections and there exist some heterogeneity in terms of cortical cell types in Layer IV (Bruno and Simons 2002). Here, we classified cortical units into fast-spiking unit (FSU) and regular-spiking unit (RSU) by using waveform parameter. We quantified the time interval between trough to peak (t_{2p}) of the spike waveform (Barthó et al. 2004).

2.2.6.4 Cross-correlation analysis

All analysis was performed in a trial-by-trial basis. Given a spike in a ‘reference’ neuron, we computed the relative times of the spikes from a ‘target’ neuron that occurred within a 25-millisecond window before and after each reference spike. Cross-correlograms were constructed using a 0.5 millisecond bin. Traditionally, monosynaptic interactions were known to produce short latency peaks in the cross-correlograms. The latency of the monosynaptic peak within cross-correlograms was typically reported to center around 2.5 ms, estimated from thalamocortical EPSPs and spiking activity (Alonso and Martinez 1998; Alonso et al. 2001; Bruno and Sakmann 2006; Bruno and Simons 2002; Reid and Alonso 1995; Sedigh-Sarvestani et al. 2017; Swadlow et al. 1978; Swadlow 1989; 2003; Swadlow and Gusev 2001). To ensure our analysis captures correlation from monosynaptic delays only, we allowed for 1.5 ms jitter on each side, setting the lower bound to be 1 ms and the upper bound to be 4 ms. This eliminated peaks that could arise in the 0-1 ms bin due to a shared common input, as well as disynaptic EPSPs that could have latencies longer than approximately 5 ms (Gil and Amitai 1996). Here, for the monosynaptic connectivity inference, we used thalamic spiking as the reference and cortical spiking as the target and examined correlated firing within a lag window of 1-4 ms. The results here were relatively invariant to the specific choice over a range of lag windows, but we found the 1-4ms window to be the most conservative (i.e. smaller window than 1-5 ms but resulted in same number of pairs classified as “connected”, see below Figure_A-3). For the spontaneous condition, we segmented the spike train data into 5s-trials (matching duration of stimulus-based trials) and performed cross-correlation analysis in a trial-by-trial manner. To measure the level of presynaptic synchronization in thalamus, we performed a cross-

correlation analysis and computed synchrony strength using a central area under the cross-correlogram for all thalamic pairs that responded to the same principal whisker. The principal whisker was identified using the functional responses as measured by the local field potential (LFP) and in the single unit (SU) data. Thalamic synchrony was computed for each thalamic pair using the total number of spikes within a 15 ms (± 7.5 ms) window of the cross-correlogram (N_{cc}), normalized by the mean number of spikes from each neuron (N_{ref} , N_{target}) (Alonso and Martinez 1998; Bruno and Sakmann 2006; Temereanca et al. 2008; Wang et al. 2010; Whitmire et al. 2016):

$$strength = \frac{N_{cc}}{\sqrt{\frac{N_{ref}^2 + N_{target}^2}{2}}}$$

2.2.6.5 Probabilistic measure of connectivity inference

For each pair of thalamocortical neurons, we repeated the cross-correlational analysis with bootstrapping method. This was done by performing resampling on the dataset with replacement, with approximately 500-1000 iterations for each condition. By counting the number of iterations that fulfill the criteria for classifying the monosynaptic connection, this resulted in a p-value that can be attached to the binary classification of monosynaptic connection (see Results: Inferring connectivity in the context of a signal detection framework). We referred to this p-value as the probability of inferring monosynaptic connection, $P(\text{Inferring 'connected'})$.

To evaluate data-length effect on the connectivity metric, simulation for various data-lengths was implemented by using subsamples (in unit of trials) of VPm and S1 spikes for cross-correlation analysis. For each data-length condition, we computed the resampled peak height, h^* . A bootstrapped estimator of bias was computed as the difference between the mean of the resampled peak height and the original metric, assuming a normal distribution:

$$bias = E(h^* - h)$$

Where $E(.)$ denotes statistical expectation. The variance was estimated as the square of the resampled peak height:

$$variance = var(h^*)$$

A significance level for the inference for a ‘putatively connected’ pair was computed and denoted as the probability of a hit when the peak height metric for the resampled data exceeded the criterion for the inference of a functional connection. The probability of a miss is complementary:

$$P(hit) = \frac{\# \{h^* \geq criterion\}}{\# of iterations}, \quad criterion = 3.5$$

$$P(miss) = 1 - P(hit)$$

On the other hand, the significance level for a ‘not connected’ pair was computed and denoted as the probability of a correct reject when the peak height metric for the resampled data is less than the criterion.

$$P(\text{correct reject}) = \frac{\#\{h^* < \text{criterion}\}}{\# \text{ of iterations}}, \text{ criterion} = 3.5$$

$$P(\text{false alarm}) = 1 - P(\text{correct reject})$$

To evaluate thalamic synchrony effect on connectivity metric, simulation for various thalamic synchrony level was implemented by manipulating both firing rate and spike timing of VPm and S1. Given that both firing rate and thalamic synchrony were affected with increasing stimulus strength, our simulation was conducted using data that was collected under spontaneous condition. For a connected pair, we set the ratio between VPm and S1 firing to be constant at each synchrony level for simplification. However, we systematically increased spiking activity (in number of spikes per trial) in VPm and S1 with a specific amount of jitter (zero-mean Gaussian noise of a specific standard deviation, sigma) as a function of thalamic synchrony. For a not-connected pair, the increase in thalamic synchrony and VPm and S1 firing were simulated by systematically adding spikes from another pair of neurons that is putatively connected. The assumption here was that a not-connected pair would become more identical to its neighboring neuron (that has a functional connection to the downstream S1 neuron) with increasing synchrony. This was repeated from 100-500 iterations for each synchrony level and the probability of satisfying Criterion 1 and 2 was computed.

2.3 Results

Here, we present a comprehensive experimental and analytic framework for assessing synaptic connectivity using extra-cellular spiking activity from simultaneously

recorded single units across brain structures. First, we provide a rigorous experimental protocol for performing simultaneous single-unit electrophysiological recording in topographically aligned regions in the thalamocortical circuit of the somatosensory pathway using a combination of stereotaxic targeting based on anatomical landmarks, sensory-evoked response properties, and post-hoc histological validation. We highlight some similarities and differences of the technical aspects of paired recordings performed in rats versus mice, two commonly used rodent species in mammalian electrophysiology. Next, we generate inferences regarding the synaptic connectivity of two single units based on spike correlation analysis across the presynaptic VPm and postsynaptic S1 spiking, leading to classification as either “connected” or “not connected”, using an approach to be explained in detail below. Figure 2-1A highlights the basic experimental setup and analysis utilized in this study, with electrophysiological recordings targeted to primary somatosensory “barrel” cortex (S1, red) and to ventro-posteromedial thalamus (VPm, blue), during controlled deflections of a single whisker on the contralateral side of the face with a computer-controlled actuator (see Methods). In the context of a signal detection framework, we then quantify the effects of experimental data-length and local synchrony of presynaptic neurons on monosynaptic connection inference, and importantly, expand this framework to attach statistical levels of confidence to the synaptic connectivity inferences.

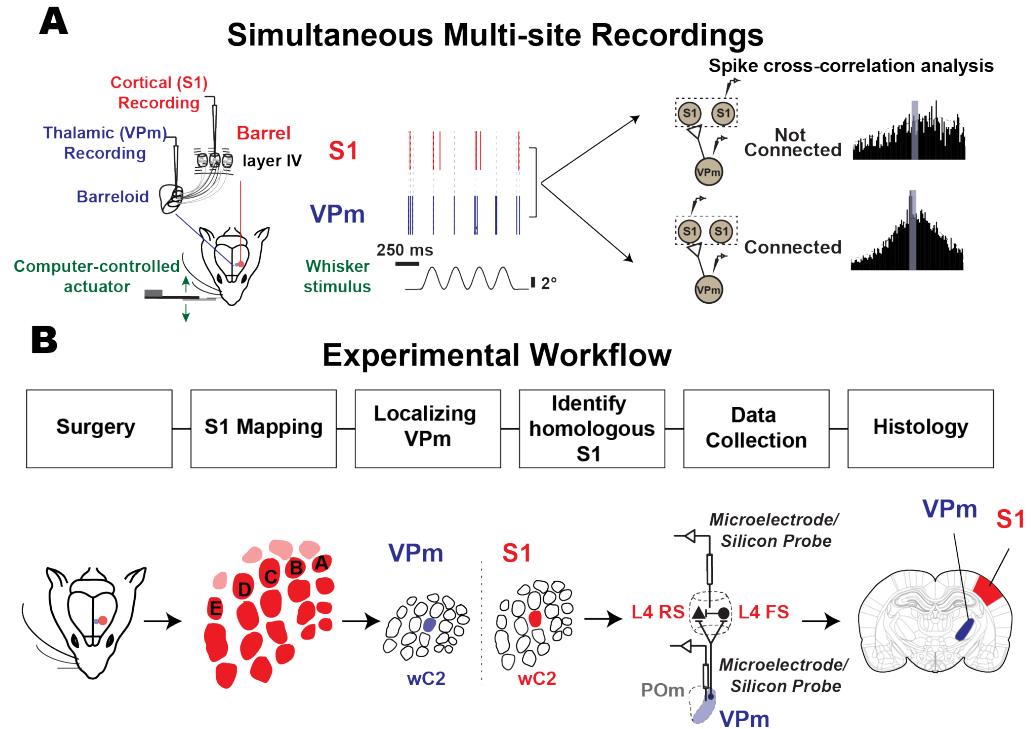


Figure 2-1. Experimental approach used to estimate monosynaptic connectivity between somatotopically-organized areas of the rodent somatosensory pathway.

A. Simultaneous single-unit extracellular recordings were performed in the ventral posteromedial (VPm) nucleus of the thalamus and in layer IV of primary somatosensory cortex (S1) in anesthetized rodents. Recordings were targeted to topographically aligned barreloids in VPm and barrel column in S1. Weak stimulation was applied to the whisker corresponding to the recorded barreloid/barrel column to elicit non-synchronous spiking. Putative monosynaptic connection between pairs of neurons were inferred using cross-correlation analysis. B. Experimental procedures used to establish paired recordings involve (1) Animal preparation includes surgeries. (2) S1 mapping, (3) identification of the whisker corresponding to the recorded barreloid, (4) targeting corresponding S1 barrel column and layer IV, (5) data collection for assessing monosynaptic connectivity by generating spikes via whisker stimulation, repeating step (3), (4) and (5) for recording additional pairs and (6) histology. FS, fast-spiking unit; L4, layer 4; POm, posteromedial nucleus; RS, regular-spiking unit; wC2, C2 whisker.

2.3.1 Experimental workflow to establish paired recordings

Paired recordings in topographically aligned feedforward sensory regions in-vivo have been previously shown to be experimentally tractable (Bruno and Sakmann 2006; Bruno and Simons 2002; Reid and Alonso 1995; Swadlow and Gusev 2001; Wang et al. 2010) yet it remains a challenging process, and to our knowledge, detailed reports on experimental approaches have not been published in full. Here, we documented the steps in details. Figure 2-1B summarizes the general workflow for establishing and analyzing paired recording: 1) mapping primary somatosensory cortex (S1), 2) localizing the ventral posteromedial (VPm) nucleus of the thalamus, 3) achieving and verifying topographical alignment of recording electrodes across VPm and S1, 4) connectivity assessment through statistical analysis of the measured spiking activity from pairs of single-units across recording sites, and 5) histological verification of recording site locations.

Although the final electrode placement for paired recording involved thalamic electrode placement followed by placement of the cortical electrode, we found that an initial somatotopic mapping of cortex was critical for efficiently achieving topographical alignment. As part of the approach, we thus first performed coarse cortical mapping prior to thalamic localization. In rat, we employed primarily electrophysiological mapping approaches for this coarse mapping of S1. We targeted S1 using approximate stereotaxic coordinates and inserted a single electrode to obtain the functional location of several “barrels” using bregma as a reference point. Once we located the S1 region, we identified the stereotaxic location of three barrel columns containing neurons that were responsive to the movement of single primary whiskers (See Figure_A-1 -

<https://doi.org/10.6084/m9.figshare.14393528.v1>). We used this relative distance between columns/barrels to estimate the overall topography of S1 by overlaying a barrel map template scaled to fit the three data points. In mouse, taking advantage of the optical properties of the mouse skull (i.e., that it is relatively translucent), we employed intrinsic optical signal imaging (IOS) for the coarse cortical mapping. Intrinsic optical signals were acquired in response to separate, punctate deflections of three different single vibrissae. The corresponding cortical regions of activation were co-registered with the anatomy of the blood vessels and further used as a landmark for electrode placement. This triangulation methodology was adapted from previously published method from our laboratory (Gollnick et al. 2016; Millard and Stanley 2013). An example of this is shown in Figure 2-2A (see also Figure_A-1). The three images on the top row were acquired in response to punctate deflections of the Beta whisker (wBeta), the C2 whisker (wC2), and the B2 whisker (wB2), respectively. Each image represents the mean 0- to 6-s post-stimulus response (baseline subtracted and scaled) to a 4-s 10-Hz 1000 deg/s pulsatile stimulus, with the region of cortical activation appearing as a dark spot near the center of the image, at different locations for each whisker. We then fitted a barrel map template, recovered from histological brain sections from previous experiments onto the overall optical image of the brain surface through the thinned skull (template shown in bottom left of Figure 2-2A). The three centroids of the intrinsic imaging signals were used as reference points (Figure 2-2A bottom middle) for transformation of the barrel map template involving scaling, rotation, translation and shearing. This transformed map along with the blood vessel image (Figure 2-2A, bottom right) was then used as a navigation guide for electrode placement for targeting a desired barrel column.

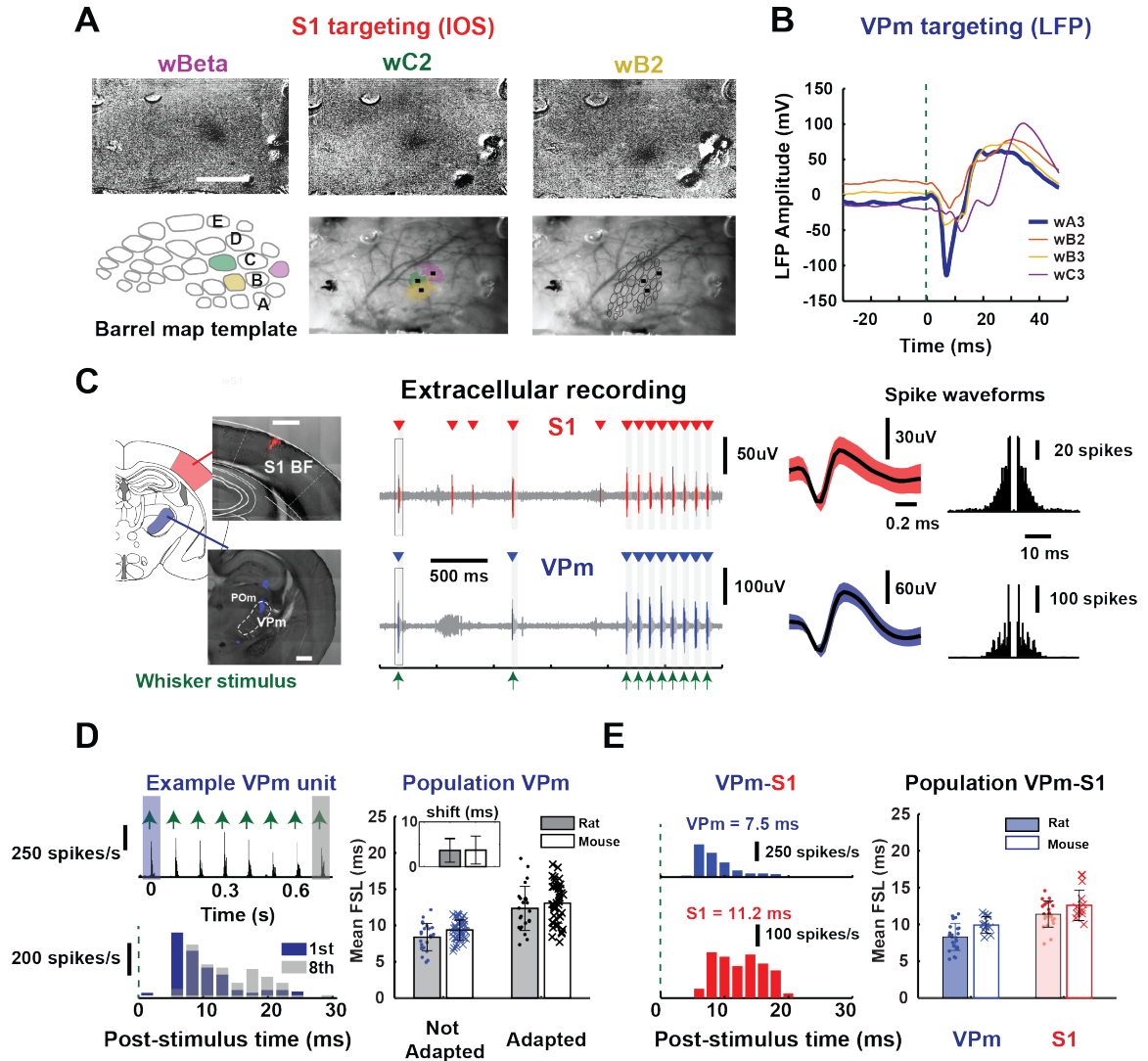


Figure 2-2. Targeting topographical alignment in vivo.

A. S1 targeting: Location of S1 barrels was determined using intrinsic imaging (IOS) in mice. The three images on the top are images acquired in response to separate single punctate deflections of the Beta whisker, the C2 whisker, and the B2 whisker, respectively. A barrel template was compared to the optical image of the brain surface through the thinned skull and fitted based on the location of the centroid of barrels to provide guidance for electrode placement. **B.** (Left) VPM targeting: example mean LFP amplitude of evoked response (shown by downward deflection after stimulus onset) for four stimulated whiskers in mice. Note the largest and fastest response to the A3 vibrissa, and the comparatively weak responses to the adjacent B2, B3, and C3 vibrissae, lending support for VPM localization. **C.** Left: Histological slice showed electrode tracks marked with fluorescent dyes (see Method: Post-mortem histology) on coronal brain sections targeting VPM (bottom) and S1 layer IV (top) in a mouse. Middle: Example raw voltage traces from extracellular recordings performed simultaneously in VPM and S1 layer IV during sensory

stimulation in a rat. Mean waveforms of isolated single units from each recording site were shown (shaded region indicates one standard deviation of spike amplitude), along with spike auto-correlograms of each unit in a rat (Right). **D.** Left: Example adapting response of a single thalamic unit from a rat, showing mean first-spike latency in response to first and last pulse of a 8Hz pulsatile, ongoing stimulus (1st pulse: 5.18 ms, last pulse: 10.7 ms). Right: Population adapting response for thalamic units recorded in rats and mice (1st pulse (rats): 8.39 ± 1.87 ms, last pulse (rats): 12.3 ± 3.04 ms, $n = 24$ neurons, $N = 12$ rats, 1st pulse (mice): 9.37 ± 1.39 ms, last pulse (mice): 13.1 ± 2.78 ms, $n = 39$ neurons, $N = 4$ mice). Inset: All thalamic units that we recorded showed latency shift less than 20 ms (latency shift (rats) = 3.65 ± 2.62 ms, $n = 24$ neurons, $N = 12$ rats, latency shift (mice) = 3.71 ± 3.11 ms, $n = 39$ neurons, $N = 4$ mice), suggested that they were thalamic VPm units. **E.** Left: Example peri-stimulus time histogram (PSTH, 2 ms binsize) for a thalamic and cortical unit in the 30-ms window following punctate (600°/s) whisker stimulus (indicated by green dotted line at $t=0$). We computed mean first spike latency (FSL), defined as average latency of first spike in 30 ms response windows after stimulus presentation for each unit (VPm: 7.5 ms, S1: 11.2 ms). Right: Population mean first spike latency for all simultaneously recorded thalamic and cortical units in rats and mice (VPm (rats) : $8.30 \text{ ms} \pm 1.84$, S1 (rats): 11.40 ± 1.77 ms, $n = 22$ neurons, $N = 12$ rats; VPm (mice): 9.80 ± 1.31 ms, $n = 9$ neuron, S1 (mice): 12.6 ± 2.06 ms, $n = 11$ neuron, $N = 1$ mouse). BF, barrel field.

Once the cortex was coarsely mapped using the above approaches, we inserted an electrode to localize VPm (see Method: Electrophysiology). Specifically, we identified specific thalamic barreloids by manually deflecting each of the facial vibrissae individually in order to find an isolated unit that was maximally responsive to a single whisker only. Note that the procedure was nearly identical for rat and mouse, except that for the mouse, a silicon multi-electrode probe was utilized, and localization was performed using one of the probe sites, usually the deepest probe contact. Given that the probe was spanning several hundred microns on the thalamic recording site, we typically recorded from one to three barreloids simultaneously with two or more recording sites within a single barreloid. Final placement of the electrode was fixed when well-isolated units were detected on probe contacts. For verification of barreloid targeting within VPm, we compared local field potential (LFP) responses to individual stimulation of multiple nearby vibrissae. Figure 2-2B shows an example of LFPs recorded in the A3 barreloid of thalamus on one of the

probe contacts. Note that the evoked LFP response exhibits an initial negative peak for the whisker A3 deflection (wA3, blue) that is substantially larger than responses to the deflection of other whiskers.

A practical challenge lies in the positioning of the recording electrodes to reach the multiple target areas. In a small subset of experiments, we optimized the electrode insertion angle by coating the electrodes with fluorescent dye (DiI) to mark the electrode track for post-experiment histological analysis. A range of insertion angles was tested for both S1 and VPm in mouse and rat. We found that the optimal electrode angle to target VPm thalamus in both rats and mice was 0 degrees from vertical (perpendicular to the brain surface) (Figure 2-2C left and Figure_A-1). For S1 targeting, we found that the optimal angle for rats was approximately 40-45 degrees from vertical and was approximately 30-35 degrees from vertical for mice for electrode penetration parallel to the cortical column/barrel, important for accurate targeting of specific cortical depths. The target recording site depths were determined based on published anatomical locations of the target structures (see Methods). Figure 2-2C shows typical electrode tracks targeting S1 and VPm in a mouse (left), along with the corresponding raw extracellular recordings from one VPm and one S1 electrode recording site (middle). Both the VPm and S1 extracellular recordings show sensory driven responses to deflections of the same whisker, the pattern of which is shown in the extracellular recordings of Figure 2-2C. The times of whisker stimulation are denoted with the green arrows, representing a pattern of two isolated whisker deflections, followed by an 8 Hz train of whisker deflections. The raw electrophysiological recordings were subsequently sorted into single-unit data based on conventional spike sorting approaches and only well-isolated units were retained for

analysis (see Methods). For each recording, the identified putative single unit spiking (red, blue) is superimposed on the raw recording (light gray), and the corresponding spike times are denoted above each trace (red and blue triangles). For each case, the spike waveform and spike auto-correlogram are shown to the right in Figure 2-2C.. A summary of the waveform size and isolation quality for all recorded VPm and S1 units is shown in Figure_A-1C.

2.3.2 *Sensory response in topographically aligned VPm – S1 layer 4 regions*

Achieving topographically aligned recordings across corresponding thalamic barreloids and cortical barrel columns necessitates the accurate targeting of the thalamic recording electrode/probe to the VPm nucleus of the thalamus. In particular, it is key to be able to distinguish whisker-responsive units located in VPm from those located in the adjacent posteromedial nucleus (POm) of the thalamus. In previous studies, POm units have been shown to exhibit lower evoked firing rate (Ahissar et al. 2000a; Diamond et al. 1992; Landisman and Connors 2007; Sosnik et al. 2001) and much broader receptive fields than VPm units, responding to approximately six vibrissae on average, ranging from three to twelve whiskers (Castejon et al. 2016; Diamond et al. 1992). Hence, to ensure recordings from primarily VPm neurons, we selected thalamic units that showed restricted whisker sensitivity, usually only to one principal whisker (as previously shown in Figure 2-2B, VPm targeting (LFP)). The thalamic single units kept for subsequent connectivity analysis exhibited strong, reliable response (response reliability: 52.6 ± 24.62 %, not shown) to a punctate whisker stimulus with short latency (1st pulse (rats): 8.39 ± 1.87 ms (mean \pm SEM), last pulse (rats): 12.3 ± 3.04 ms (mean \pm SEM), n = 24 neurons, N = 12 rats, 1st

pulse (mice): 9.37 ± 1.39 ms (mean \pm SEM), last pulse (mice): 13.1 ± 2.78 ms (mean \pm SEM), $n = 39$ neurons, $N = 4$ mice, Figure 2-2D and Figure 2-2E, Figure_A-2). As an additional criterion, we measured the adapting properties of the thalamic units in response to repetitive, periodic whisker stimuli (Ahissar et al. 2000a; Masri et al. 2008) (Sitnikova and Raevskii 2010). Previous studies have shown that neurons in POm exhibit dramatic adaptation to persistent sensory stimulation, where most Pom neurons failed to exhibit a response to stimuli ≥ 11 Hz (Masri et al. 2008), and a significant shift in response latency with the adaptation, as compared to VPm neurons (Ahissar et al. 2000a; Sosnik et al. 2001). Here, we showed a representative thalamic unit spiking response to an 8 Hz adapting whisker stimulus on the left in Figure 2-2D with a PSTH in response to the full stimulus train (top) and a superposition of the stimulus evoked response to the 1st (blue) and 8th (gray) deflection in the train (bottom). This particular example shows strong stimulus-locked responses and moderate adaptation (i.e., reduction in response amplitude), with a relatively small increase in latency of spiking. In fact, all the thalamic units that we considered for further analysis showed only moderate spike frequency adaptation, with a maximal increase in latency of 8ms when comparing responses to the first and last stimulus of the train (mean first spike latency (FSL), latency shift from Not-Adapted to Adapted = $4.28 \text{ ms} \pm 2.32 \text{ ms}$ (mean \pm SEM), $n=21$ cells from rat; $3.71 \pm 3.11 \text{ ms}$ (mean \pm SEM), $n = 39$ neurons, $N = 4$ mice, Figure 2-2D right, inset). Furthermore, the response latency of thalamic neurons measured here is consistent with the latency of VPm neurons (peak latency <10 ms) identified through a genetic validation approach (Wright et al. 2021b). Note that there remains a small possibility that a subset of the thalamic units is POm in origin, and project to S1 inter-barrel areas (septa). However, this is unlikely to be the case

for the thalamocortical pairs that showed monosynaptic connectivity, given that these thalamic and cortical units demonstrated mostly single whisker receptive fields (Furuta et al. 2009) and the likelihood of detecting synaptic connections in POm-S1 inter-barrel areas is much lower. Finally, a recent study showed that POm cells remain largely inactive (close to zero spontaneous firing rate) under isoflurane anesthesia (Zhang and Bruno 2019), making them extremely difficult to locate and record from under the conditions of this study, which when combined with the other factors described above make it unlikely that any of the recordings here are POm in origin. Again, note that the challenges here are somewhat specific to this particular brain region, but achieving definitive recordings in other brain regions would likely have similar challenges to those described here.

Previous studies have shown that the convergence of thalamic inputs onto topographically aligned cortical layer 4 neurons is generally relatively high, but with the probability of contacting regular spiking units (RSUs) much lower than fast spiking units (FSUs) (Bruno and Simons 2002; Swadlow 2003). We recorded from well-isolated cortical layer 4 neurons (see Figure_A-1C) at a cortical depth taken from micromanipulator readings (Rat: 803.28 ± 175.28 μm , mean \pm SEM, $n=21$, data not shown; Mouse: 350-700 μm , $n=11$, data not shown). All cortical units included in this study were putatively layer 4 neurons. The mean first spike latency of cortical units in rat was $11.4 \text{ ms} \pm 1.77 \text{ ms}$ (mean \pm SEM, $n=22$) and $12.6 \pm 2.06 \text{ ms}$ (mean \pm SEM, $n=11$) for mouse. We found that the relative latency difference between VPm and S1 layer 4 in aligned regions was comparable to the expected synaptic delay between VPm and S1 layer 4 (differences between VPm-S1 were $\sim 3 \text{ ms}$ for both rat and mouse). An example of the response to a punctate whisker

stimulus for a pair of VPm and S1 FS units with mean first-spike latency of 7.5 ms and 11.2 ms is shown on the left of Figure 2-2E..

2.3.3 Inferring connectivity in the context of a signal detection framework

In general, neurons in the central nervous system require the concerted action of a relatively large number of pre-synaptic inputs to produce an action potential (Bruno and Sakmann 2006). Thus, the relationship between pre- and post-synaptic neurons is tenuous at best, reflected in often a very subtle increase in the probability of firing of the post-synaptic neuron a few milliseconds after the firing of a pre-synaptic neuron. The analysis of spike trains from a pair of neurons can thus be utilized for a simple binary classification of a neuronal pair either being ‘not connected’ or ‘connected’ (Figure 2-3A).

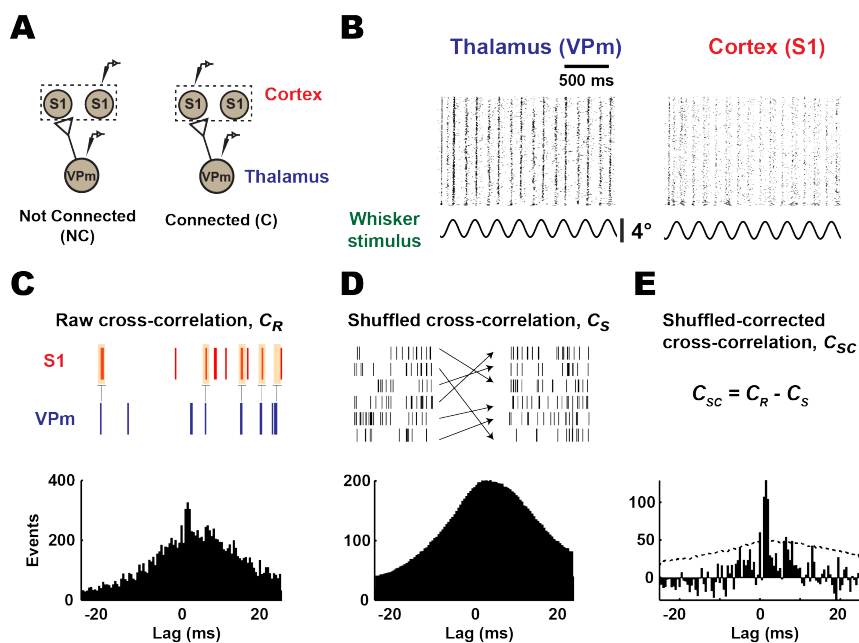


Figure 2-3. Monosynaptic connectivity inference using cross-correlation analysis.

A. Inferring monosynaptic connectivity from extracellular recordings performed in topographically aligned thalamocortical regions in vivo resulted in binary consequences. A pair of neurons can be putatively classified as connected or not connected, as shown in

the schematic. S1, primary somatosensory cortex; VPM, ventral posteromedial nucleus. **B:** Raster plots showing whisker-evoked spiking response under low-velocity sinusoidal stimulation (mean velocity: 25°/s) for a representative example from thalamus and cortex in a rat. **C.** All cross correlograms were computed using VPM spike train as a reference. Occurrences of cortical spikes were measured at various time lags (25-ms window before and after a thalamic spike, with 0.5-ms step size; see METHODS). **D.** Stimulus-driven cross correlograms were constructed between the original reference VPM spike trains and the trial-shuffled cortical spike trains. **E.** Shuffled-corrected cross correlograms were generated by subtracting the mean of shuffled cross correlograms (averaged from 1,000 iterations) from the raw cross correlograms. Dotted gray lines denote 3.5 standard deviation of the shuffled distribution.

In order to infer connectivity, for each recorded pair of neurons, the raw spike cross-correlogram is calculated using standard approaches (C_r , Figure 2-3C) (see Methods), effectively yielding a histogram of cortical firing relative to thalamic spike times. Because the analysis is based on spiking activity, and the baseline spiking activity can often be relatively low, we drove the thalamocortical circuit in-vivo with a weak whisker stimulus (Figure 2-3B, sinusoidal deflection, 4 Hz, mean velocity: 25 °/s), which is known to enhance firing rates with minimal impact on firing synchrony across neurons (Bruno and Sakmann 2006). To correct for correlated stimulus-locked activity, we generated a shuffled-corrected spike cross-correlogram (C_{sc} , Figure 2-3E by subtracting the trial shuffled spike cross-correlogram (C_s , Figure 2-3D) from the raw spike cross-correlogram. The “shuffled cross-correlogram” is generated using the same procedure used for the raw cross-correlogram, except that the trials of the thalamic and cortical spiking activity are randomized relative to each other. This effectively destroys any elements of the cross-correlogram that are not due to the stimulus. Shown in this example is the qualitative signature of monosynaptic connectivity – a prominent peak in the shuffled-corrected cross-correlogram for small positive lags that would be consistent with a single synaptic delay.

Then, to conclude that a neuronal pair was ‘connected’, we adopted two criteria that expanded from previous studies (Bruno and Sakmann 2006; Reid and Alonso 1995; Swadlow and Gusev 2001) based on both the raw and shuffled-corrected cross-correlogram: (Criterion 1) a notable sharp, millisecond-fine peak is observed within a narrow lag of 1-4 ms after a thalamic spike, and (Criterion 2) this fast ‘monosynaptic peak’ is significant or still present after accounting for (subtracting) stimulus-induced correlation. Note that a peak is defined as the bin in the raw cross-correlogram (0.5 ms bin size) that contains the maximum number of events. In order to fulfill both criteria, we required that the peak detected in the 1-4 ms range to have the largest correlation out of all the bins in the range of ± 25 ms window and this correlation is significant (>3.5 SD) against shuffled data. For the example ‘connected’ pair in Figure 2-3C-E and a separate ‘not connected’ pair, Criterion 1 is evaluated from the raw cross-correlation as shown in Figure 2-4A. For the ‘not connected’ example (raw cross-correlogram on the left), a peak was detected outside the central 1-4ms lag, and thus fails Criterion 1. The example ‘connected’ pair, the raw cross-correlogram on the right, exhibits a peak within the central 1-4 ms lag (shown as a vertical gray band), and thus passes Criterion 1. Figure 2-4A illustrates how Criterion 2 is estimated from the shuffled-corrected cross-correlation. We evaluate the prominence of the peak relative to a distribution of peak magnitudes (same bin with maximum number of events) from the shuffled cross-correlograms (1000 iterations). Specifically, we define the metric related to Criterion 2 as the peak height, h , computed using the maximum of the C_{sc} (0.5 ms bin size) within 1-4 ms lags, normalized by the standard deviation of the shuffled cross-correlogram. This metric is thus the number of standard deviations the peak of the shuffled-corrected cross-correlogram within the 1-4ms lag is above the shuffled

distribution. This is shown in more detail for this example in the inset in the bottom row of Figure 2-4A, where the central portions of the shuffled-corrected cross-correlograms are shown for each case. In order to pass Criterion 2, the peak height of the shuffled-corrected cross-correlograms must be greater than 3.5 standard deviations of the shuffled data, which corresponds to a 99.9% confidence interval for each bin.

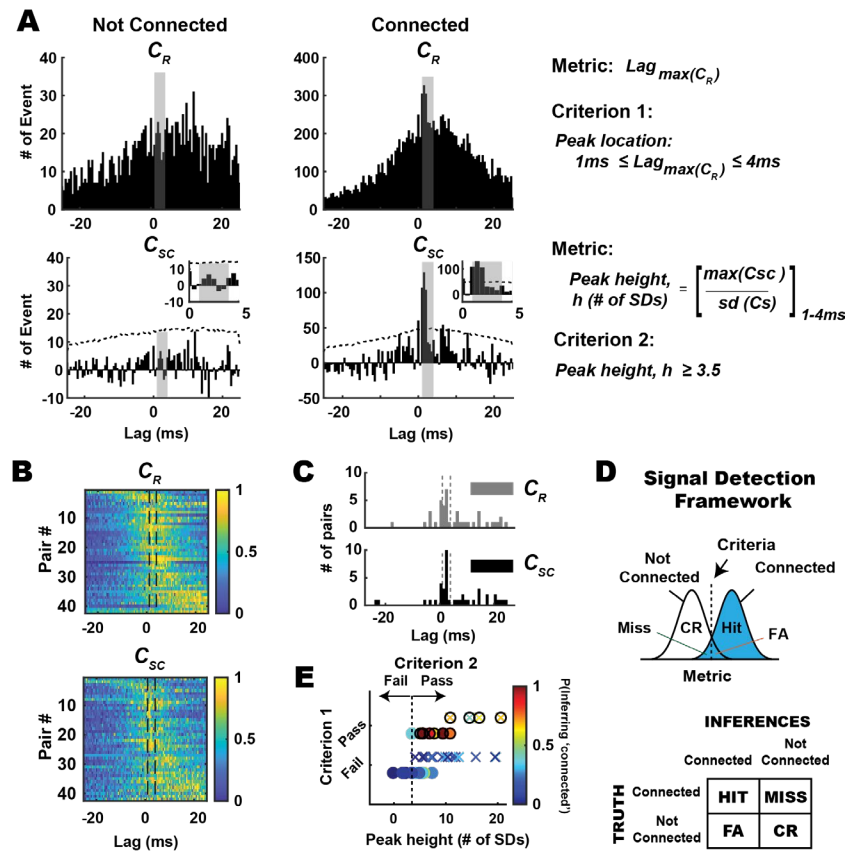


Figure 2-4. Evaluation of monosynaptic connection inference in the context of a signal detection framework.

A. In the context of signal detection framework, we defined 2 distinct metrics and criteria to classify neuronal pairs into connected and not-connected distribution. Shown here are representative example pairs from each condition. Top: note the qualitative difference in raw cross correlograms (CR), one with broad and distributed spikes in cross correlogram (left) and another with sharp peaks (right) in 1–4 ms time lags (shaded gray). The first metric is the maximum peak of the raw cross correlogram (CR), and criterion 1 was fulfilled if the maximum peak of the raw cross correlograms was within 1–4 ms lag. Bottom: after correcting for stimulus-driven correlations, we further quantified the

significance of the peaks detected in raw cross correlogram. Hence, the second metric used here is the peak height within the window of interest (1–4 ms bin), measured as maximum peak value in shuffled-corrected cross correlogram (CSC), normalized to the number of standard deviations (SDs) with respect to the shuffled distribution. Criterion 2 was fulfilled if the peak exceeded 3.5 SDs of the shuffled distribution. **B.** As expected, the majority of simultaneously recorded thalamocortical pairs exhibited peak correlation after 0-time lag ($n = 42$ pairs; rats: 22, mice: 20). Histograms show the number of events in each bin of raw cross correlograms (top) and shuffled-corrected cross correlograms (bottom), sorted by latency of maximum peak in the cross correlograms. Data were normalized to maximum peak, and the colors in each row show the number of events for an individual pair, normalized to maximum peak. **C.** Distribution of the lags of the peak location in the raw and shuffled-corrected correlograms across all recorded pairs. Note that the peak locations for raw and shuffled-corrected correlograms were largely the same, shifted only by 1–2 bin size (0.5-ms bin). **D.** Within this framework, 4 possible outcomes are possible: hit: connected and inferred to be connected; miss: connected but inferred to be not connected; false alarm (FA): not connected but inferred to be connected; correct rejection (CR): not connected and inferred to be not connected. **E:** In this context, we found that 11/42 pairs have putative monosynaptic connection (denoted by filled circles) and 31/42 pairs. Pairs were not connected ($n = 22$ pairs, $N = 12$ rats; $n = 20$ pairs, $N = 1$ mouse). Note that criterion 1 was a binary classification: pairs having peak locations from their raw cross correlograms within the 1–4 ms lag pass criterion 1, and those that do not fail criterion 1. For criterion 2, the dashed vertical line represents 3.5 SDs for the peak height metric: pairs having peak height above this criterion line pass criterion 2. Only pairs that passed both criteria 1 and 2 were classified as connected [anything to the right of the vertical dashed line in E (top row)], and the rest were classified as not connected. For each recorded pair, probability of inferring monosynaptic connection (i.e., probability of bootstrapped data satisfying criteria 1 and 2) is depicted with a color bar. Note that 1,000 iterations were performed for each data set.

Thus, we conclude that the shuffled-corrected cross-correlograms on the left fails Criterion 2 as the peak falls below the criterion line (3.5 SD, depicted as dashed line) whereas the shuffled-corrected cross-correlograms on the right passes Criterion 2. Note that for the “not connected” pair shown in Figure 2-4A, the shuffled-corrected cross-correlogram also revealed the presence of the global peak outside the 1-4 ms central lag, similar to that of the raw cross-correlogram. Thus, it is possible to utilize the shuffled-corrected cross-correlogram for the evaluation of Criterion 1 in some cases, but overall, we found that Criterion 1 was more robustly evaluated utilizing the raw cross-correlogram. The raw and shuffled-corrected correlograms for all recorded thalamocortical pairs are

shown in Figure 2-4B- normalized to the peak in each correlogram, ordered from earliest to latest peak, top to bottom. The vertical lines in these plots highlight the 1-4ms lag range described in Figure 2-4A. Figure 2-4C shows the distribution of the lags of the peak location in the raw and shuffled-corrected correlograms across all recorded pairs. Overall, the peak locations for raw and shuffled-corrected correlograms were similar, shifted only by 1-2 bin size (0.5ms). For all the monosynaptically connected pairs in this paper, the mean peak location was 1.18 ± 1.08 ms (mean \pm SEM, $n = 11$), and with a median of 1.5 ± 0.89 ms.

Note that to be classified as connected, a candidate pair of neurons must pass both Criterion 1 and Criterion 2. Using these metrics and criteria, we can consider the result of cross-correlation analysis for each pair as an inference problem in the context of a signal detection framework, where we conceptualize the distribution of metric values for the non-connected pairs as “noise”, and for the connected pairs, as “signal”. Applying the criteria on the metric values yields four possible outcomes: Hit (connected pair classified/inferred as such), Miss (connected pair classified/inferred as ‘not connected’), False Alarm (not-connected pair classified/inferred as ‘connected’), and Correct Reject (not-connected pair classified/inferred as such) (Figure 2-4D). With these metrics and criteria, we classified measured neuronal pairs into ‘connected’ and ‘not-connected’ distributions, with 11/42 pairs having a putative monosynaptic connection and 31/42 pairs having no apparent connection (Figure 2-4D bottom, Rat: $n = 22$ pairs, Mouse = 20 pairs). For Criterion 1, this was a binary classification due to biological constraints (single synaptic delay) – pairs having peak locations from their raw cross-correlograms within the 1-4ms lag pass Criterion 1, and those which do not, fail Criterion 1. For Criterion 2, the dashed vertical

line represents the 3.5 SD for the peak height metric – pairs having peak height above this criterion line pass Criterion 2. Only pairs that passed both Criterion 1 and 2 in Figure 2-4E were classified as ‘connected’ (anything to the right of vertical dashed line and on the top row) and the rest were classified as ‘not connected’. Note that while this is a binary classification, and the end-result is a labeling of a pair as ‘connected’ or ‘not-connected’, not all classifications are equivalent, with some having substantially more confidence in the classification than others. By utilizing a bootstrapping approach (see Methods) and evaluating the likelihood of specific outcomes using the pre-defined metrics and criteria for each recorded pair, we were able to attach a probability measure (Figure 2-4E bottom, color bar, P(Infering ‘connected’)) along with each connectivity inference. In Figure 2-4E bottom, some of the cases that passed Criterion 1 have peak heights that are substantially far away from the line for Criterion 2. As expected, the likelihood of inferring monosynaptic connection for these cases was higher ($\sim 0.6-1$) and thus we have more confidence in the assertion, as compared to cases that are very close to the criterion line for Criterion 2, or failed Criterion 1.

2.3.4 Probabilistic measure of connectivity inference across brain structures in large-scale recordings

Through the advent of high channel-count electrophysiological recording techniques (Chung et al. 2019; Jun et al. 2017; Rios et al. 2016), the diversity of recording quality, cell type, and possibilities for connectivity has expanded tremendously. To demonstrate how our framework can be beneficial, Figure 2-6 shows an example of simultaneous topographically aligned recordings from silicon multi-electrode probes

inserted in VPM thalamus (Figure 2-6A) and S1 (Figure 2-6B). Specifically, focusing on portions of the probes that were assessed to be topographically aligned, a subset of channels from the VPM probe (Channels A-D) yielded 5 thalamic neurons (VPM 1-5), while a subset of channels from the S1 probe (A-D) yielded 4 cortical neurons (S1 1-4). These neurons were recorded during weak sinusoidal (25 deg/s, 4Hz) whisker stimulation. In this multi-dimensional analysis, each of the 20 thalamocortical pairs were assessed for the possibility of connectivity. Table 1 in Figure 2-6C shows the matrix of binary outcomes of monosynaptic connectivity inference from cross-correlation analysis of the full dataset across the recording sites. Out of the 20 VPM-S1 pairs, 4 were judged to be connected according to our criteria. Note that while the connectivity from an individual barreloid to the homologous cortical barrel is relatively high (it has been estimated that approximately 1 in 3 VPM neurons within a barreloid is connected to a particular neuron in cortical layer 4 of the homologous barrel (Bruno and Sakmann 2006)), the relatively stringent criteria of the inference coupled with other factors such as the potential to record from multiple nearby VPM barreloids and variable single unit quality make this outcome typical. Shown in Figure 2-6C Table 2 are the probabilities of connectivity associated with each pair using the bootstrapping method ($n = 1000$ iterations) on the data (Table 2), as previously described. In general, the binary inference for a particular pair corresponded to the bootstrapped confidence levels – connected pairs had a relatively high probability of connectivity from the bootstrapping (see all ‘connected’ pairs in Figure 2-5) while not connected pairs had a relatively low probability of connectivity from the bootstrapping ($p < 0.4$). We found that the binary outcomes of monosynaptic connectivity inference could result in different ranges of probability of inferring monosynaptic connection (0.4-1). One

factor that could affect this probability is data-length. Not surprisingly, we found that the ‘connected’ pair that yielded the lowest probability in this matrix ($p = 0.41$) had about 3900 spikes (in terms of geometric mean), as compared to the others (4900, 6900 and 10000 spikes).

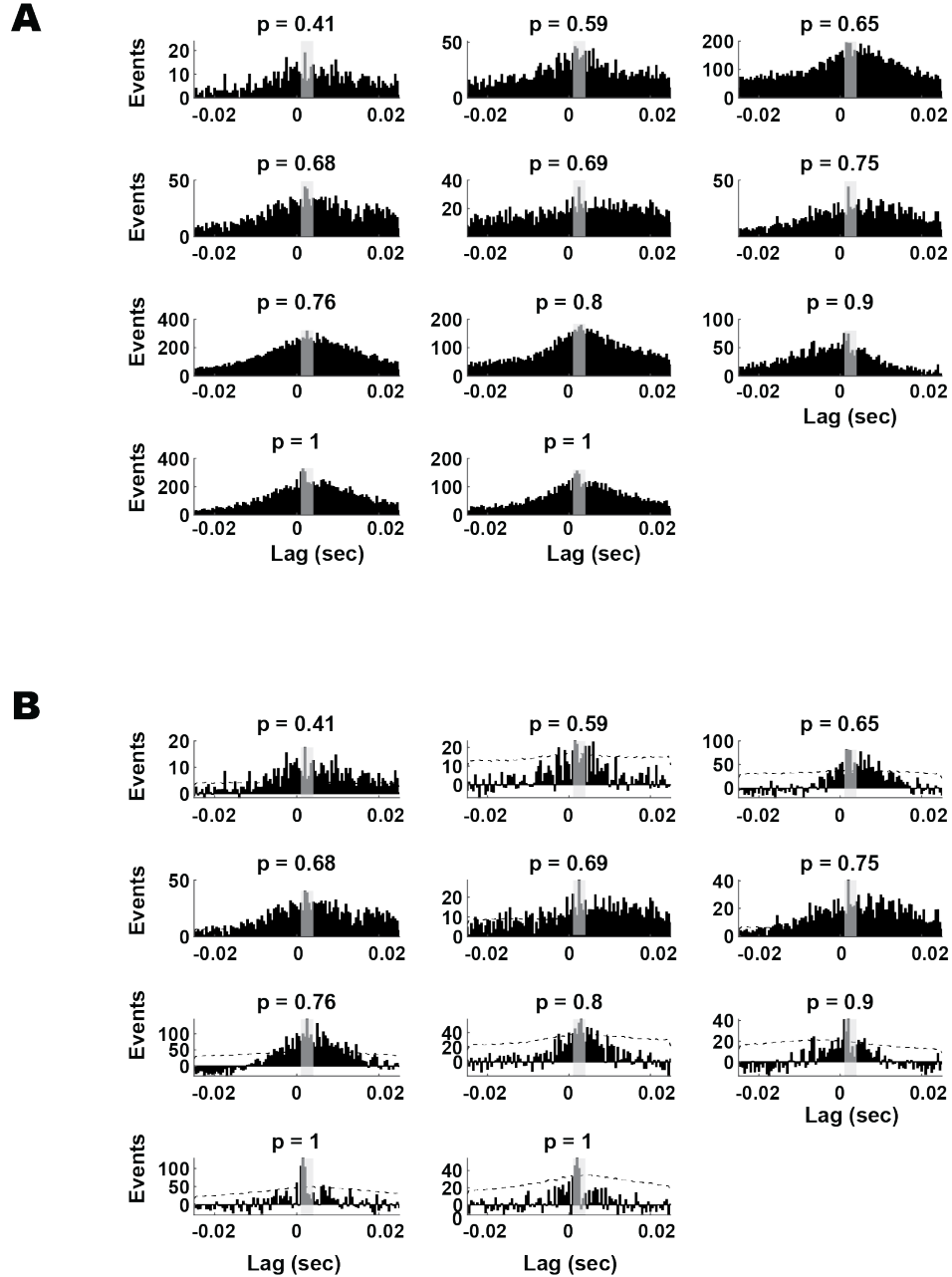


Figure 2-5. Raw and shuffled-corrected cross-correlograms of ‘connected’ pairs in rat and mouse.

A. Raw cross-correlograms of all ‘connected’ pairs in Figure 2-4E. **B.** Corresponding shuffled-corrected cross-correlograms in A. P-value above each plot represents the probability of a correct inference associated with each ‘connected’ pair (related to Figure 2-4 and Figure 2-6).

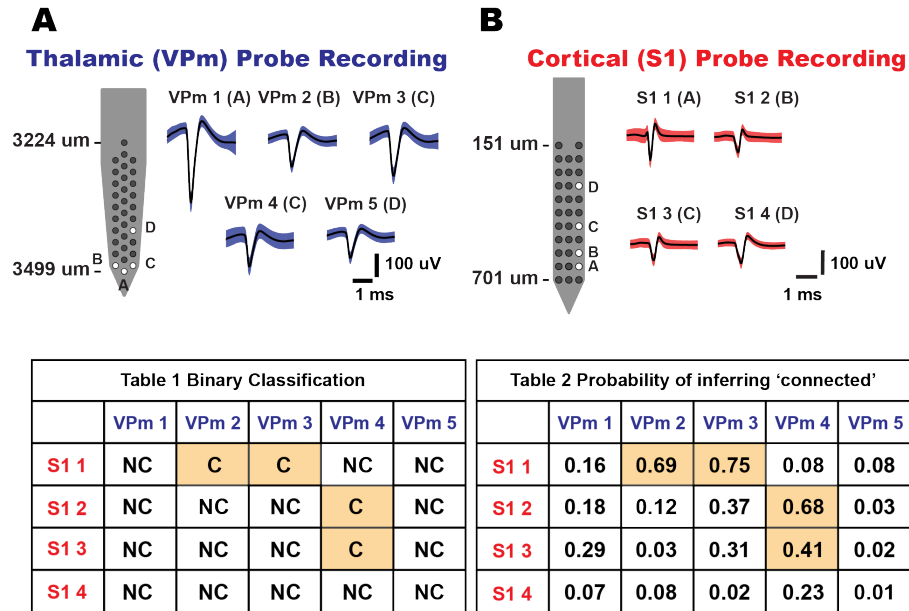


Figure 2-6. Connectivity matrix for topographically aligned simultaneous multi-site recordings.

A: Thalamic [ventral posteromedial nucleus (VPm)] probe recording. Five whisker-responsive thalamic units were isolated from 32-channel silicon probe sites, labeled A–D. Mean waveforms of single units are shown on right (shaded region indicates 1 standard deviation of spike amplitude) ($n = 5$ neurons). B: Cortical [primary somatosensory cortex (S1)] probe recording. Four whisker-responsive units, putatively from layer IV barrel cortex, were isolated from 32-channel silicon probe sites, labeled A–D. Mean waveforms of units are shown on right (shaded region indicates 1 standard deviation of spike amplitude) ($n = 4$ neurons). Table 1 shows binary outcomes of the monosynaptic connectivity inference based on criteria 1 and 2 of cross correlation analysis. Table 2 shows the connectivity matrix tabulating the probability of inferring a putative monosynaptic connection using the bootstrapping method for each thalamocortical pair in Table 1 (bootstrap iteration = 1,000). C, connected; NC, not connected.

2.3.5 Data-length effect on monosynaptic connection inference

As previously shown, inference of monosynaptic connectivity using cross-correlation analysis on extracellular signals is highly dependent on the amount of collected data. Based on existing literature, the recommended numbers of spikes were highly variable, ranging from 2000 to 10000 spikes (Swadlow and Gusev 2001; Wang et al. 2010),

but were presented more as a “rule-of-thumb” than based on systematic evaluation. Here, we systematically evaluated data-length dependence effects on the connectivity inference outcomes. More specifically, we measured the data-length effect by performing bootstrapping on the full dataset by randomly selecting segments of data of increasing duration, as illustrated in Figure 2-7A. Note that for this analysis, the effects of data-length were evaluated in the context of Criterion 2, as this is the measure more prominently affected by data-length. In general, the analysis is primarily sensitive to the number of spikes used in the estimates, rather than the time duration of experimental data collection, and is sensitive to the number of both VPm and S1 spikes (i.e., sufficient spiking from both is requisite). For this reason, we utilized the geometric mean of the number of VPm and S1 spikes, calculated as the square root of the product of the number of VPm and S1 spikes. Because we did not have access to an established “ground truth” of a pair being either connected or not connected, we utilized example pairs in which the analysis revealed a very clear classification, which we subsequently utilized as ground truth for the analysis.

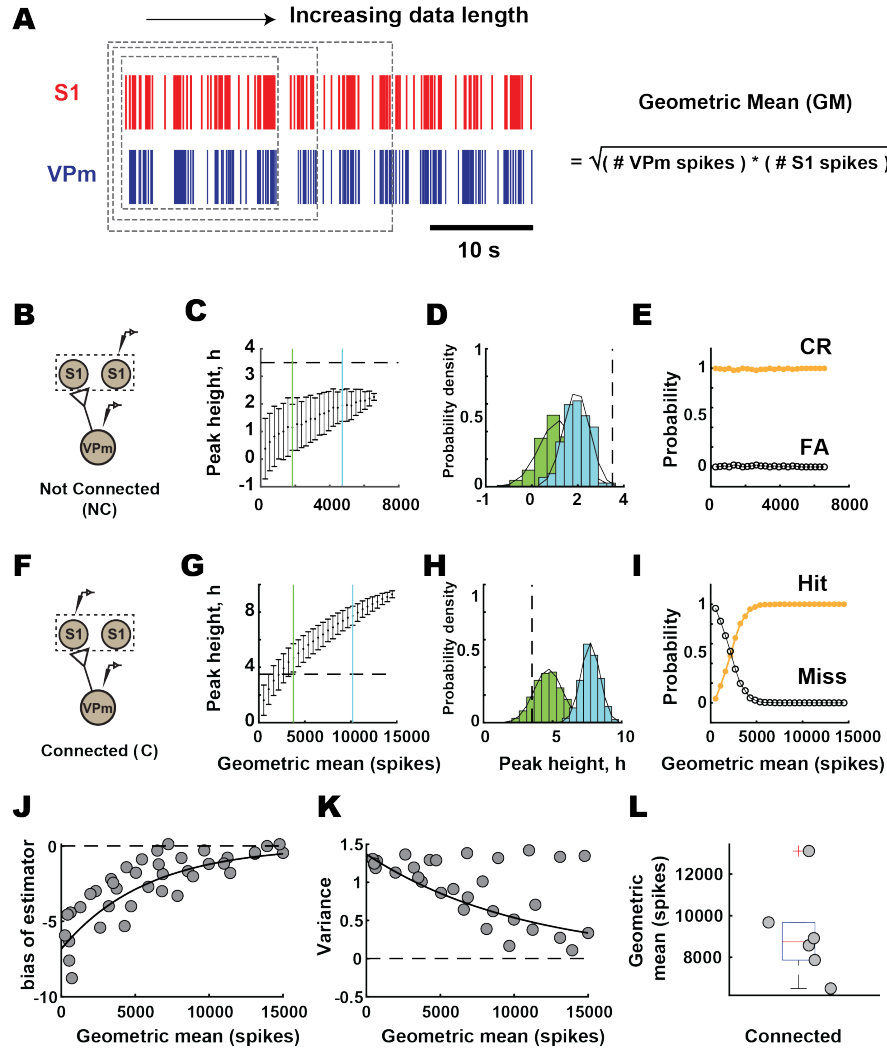


Figure 2-7. Data length dependence effect on monosynaptic connection inference.

A: Data length dependence effect on connectivity inference was evaluated with a subsampling method. Data length was measured in terms of geometric mean number of spikes, which was calculated by taking the square root of the product of total ventral posteromedial nucleus (VPm) and primary somatosensory cortex (S1) spikes. Random subsampling of the data set was performed in the unit of trials with 1,000 iterations for each condition. **B:** Representative example pair of neurons from not-connected distribution in a rat. **C:** Mean and standard deviation of peak height from cross correlogram were computed for each subsample of not-connected example. Blue line, short-data length condition (GM: 1,837 spikes); green line, long-data length condition (GM: 4,730 spikes). **D:** Distribution of peak height after bootstrapping for 2 data lengths labeled in part I. **E:** Probability of outcome for this example. CR, correct reject; FA, false alarm. **F–I:** Similar to B–E but for connected example in a rat [blue (GM): 3,760 spikes, hit rate 87.7%, miss rate 12.3%; green (GM): 10,201 spikes, hit and miss rates 100%, 0%] (also see Figure 2-10; see <https://doi.org/10.6084/m9.figshare.14393582.v1>). **J:** Bootstrap estimator of bias for each data length. Scatterplot of population data for connected pairs (n = 6 pairs, N = 3 rats).

Solid line, exponential fit ($R^2 = 0.76$). **K**: Variance of peak height at each data length for pairs shown in J. Solid line, 1st-order polynomial fit ($R^2 = 0.62\%$). **L**: Geometric mean for all connected pairs (median: 8,741 spikes, $n = 6$ pairs, $N = 3$ rats).

Shown are the results from such an analysis for a ‘not connected’ pair (Figure 2-7 B-E) and a ‘connected’ pair (Figure 2-7 F-I). We found that, when a functional connection was obviously not present, the correlated firing activity between a pair of neurons was indistinguishable from that expected from stimulus-induced correlation, reflected in the metric remaining well below the criterion line (3.5 SD) for all values of data-length, while however steadily increasing as a function of the geometric mean (also accompanied by a decrease in the variability of the metric as reflected in the SEM) (Figure 2-7C). Figure 2-7D shows the distributions of the estimated connectivity metric h for two particular data-lengths (geometric means of 1837 spikes and 4730 spikes), relative to the criterion line. Both of these distributions are clearly to the left of the criterion line, corresponding to high correct reject and low false alarm rates, relatively unaffected by data-length (Figure 2-7E).

In contrast, when a functional connection was apparent, limited data confounded the inference of ‘connected’ as the metric remained below the criterion line for smaller data-lengths (Figure 2-7G). For two particular data-lengths (geometric means of 3760 and 10201 spikes), the distributions of the estimated connectivity metric h are shown in Figure 2-7H., relative to the criterion line. While the longer data-length resulted in a distribution of the peak height that was clearly above the criterion line (easily passing Criterion 2), the shorter data-length resulted in a distribution whose mean was above the criterion line (barely passing Criterion 2), but with a substantial portion of the distribution below the criterion line, resulting in a hit rate of 87.7% and miss rate of 12.3%. We found that the

data-length required to reach a consistently correct inference was approximately 5000 spikes for this example (Figure 2-7I).

From the results in Figure 2-7 B-E and Figure 2-7 F-I (also see Figure 2-10), it appears that data-length was critical only for correctly identifying a connected pair, and did not directly affect the inference related to a “not connected” pair – in other words, the analysis is prone to type II errors as opposed to type I, and the type II error is strongly dependent upon data-length. It is important to point out that the data-length needed for sufficiently reducing the probability of error in the inference in Figure 2-7I is dependent upon the ground truth value for the connectivity metric h , as well as the variance in the estimator. We thus analyzed the estimator bias and variance across six ‘connected’ pairs, as a function of the data-length, which we could systematically vary by utilizing sub-sampling of the full datasets. Figure 2-7J shows the bias in the estimator for the connectivity metric h , as a function of the geometric mean number of spikes, with generally a negative bias (an underestimate) and a clear exponential decrease in bias with data-length as expected, as the full data-length is approached. Figure 2-7K shows the corresponding variance in the estimator of the connectivity metric h , again as a function of the geometric mean number of spikes. Although some of the measures exhibited an apparent invariance to the data-length, overall, this quantity decreased exponentially with increasing geometric mean number of spikes, again as expected. For the set of ‘connected’ pairs of thalamic and cortical neurons here, the geometric mean number of spikes required for the lower bound of resampled data to pass Criterion 2 is shown in Figure 2-7L, with a median of approximately 9000 spikes.

2.3.6 *Thalamic synchrony effects on monosynaptic connection inference*

Without having access to the subthreshold activity of the postsynaptic cortical neurons, assessment of connectivity through the co-occurrences of spiking activity in thalamic and cortical neurons often necessitates activation of the intact circuitry with exogenous stimulation due to relatively low intrinsic spontaneous firing rates. The analysis of Figure 2-7 revealed a clear motivation for acquiring larger numbers of spikes, which can obviously be facilitated through increased mean firing rates. In sensory pathways, previous studies have used sensory stimuli of varying strengths to evoke higher firing rate in primary sensory areas (Bruno and Sakmann 2006; Reid and Alonso 1995; Sedigh-Sarvestani et al. 2017; Wang et al. 2010), citing a rule-of-thumb which involves increasing the number of spikes through external stimulation, but not with a stimulus so strong as to induce stimulus-driven synchronization in spiking. Although this approach is logical, it remains ad hoc, and the exact ramifications are not clear. Here, we utilized silicon multi-electrode probes in the thalamic VPm and S1 layer 4 to quantify changes in neural activity across spontaneous and stimulus driven conditions and performed analyses to systematically evaluate the potential effects of stimulus-driven changes in firing rate and synchrony on the monosynaptic connection inference between VPm and S1 pairs. Figure 2-8A shows simultaneous recordings from two thalamic neurons (VPm1 and VPm2) within the same thalamic barreloid and two corresponding cortical S1 neurons in the homologous barrel column. For this example, VPm Unit 1 and S1 Unit 1 were revealed to be ‘connected’, while VPm Unit 2 and S1 Unit 2 were clearly ‘not connected’. Under increasingly stronger stimulus drive, from spontaneous (left), to weak-sinusoidal whisker stimulus drive (middle), and to strong repetitive, punctate whisker stimulus drive (right), there is a general

increase in firing rate across the recorded cells in both VPm and S1 (Figure 2-8B). In addition to the modulation of mean firing rate, we found that increasing stimulus drive affected the inference of connectivity by producing inconsistent conclusions across stimulus conditions, especially obvious with increasingly strong stimuli. Interestingly, we found that this preferentially affected the location of the peak in the cross-correlogram, which is associated with Criterion 1 evaluated through the raw cross-correlogram. Figure 2-8C shows the raw and shuffled-corrected spike cross-correlograms across the stimulus conditions for the connected pair VPm Unit 1-S1 Unit 1, and Figure 2-8D shows this for the not-connected pair VPm Unit 2-S1 Unit 2. Note that we were able to maintain stable recordings for this particular group of neurons over a relatively long experimental time period, enabling us to collect a sufficient number of spikes in the spontaneous condition in order to make inferences regarding connectivity, which we can treat as ground truth here (VPm Unit 1-S1 Unit 1 connected, VPm Unit 2-S1 Unit 2 not-connected). First considering the connected pair VPm Unit 1-S1 Unit 1 (Figure 2-8C), we found that the inference remained consistent ('connected') for spontaneous (I) and sinusoidal (II) stimulus conditions as it passed both Criterion 1 and 2. However, for the repetitive transient (III) stimulus condition (bottom row), while the peak height in the shuffled-corrected cross-correlogram exceeded the criterion line (thus satisfying Criterion 2, Figure 2-8C bottom panel), there was a disappearance of an isolated peak in the 1-4 ms lag of the raw cross-correlogram, which is a violation of Criterion 1. This led to the incorrect inference of 'not connected' for the case of the strong, transient stimulus, or a "miss" in the language of signal detection theory. In our analysis, we have 12 thalamocortical pairs for which we have all stimulus conditions, where we consider the spontaneous condition as the "ground

truth". Of these 12 pairs, 3 pairs were connected (C) and 9 not connected (NC), as determined from the spontaneous condition, which we consider "ground truth". For the 9 NC pairs, 6 pairs were incorrectly classified as C in the strong (transient) stimulus case, and the remaining 3 pairs continued to be correctly classified as NC. For the 3 C pairs, 2 pairs were incorrectly classified as NC in the strong (transient) stimulus case, and the remaining 1 pair continued to be correctly classified as C. For this relatively small number of pairs, it is difficult to identify a particular pattern in this, but we can generally say that both types of errors can emerge from the strong stimulus that synchronizes the thalamic population, as we also demonstrate in the simulations.

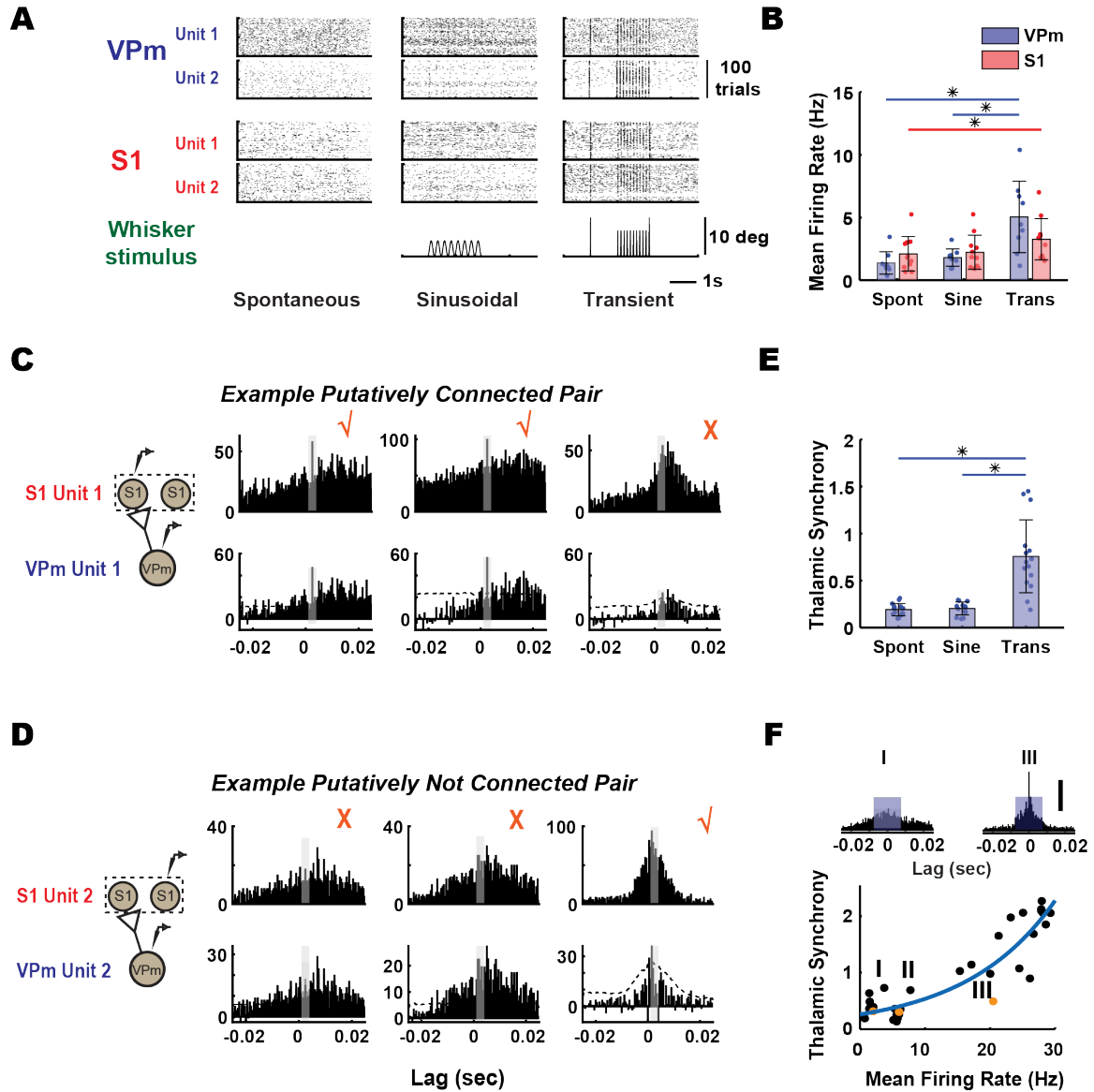


Figure 2-8. Thalamic synchrony effect on monosynaptic connection inference.

A: Raster plots from simultaneously recorded thalamic and cortical units under spontaneous (no stimulus; Spont), sinusoidal stimulus (mean velocity: 25/s; Sine), and transient inputs (1,200/s; Trans) in a mouse. S1, primary somatosensory cortex; VPm, ventral posteromedial nucleus. **B:** Mean firing rates of thalamus (VPm, blue) and cortex (S1, red) of neuronal pairs were quantified across all 3 stimulus conditions. VPm: spontaneous: 1.38 ± 0.89 Hz, sinusoidal: 2.11 ± 1.37 Hz, transient: 5.05 ± 2.85 Hz; mean \pm SE ($n = 9$ neurons); S1: spontaneous: 2.11 ± 1.37 Hz, sinusoidal: 2.23 ± 1.36 Hz, transient: 3.27 ± 1.65 Hz ($n = 11$ neurons, $N = 1$ mouse) ($P < 0.05$, Wilcoxon signed-rank test with Bonferroni correction). **C:** Monosynaptic connectivity inference for 1 representative example of connected thalamocortical pair from mouse. Checkmark symbols indicate that the pair is being classified as putatively connected; cross symbols indicate that the pair is being classified as not connected. **D:** Same as C but for not-

connected example. **E**: thalamic synchrony was computed across 3 stimulus conditions, calculated as number of synchronous events between 2 thalamic units that occur within central window (± 7.5 ms). ($P < 0.05$, Wilcoxon signed-rank test with Bonferroni correction). Spontaneous: 0.20 ± 0.07 ; sinusoidal: 0.19 ± 0.06 ; transient: 0.76 ± 0.39 ; mean \pm SE ($n = 9$ neurons, 15 pairs, $N = 1$ mouse). **F**, top: raw spike cross correlograms for the 2 VPM units shown in A (top) in spontaneous and transient stimulus conditions. (I, spontaneous; III, transient). Blue box on each cross correlogram represents the central window (± 7.5 ms) used for thalamic synchrony computation. Scale bar represents 100 spikes in cross correlograms. Bottom: the relationship between thalamic synchrony and mean firing rate of respective thalamic pairs was quantified across various stimulus conditions, including spontaneous, sinusoidal, and transient stimuli with 6 different velocities ($n = 5$ neurons, 10 pairs, $N = 1$ mouse). Orange symbols represent thalamic synchrony across 3 stimulus conditions for example thalamic pair (I, spontaneous; II, sinusoidal; III, transient). Blue line shows exponential fit of the relationship.

Turning to the ‘not-connected’ pair VPM Unit 2-S1 Unit 2 in Figure 2-8D, note that for the spontaneous (I) and sinusoidal (II) case, while the peak height of the shuffled-corrected cross-correlogram exceeded 3.5 SD (thus passing Criterion 2, not shown), we correctly inferred ‘not connected’ for these stimulus conditions given the violation of Criterion 1. Surprisingly, we incorrectly inferred ‘connected’ for the repetitive transient (III) stimulus condition as fast peaks emerged in the 1-4 ms lag of the raw cross-correlograms, satisfying Criterion 1 (and also Criterion 2, not shown), or a “false alarm” in the language of signal detection theory. We thus encountered two kinds of errors when utilizing exogenous stimulation to increase neuronal firing rates – “misses” and “false alarms”, both linked to Criterion 1, due to appearance of spurious peaks in 1-4 ms lag in the cross-correlogram.

In previous studies, increase in stimulus-driven firing rate has been shown to couple with higher degree of synchronization within and across neural circuits (Temereanca et al. 2008; Wang et al. 2010) that can potentially dominate the temporal relationship of the network dynamics revealed by correlational analysis (Ginzburg and Sompolinsky 1994).

This highlights the issues underlying the tradeoff between firing rate and synchronization of the local network that are intrinsic to the correlational analysis used for monosynaptic connection inference. Several paired recording studies have approached this problem by collecting spontaneous spiking data (Swadlow and Gusev 2001), where presumably the spontaneous activity is less synchronous than stimulus driven activity, or by providing weak or non-synchronizing inputs to probe the circuit (Bruno and Sakmann 2006; Bruno and Simons 2002; Reid and Alonso 1995). However, some degree of synchronization is always present, and a direct understanding of the potential effects and implications of population synchronization of presynaptic neurons on monosynaptic connection inference is lacking. To relate the amount of synchronization across the thalamic units with the increase in stimulus strength, we quantified synchrony using the spike cross-correlogram measured across thalamic pairs. Specifically, the synchrony was defined as the number of spikes of the cross-correlogram within a window of ± 7.5 ms, normalized by the number of thalamic spikes (see Methods). Population data showed significant increases in thalamic synchrony comparing spontaneous and transient conditions, as well as sinusoidal and transient conditions (Figure 2-8E, $n = 15$ pairs). The raw spike cross-correlograms for the two VPM units shown in the top row of Figure 2-8A are shown in Figure 2-8F (top and orange symbol in bottom), illustrating an increase in the central peak of the cross-correlogram and thus the thalamic synchrony, note the emergence of sharp peaks from spontaneous to transient stimulus. The nature of the stimulus thus strongly affects the synchrony, but also strongly affects the firing rate, suggesting a more general relationship between firing rate and synchrony. To more generally quantify the relationship between thalamic synchrony and mean firing rates, across several experiments we collected

thalamic responses to different stimuli (spontaneous, sinusoidal (25 deg/s) and transient stimuli of different velocities (50, 125, 300, 600, 900, and 1200 deg/s), producing a range of firing rates and corresponding degrees of synchrony, displayed in Figure 2-8F.. In general, there was a monotonic increase in thalamic synchrony with firing rate, fit well by an exponential function (Figure 2-8F, blue curve).

To more systematically explore the relationship between the measured thalamic synchrony and Criterion 1 of the thalamocortical connectivity inference, we generated a set of simulations based on experimental data to demonstrate how increasing degrees of thalamic synchrony could influence the connectivity inference. Described in more detail below, the simulations were based on introducing spiking activity that corresponds to varying degrees of synchrony into the experimentally observed spiking activity at the levels of both thalamus and cortex. As described above for experimental observations, through these simulations we also found that the synchronization of the presynaptic thalamic population could potentially produce errors in two scenarios: misses (i.e., a connected pair being incorrectly inferred as “not connected”, denoted $C \rightarrow NC$) and false alarms (i.e., a not connected pair being incorrectly inferred as ‘connected’, denoted $NC \rightarrow C$).

We first sought to simulate the scenario of the top row of Figure 2-8C where a pair of connected thalamocortical neurons (VPm Unit 1-S1 Unit 1) was misclassified as not-connected because a significant maximum peak was not detected in the central 1-4 ms lag of the raw cross-correlogram (violating Criterion 1, rightmost panel). We hypothesized that this experimental observation was due to a significant increase in cortical firing that was caused by inputs of nearby VPm neurons also connected to the same cortical neuron S1,

but relatively synchronous with the reference thalamic neuron VPm1. For this simulation, we therefore emulated this scenario by reintroducing jittered spikes from VPm Unit 1 and S1 Unit 1 back into these datasets, respectively. Importantly, we found from our experimental observations that the mean thalamic and cortical firing rate increased with stimulus strength, but cortical firing increased to a lesser extent as compared to thalamic firing (not shown). Therefore, the number of added spikes and the jitter (zero-mean Gaussian noise of a specific standard deviation, σ) were both set to produce a specified level of synchrony between the original and perturbed VPm1 spike train and also match the observed firing rates in both VPm and S1 for this particular condition. The resultant thalamic and cortical activity was denoted as VPm Unit 1* and S1 Unit 1*, respectively. A schematic of this was shown in Figure 2-9A. With these manipulations, we performed the analysis of connectivity as before between VPm Unit 1* and S1 Unit 1* at each firing rate level (with corresponding thalamic synchrony level) to generate the probability of the connectivity inference (i.e., probability of satisfying Criterion 1 reported as the fraction of bootstrapped iterations results in satisfying Criterion 1). We found that the probability of inferring a connection dropped with increasing thalamic synchrony as shown in the top of Figure 2-9B. For low levels of synchrony (e.g., thalamic synchrony measures of 0.2 or less), the probability of satisfying Criterion 1 (and thus making the correct inference, given that Criterion 2 is satisfied) remained relatively high (from ~ 0.6 to 0.9). However, increasing levels of thalamic synchrony (and certainly above 0.5), the probability of satisfying Criterion 1 approached 0 (and thus the chance of a miss neared 100%). The raw spike cross-correlogram for two synchrony levels (highlighted with the green and blue vertical dashed lines in Figure 2-9B top) are shown below, illustrating the disappearance

of the peak in the 1-4ms lag with increased synchrony. This is consistent with what we observed in the actual experimental data (Figure 2-8C, top right). Note that for artificially high levels of synchrony, approaching near perfect synchrony, the probability of satisfying Criterion 1 does gradually come back up and approach the same probability as for very low levels of synchrony, as expected (not shown for simplicity).

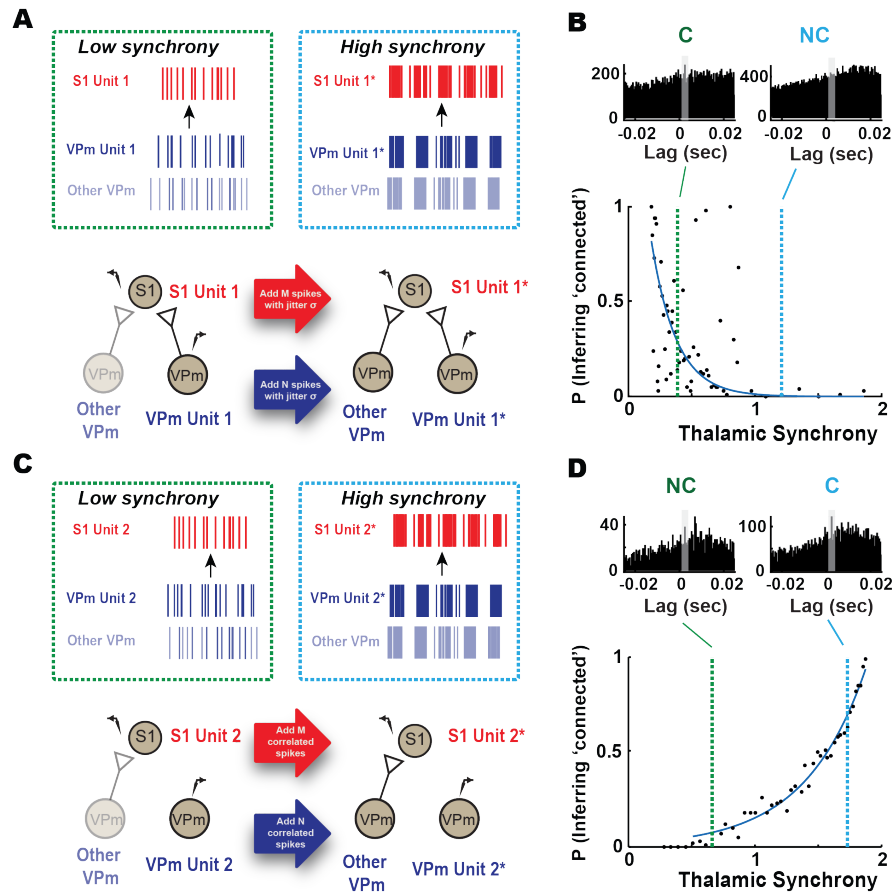


Figure 2-9. Potential errors in connectivity inference due to thalamic synchrony.

A: Schematic shows conditions for 2 different synchrony levels, low and high. As thalamic synchrony increases, both thalamic and cortical units showed an increase in firing rate accompanied by highly synchronous spiking in the local ventral posteromedial nucleus (VPm) population. To approximate this effect, we gradually added synchronous spikes in VPm and primary somatosensory cortex (S1). We matched the firing rate of thalamic (N spikes) and cortical cells (M spikes), using experimental data, and introduced the same amount of jitter (r) associated with a specific thalamic synchrony level to both spike trains. **B:** The effects of increase in synchronous firing on the monosynaptic connectivity

inference were examined with a probabilistic measure. Our simulation showed that with increasing thalamic synchrony, the probability of satisfying the criterion for monosynaptic connection decreased. Two example raw cross correlograms, corresponding to low and high synchrony level, showed that a connected (C) pair (green, $P = 0.3$ at synchrony level of 0.25) could be misclassified as not connected at a higher synchrony level (light blue, $P = 0.05$ at synchrony level of 1.2). **C:** Same as A but for an example not-connected (NC) thalamocortical pair. We gradually increased the thalamic and cortical firing by introducing synchronous spikes from a neighboring connected pair (denoted as N correlated spikes for thalamic and M correlated spikes for cortical cell). We found that the probability of error rapidly increased with thalamic synchrony (probability of satisfying criterion 1 exceeds 0.5 as thalamic synchrony reaches 1.5). **D:** The probability of incorrectly inferring connectivity significantly increased with increasing synchrony. Two example raw cross correlograms at the corresponding thalamic synchrony level showed that a not-connected pair could be misclassified as connected at a higher synchrony level. Note the emergence of monosynaptic peaks in raw cross correlograms with increased synchrony.

On the other hand, we found that in addition to causing the incorrect classification of a connected pair (i.e., a “miss”), the thalamic synchrony induced by increased stimulus drive could also have the opposite effect – the incorrect classification of a not-connected pair as connected (i.e., a “false-alarm”). When considering a thalamocortical pair that is not synaptically connected (VPm Unit 2-S1 Unit 2), increased stimulus drive introduces the presence of spiking in the S1 neuron induced by nearby VPm neurons that serve as synaptic inputs to the S1 neuron in question. When these VPm neurons become increasingly synchronous with VPm Unit 2, this results in the presence of a peak in the raw cross-correlogram in the 1-4ms bin, satisfying Criterion 1 and thus resulting in a “false alarm”, displayed in Figure 2-8D.

For a demonstration of this phenomenon, from experimentally obtained data, we conducted a simple simulation designed to systematically explore this effect. Specifically, in addition to the not-connected pair in question, VPm Unit 2-S1 Unit 2, we identified a distinct, simultaneously recorded thalamocortical pair that was inferred to be connected. By introducing spikes from the connected thalamic and cortical neuron into the spike trains

of VPm Unit 2 and S1 Unit 2, respectively, the degree of thalamic synchrony was systematically increased as a function of the number of spikes added, but at the same time introduced the presence of cortical spiking from the connected pair. As with the first simulation, the number of spikes added to VPm Unit 2 and S1 Unit 2 was set to match the observed thalamic and cortical firing rates for this condition, to produce the perturbed spikes trains VPm Unit 2* and S1 Unit 2*. A schematic of this was shown in Figure 2-9C. With these manipulations, we performed the analysis of connectivity as before, but now between VPm Unit 2* and S1 Unit 2* at each firing level (with corresponding thalamic synchrony level) to generate the probability of the connectivity inference (i.e., probability of satisfying Criterion 1 reported as the fraction of bootstrapped iterations results in satisfying Criterion 1), as with the first simulation. We found that as thalamic firing became more similar with increasing amount of mixing (reflected in an increase in thalamic synchrony), the raw cross-correlogram exhibited the increased likelihood of a peak in the 1-4ms bin. Correspondingly, the probability of error rapidly increased with thalamic synchrony (probability of satisfying Criterion 1 exceeds 0.5 as thalamic synchrony reaches 1.5 in the top panel of Figure 2-9D). The raw spike cross-correlogram for two synchrony levels (highlighted with the green and blue vertical dashed lines in Figure 2-9B right top), illustrated the appearance of the peak in the 1-4ms lag with increased synchrony (Figure 2-9D bottom right). Although these simulations should be considered primarily in terms of the basic trends they exhibit, the rapid increase in the probability of error with thalamic synchrony suggests that above some level of synchrony in the pre-synaptic population, false-alarms are inevitable.

2.4 Discussion

The field of neuroscience is in a period of rapid tool development, spawned by a combination of innovative technologies and a shift in the focus of international scientific priorities. The explosion of tools for performing large scale neuronal recording at single cell resolution provides access to real-time monitoring of network activity within and across multiple brain regions (Ahrens et al. 2013; Chung et al. 2019; Jun et al. 2017). This access enables the exciting potential for interpretation of the causal flow of neuronal activity that ultimately underlies brain function, shaping of perception, and behavior (Sheikhattar et al. 2018). There have been significant efforts in anatomical tracing of connectivity and cell-type specific projections within and across brain regions and hemispheres, leading to new insights into the detailed structure of brain circuits (Yuan et al. 2015). The ultimate goal is to understand how this complex structure gives rise to behaviorally relevant function through the dynamic interaction of neurons within the neural network. However, the identification of functional connections amidst perturbation-induced confounding variables in an intact brain remains very challenging despite increasing accessibility (Lepperød et al. 2018). Here, we provided an experimental and analytical framework for quantifying long-range synaptic connectivity that was developed and tested in the thalamocortical circuit of the rodent somatosensory pathway but is generalizable to other circuits and pathways. Importantly, we attacked this from a scalable statistical framework based on signal detection theory, where we established approaches to assess confidence in classification, and systematically examined factors contributing to the inference of connectivity.

The gold standard of studying and assessing synaptic connectivity involves direct manipulation of pre-synaptic neurons to observe a measurable postsynaptic effect. Hence, connectivity studies are often performed using in-vitro brain slices (Jiang et al. 2015; Pfeffer et al. 2013) due to better accessibility to pre- and postsynaptic neurons concurrently, which is difficult or intractable in-vivo (Jouhanneau et al. 2015; Jouhanneau et al. 2018; Pala and Petersen 2015). In attempts to identify connectivity in-vivo, previous studies have used electrical stimulation to conduct collision tests that involve comparing the timing of anti-dromic activation with stimulus evoked activity to verify origins of projection (Kathleen Kelly 2001; Swadlow 1989). Although this is a powerful and attractive approach, as it helps to more confidently assess connectivity and establish causal relationships, it does not scale well to assessing connectivity at the population level, where selective stimulation of individual neurons is not typically possible. As an alternative, we adopted non-synchronizing, weak sensory drive (Bruno and Sakmann 2006; Wang et al. 2010) to assess likely connectivity through spike cross-correlation analysis. Although this approach obviously does not address issues of causality directly, it scales with increasing size of population recordings in the pre- and post-synaptic regions, opening up the possibility for assessing connectivity using large, ensemble recordings (Juavinett et al. 2018).

The systematic evaluation of the parameters of analysis presented here offers the potential for the optimization of experiment design for the purpose of assessing connectivity. Although the details likely vary across brain region and experimental preparation, the results here do suggest some general rules of thumb, perhaps the most important of which revolve around the interplay between data-length and synchrony. For

example, based on our data, we estimated that about ~9000 spikes (in terms of geometric means of total thalamic and cortical spikes) were needed to reach an inference with high certainty (95% confidence interval) in the fentanyl-anesthetized rat, consistent with recommended number of spikes used using similar stimulus conditions (Bruno and Simons 2002; Wang et al. 2010) and between 6800 and 10,000 spikes for spontaneous and sinusoidal conditions respectively in the isoflurane-anesthetized mouse (overall data shown in Figure 2-10). Thus, the requirements were on the same order of magnitude for both of these cases, despite significant differences in experimental preparation (i.e., anesthesia, etc.) and differences in precise anatomical details across the species.

Synchrony across the pre-synaptic population has long been implicated as a potential confound in assessing synaptic connectivity, typically tied to false alarms (type 1 error), or the incorrect inference of connectivity in non-connected pairs (Ostojic et al. 2009). The results here supported this long-held assumption, where the artificially elevated synchrony in the VPM population resulted in the increased likelihood of satisfying Criterion 1, and importantly established ranges of measured synchrony for which this is more likely. Surprisingly, we also found that increased pre-synaptic synchrony could result in a different type of confound – a miss (type 2 error), or the incorrect inference of not-connected for connected pairs. Interestingly, this effect emerged over a relatively similar level of synchrony as determined through artificial elevation of the thalamic synchrony. As expected, spontaneous activity is typically fairly asynchronous, and in this regime, the types of errors described here are unlikely for this case. However, common drive through sensory input designed to elevate firing in otherwise sparse conditions increases the likelihood of these errors, and thus the tradeoff between increased data length and

synchronization plays an important role in experimental design. This is further important in extending this approach to awake, behaving conditions, with increased firing rates, and continuous modulation in population synchrony by brain state. One alternate explanation for increased likelihood of synaptic connectivity classification errors as we moved from stimulus-free condition to highly synchronizing, transient stimuli could be due a higher rate of spike sorting errors, where elevated firing across all units (single-unit and multi-unit) could cause waveform distortion and hence cluster misclassification. Despite a slight reduction in waveform signal-to-noise ratio (4% change for VPm and 1.5% change for S1), however, we found no significant difference when we compared the waveform features of all single units such as peak-to-peak amplitudes and signal-to-noise ratios in spontaneous and stimulus-present conditions (see Figure 2-11, mice data).

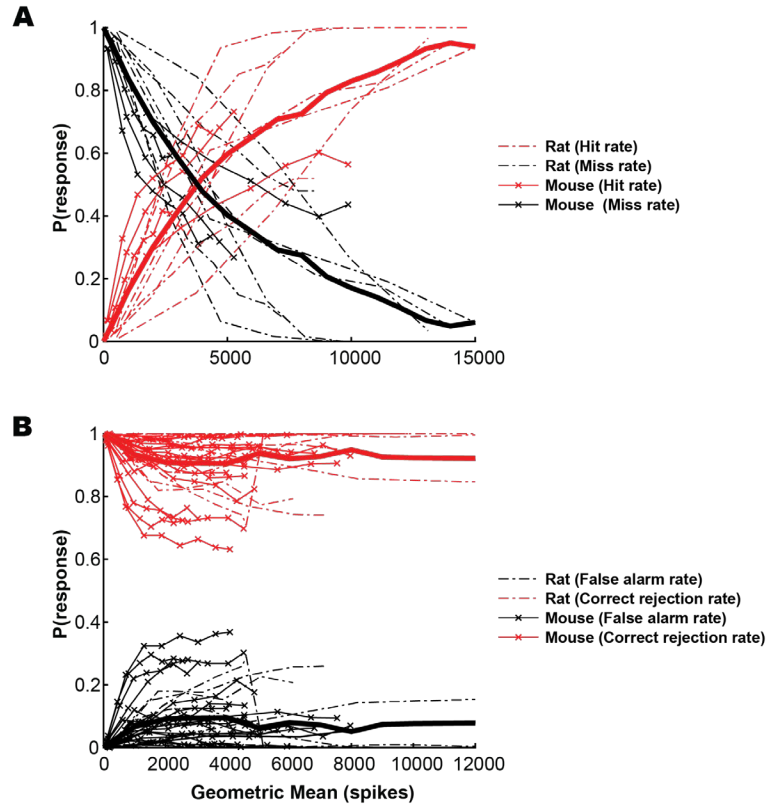


Figure 2-10. Effect of data-length on monosynaptic connectivity inference for rat and mouse data.

A. Hit and miss rates for all connected pairs ($n = 11$ pairs). **B.** Correct Reject and False Alarm rate for all not-connected pairs ($n = 31$ pairs). Note that the hit rate and correct reject rate are similar to $P(\text{correct inference})$ on other figures (related to Figure 2-7). Bold lines represent mean probabilities, averaged across pairs at each data-length (if available).

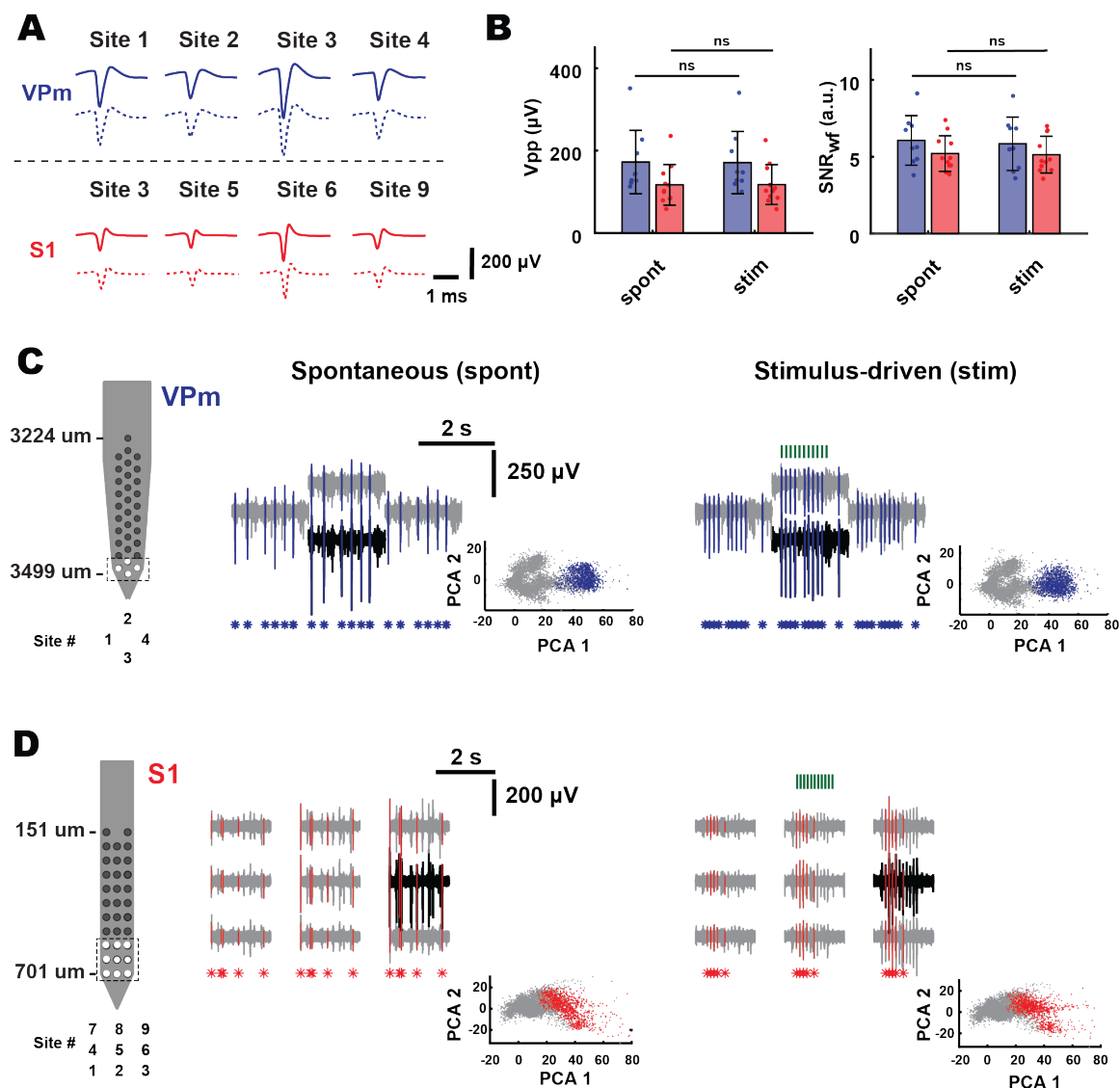


Figure 2-11. Single-unit isolation quality of probe recordings during spontaneous and stimulus-driven conditions.

A. Example mean single-unit waveforms in C and D for spontaneous (top, solid-filled) and stimulus-driven (bottom, dashed-filled) conditions. **B.** Peak-to-peak amplitude and unit quality of waveform across spontaneous and stimulus-driven condition. (Spontaneous (Vpp): VPM = $172 \pm 76.7 \mu$ V, $n = 9$ neurons, S1 = $117 \pm 49.3 \mu$ V, $n = 11$ neurons; Stimulus-driven: VPM = $171 \pm 75.2 \mu$ V, $n = 7$ neurons, S1 = $118 \pm 48.2 \mu$ V, $n = 11$ neurons; Spontaneous (SNR_{wf}): VPM = 6.06 ± 1.62 arbitrary unit (a.u.), $n = 9$ neurons, S1 = 5.21 ± 1.16 a.u., $n = 11$ neurons; Stimulus-driven: VPM = 5.84 ± 1.74 a.u., $n = 9$ neurons, S1 = 5.13 ± 1.19 a.u., $n = 11$ neurons, $N = 1$ mouse) **C.** Electrode configuration shown on the left. Sample voltage trace from VPM single unit with detected spikes (highlighted in blue) for spontaneous and stimulus-driven conditions. Inset (bottom): Waveform feature scatterplot showing spike clusters of the example unit and noise (gray, spikes from other whisker-responsive units detected on the same or neighboring channels). **D.** Same as (C)

but for S1 single unit. PCA 1 and PCA 2 plotted here are the two largest principal components of the example unit and other spikes are projected onto these dimensions.

Although the approach here was developed with generality in mind, there are several potential limitations related to the specific details of the experimental preparation. First, the data collected in this study were from immobilized, anesthetized rodents. This enabled relatively stable and long-duration recordings of well-controlled stimulus conditions that provided insights for accurate identification of synaptic connectivity across different stimulus regimes. Although we envision the broad applicability of this approach for awake, paired recordings, future experiments are required to pinpoint the optimal experimental conditions for monosynaptic connectivity inference in awake rodents. Specifically, the relationship between mean firing rate and thalamic synchrony must be determined in this context. It was known that the baseline firing rate for both thalamic and cortical neurons are higher under wakefulness (Crochet and Petersen 2006; Urbain et al. 2015), however it is unclear if thalamic synchrony also increases monotonically with mean firing rate. Additionally, the effect of whisking is likely to confound the relationship between stimulus strength and measured synchrony explored in this study, hence confounding the monosynaptic connectivity inference. However, given the techniques and experimental parameters explored in this study, we believe that this has laid the foundation for capturing connectivity during wakefulness. Ideally, a non-synchronizing stimulus (sensory or optical) should be used to elevate the mean firing rate across the aligned thalamocortical brain regions while whisker videography should be in place to record whisker movement. Given that the effects of whisking on thalamic synchrony are unclear and could increase trial-to-trial variability, epochs of whisking should likely be excluded from the analysis for monosynaptic connectivity inference.

Second, the thalamocortical circuit is built on anatomy that is well-studied, and highly convergent, with approximately 50-100 thalamic relay neurons making synapses onto a cortical layer 4 neuron with a clear topography (Bruno and Sakmann 2006). This convergent nature of the thalamocortical projections provides significant support in assessing possible connectivity, in contrast to potential connectivity across cortical laminae or other less topographically organized projections. Third, the VPM relay neurons are reported to be uniformly excitatory, thus the pre-synaptic spiking enhances the likelihood of action potentials in the post-synaptic cortical target. Although long-range projections typically tend to be excitatory rather than inhibitory, analogous approaches should certainly be developed for inhibitory connectivity that is becoming increasingly acknowledged to play a complex and pivotal role in controlling network dynamics (Isaacson and Scanziani 2011).

With the scaling up of electrophysiological recordings comes challenges. In this work, we performed highly curated, small scale electrophysiological recordings to evaluate dynamics of VPM (potential pre-synaptic) and S1 (potential post-synaptic) neurons on a pair-by-pair basis as well as large-scale pre- and post-synaptic recordings, where any pair of neurons from the upstream and downstream structures would be a candidate for connectivity inference. What comes hand-in-hand with increasing recording yield that enables us to better answer questions about circuit function is an increasing diversity of recording quality, increasing diversity of cell type, and a wide array of possibilities for connectivity. In our hands, we found that the odds of finding putative monosynaptic connections per recording session increased by at least two- to three-fold, as illustrated in Figure 2-6, where 5-10 single units can be isolated from each brain region for the

connectivity inference. Previous studies suggest that high signal quality can be obtained with multi-site recording due to its better detectability of extracellular feature across closely spaced contacts (Buzsáki 2004; Gray et al. 1995; Harris et al. 2000). Hence, this increase in recording yield as well as the increased probability of detecting monosynaptic connectivity with high-density probe recordings were likely due to improved single unit isolation over time, enabling reliable tracking of single units over longer recording duration (3-4 hours). Yet, in practice, handling large amounts of data with probe recordings presents challenges as most of the spike sorting algorithms to-date require manual curation to improve spike classification. This suggest that a certain amount of contamination of spikes from neighboring cells is to be expected. Overall, large-scale recording of neuronal activity will reduce the number of animals, reveal important information only available from monitoring the interaction of brain networks, but the variability inherent in these datasets drives the need for a more comprehensive approach for diverse neuronal ensembles. Traditionally, cross-correlation analysis of homogeneous, highly curated, small scale electrophysiological recordings was primarily used to attach a binary outcome for concluding monosynaptic connection in-vivo (Bruno and Simons 2002; Fujisawa et al. 2008; Miller et al. 2001; Reid and Alonso 1995; Swadlow 2003; Swadlow and Gusev 2001) and data with uncertainties were often discarded. In this work, the evaluation of the neuronal data would not result in a binary classification of connected or not, but instead the assignment of a likelihood of connectivity based on the statistical framework we present here, producing a probabilistic connectivity map. While this approach was developed through analysis of extracellular neuronal spiking data, we also envision that this would be readily adapted to optical imaging approaches that enable cellular resolution calcium or

voltage imaging of population spiking activity. Recently, model-based approaches to improve connectivity estimation are being developed for the analysis of large datasets (Chen et al. 2011; Kobayashi and Kitano 2013; Kobayashi et al. 2019; Lütcke et al. 2013; Okatan et al. 2005; Paninski et al. 2004; Stevenson et al. 2008; Zaytsev et al. 2015). These methods typically involve fitting neuronal data or correlational relationships from recordings through models (i.e., generalized linear models (GLMs)) and further aim to reconstruct neuronal circuitry to estimate functional connectivity or to decode causal flow. The statistical approach we present here could eventually be combined with these more structured network modelling approaches to provide a more comprehensive framework for assessing and understanding causal interactions in the brain.

CHAPTER 3. MULTIPLE TIMESCALES OF RAPID SENSORY ADAPTATION IN THE THALAMOCORTICAL CIRCUIT

Sensory processing requires reliable transmission of sensory information across multiple brain regions, from peripheral sensors, through sub-cortical structures, to sensory cortex, ultimately producing the sensory representations that drive perception and behavior. Numerous studies have shown that our perception of the sensory world is far from static, but instead is strongly shaped by the properties of the sensory inputs through various forms of adaptation, across a range of timescales from seconds to minutes. The neural mechanisms underlying these adaptations are still not well understood. When the brain is presented with persistent stimuli, neurons adapt their spiking responses accordingly through a modulation in sensitivity to sensory inputs. This phenomenon has been most well-studied over very rapid timescales of hundreds of milliseconds, yet other studies suggest longer time scales of 10's of seconds are also relevant for sensory adaptation. Here we investigate the effects of persistent stimulation across these timescales, as the sensory representations are transformed across brain structures in the early sensory pathway. Specifically, we take advantage of the well-known anatomical and functional organization of the rodent whisker pathway to perform *in vivo* anesthetized, simultaneous multi-electrode recordings from the ventroposteromedial nucleus of the thalamus (VPm) and layer 4 of the primary somatosensory cortex (S1) to measure the effect of prolonged exposure to persistent stimuli on thalamic neurons and their downstream cortical targets. We presented punctate whisker deflection trains to individual whiskers and quantified the adaptive effects on VPm and S1 as a function of stimulus duration. Our results demonstrate

that the degree of neuronal adaptation in both the thalamus and cortex increases with stimulus duration, and importantly, neurons adapt well beyond a single, short timescale that is typically described in the literature. We found that putative excitatory neurons (RSUs) in S1 layer 4 were more profoundly adapted than putative inhibitory neurons (FSUs), and cortical neurons, in general, adapt to a greater extent than thalamic neurons. These differential adaptation dynamics are conserved across timescales. Furthermore, an ideal observer analysis of cortical activity shows that prolonged exposure to persistent stimulation further improved discrimination performance between different velocities of whisker stimulation at the expense of detectability, pointing to additional adaptive changes beyond a single timescale. Compared to VPM, adaptation was on average more variable across neurons in S1, likely due to the complex integration of feedforward thalamic input, depression of thalamocortical (TC) synapses, and intracortical synaptic signaling across S1. We found that synchronization of thalamic spiking across the local population was further reduced with persistent sensory stimulation. Analysis of putatively monosynaptically connected thalamocortical pairs reveals a monotonic reduction in synaptic efficacy over the entire time course of the repetitive stimulation, although a more drastic decrease during the initial phase. Taken together, these results suggest that adaptation of the thalamocortical circuit across timescales results from a complex interaction between distinct mechanisms and the engagement of different mechanisms can shift depending on the timescale of environmental changes.

3.1 Introduction

Natural sensory stimuli in our daily lives encompass a great diversity of statistics at many spatial and temporal scales. It has long been asserted that the brain's ability to adjust its sensitivity to a wide range of stimulus statistics is a fundamental function that is critical for survival (Barlow 1961). This phenomenon, broadly referred to as sensory adaptation, is a ubiquitous feature in the brain that is well-documented across all sensory modalities in a wide variety of organisms (Whitmire and Stanley 2016). It has been posited that all sensory systems have adaptive properties to overcome changes in stimulus statistics mediated through multiple mechanisms of adaptation that modulate their response properties over a variety of timescales ranging from milliseconds to evolutionary spans (Latimer et al. 2019). While adaptation across mechanisms and timescales has been proposed as a unifying theoretical framework that may integrate numerous disparate experimental observations (Drew and Abbott 2006), the large majority of studies of sensory adaptation focus on a single timescale (Chung et al. 2002; Khatri et al. 2004; Kheradpezhrouh et al. 2017; Patterson et al. 2013), likely targeting one specific mechanism. What is not well understood is the interaction between the mechanisms of adaptation across different timescales that would be relevant in ethological contexts.

As sensory signals move from the periphery to sensory cortex, sensory representations are progressively transformed via the specific characteristics of the circuitry at each stage and the nature of the anatomical projections from region to region (for a review, see Adibi and Lampl, 2021). In the rodent whisker-mediated somatosensory pathway, previous studies have shown that the degree of sensory adaptation increases as

neural signals traverse from periphery to cortex (Khatri et al., 2004; Ganmor et al., 2010, Mohar et al., 2013, 2015). A particularly important stage of the sensory signaling pathway is the thalamocortical circuit, where complexity explodes as highly divergent thalamic afferents synapse on to both excitatory and inhibitory neurons in the cortex, initiating thalamic-driven feedforward inhibition that has profound effects on sensory representations (Cruikshank et al. 2007a; Cruikshank et al. 2007b; Gabernet et al. 2005b; Simons and Carvell 1989; Wang et al. 2010). This sequence of excitation followed by inhibition has been shown to be critical for maintaining a precisely time-locked response in excitatory principal cells (Gabernet et al. 2005b). Additionally, differential adaptation of thalamic neurons and cortical excitatory and inhibitory neurons has been shown to be important for tuning the cortical circuit to optimally represent whisker velocity and direction selectivity of whisker deflection in the rodent pathway (Khatri et al. 2004; Simons and Carvell 1989; Wilent and Contreras 2005). Given the complexity of the thalamocortical circuit, it is likely that multiple mechanisms are engaged in the transformation of sensory representations along the pathway. Short-term depression of thalamocortical synapses has been intensely investigated, and likely plays a prominent role in sensory adaptation (Castro-Alamancos 2004b; Chung et al. 2002; Katz et al. 2006). However, recent work also suggests that adaptive changes in thalamic spiking synchrony, in addition to robust engagement of feedforward cortical inhibition, also play an important role in mediating rapid adaptation in mouse barrel cortex (Wang et al. 2010; Wright et al. 2021a). Our goal was to find commonalities in these mechanisms across different timescales and determine the functional relationship to each other.

Here, we investigated the time course of adaptation across a range of timescales exhibiting multi-exponential signatures suggestive of multiple underlying mechanisms. Specifically, we utilized multi-site, multi-electrode extracellular recording of spiking activity from the ventro-posteromedial (VPm) nucleus of the thalamus and layer 4 of the whisker response region of primary somatosensory cortex (S1) in the anesthetized mouse. To investigate adaptation across timescales, we presented repetitive, punctate whisker deflection trains to individual whiskers and quantified the adaptive effects on single-unit spiking activity in VPm and putative excitatory and inhibitory neurons in S1 as a function of stimulus duration. We uncovered evidence of at least two timescales in the adaptation dynamics that exhibited differential functional properties across the thalamocortical circuit, affecting both the response magnitude and spike timing latency. We found thalamic synchrony plays a more prominent role in the second, longer timescale, whereas short-term synaptic depression, as measured through identified monosynaptically connected pairs, contributes more in the first, short timescale, although both mechanisms seemed to have some influence across the entire range of timescales studied. Notably, from the perspective of an ideal observer of spiking activity, we found that adaptation across multiple timescales also shifts towards better discrimination of whisker deflection velocity at the expense of detection. Taken together, the results here suggest that the overlap of distinct mechanisms can underlie adaptive dynamics across timescales and although multiple mechanisms may interact or switch dynamically at various timescales, the similarity in function supports the possibility of a unifying framework across disparate mechanisms and timescales.

3.2 Methods

3.2.1 *Animals*

Experiments were conducted using adult C57BL/6J, Ai32xNR133 (Bolus et al., 2020; Ai32 crossed with the NR133 Cre-recombinase driver line; Gerfen et al., 2013), and Ai32xPV-Cre mice (older than 2 months) of both sexes. All procedures were approved by the Georgia Institute of Technology Institutional Animal Care and Use Committee and followed guidelines established by the National Institutes of Health.

3.2.2 *Experimental Procedures*

3.2.2.1 Head-plate implantation

Head-plate implantation and intrinsic imaging procedures were usually performed at least three days to one week before acute experiments. A lightweight custom metal (titanium or stainless steel) head-plate was implanted on the skull of the mouse for head fixation and improved stability during recording, in accordance with a previously described protocol (Borden et al. 2017; Liew et al. 2021; Wright et al. 2021a). During this survival surgical preparation, the animal was sedated with 5% vaporized isoflurane and anesthesia was maintained with 2-3% isoflurane for the head-plate procedure. We administered opioid and non-steroidal anti-inflammatory analgesic (SR-Buprenorphine 0.8 - 1 mg/kg, SC, pre-operatively, and Ketoprofen 5-10 mg/kg, IP, post-operatively) and covered the animal's eyes with ophthalmic eye ointment (Puralube Vet Ointment). Body temperature was monitored and maintained at 37 °C. After sterilizing the skin above the skull and applying topical anesthetic (lidocaine 2%, 0.05 ml, max 7mg/kg, SC), we removed the skin and

scraped off periosteum and any conjunctive tissue from the skull. We gently separated tissue and muscles close to the lateral edge of the skull using a scalpel blade (Glass Van & Technocut, size no. 15), leaving sufficient room for head-plate attachment and away from targeted recording areas. To ensure that the skull surface remained level during head fixation, we adjusted the animal's head position to minimize the relative height difference ($< 100 \text{ } \mu\text{m}$) between the skull surface at the bregma and lambda landmarks (Franklin and Paxinos 2008). We found this step to be critical especially for VPm targeting. We secured the metal headplate over the intact skull with C&B-Metabond (Parkell Prod Inc). The Metabond dental acrylic was chilled using ice, slowly applied to the skull surface, and allowed to cure for 5-10 minutes before we covered the rest of the attachment site and edges of the skin incision with skin adhesive (Vetbond, 3M) to ensure that the skin edges were securely adhered to the skull. The final head-plate and dental acrylic structure created a recording well for holding Ringer's solution (in mM: 135 NaCl, 5 KCl, 5 HEPES, 1 MgCl₂-6H₂O, 1.8 CaCl₂-2H₂O, pH 7.3) for future imaging and electrophysiological recording sessions. We applied a thin layer of transparent Metabond dental acrylic over both hemispheres to prevent inflammation and covered the exposed skull with a silicone elastomer (Kwik-Cast, World Precision Instruments) if there were no other additional procedures after head-plate implantation.

3.2.2.2 Intrinsic Optical Imaging in the Mouse S1 Barrel Cortex

We performed intrinsic signal optical imaging of whisker-evoked responses in mouse primary somatosensory cortex under 1-1.2% isoflurane anesthesia to functionally identify barrel columns (Lefort et al. 2009; Pala and Petersen 2015). All whiskers except

the whiskers of interest (A2, B1, C2, D1, D3 and E2) were trimmed. The skull was thinned using a dental drill (0.1 mm diameter bit, Komet, USA) until blood vessels became visible. Warm Ringer's solution was applied on top of the skull and covered with a glass coverslip (thickness 0.13-0.17mm, Fisherbrand). A reference image of the blood vasculature was captured under green illumination (530nm) (M530F1 LED, Thorlabs). Repetitive whisker stimuli (10 Hz, sawtooth pulses, 1000 deg/s) were delivered to individual whiskers using a galvanometer system (Cambridge Technologies) while performing imaging of barrel cortex under red illumination (625 nm) (M625F1 LED, Thorlabs) – see Whisker Stimulation section below. Images were acquired using a CCD Camera (MiCam02HR, SciMedia) at 10 Hz, with a field of view of approximately 4 x 2.5 mm, corresponding to 384 x 256 pixels (resolution: 100pixel/mm). Each trial lasted 10s, with 4s of baseline followed by 4s of whisker stimulation and 2s without stimulation. The inter-trial interval was 30s. Whisker-evoked responses were averaged over 10-20 trials. Intrinsic signals were measured as the relative change in reflectance by taking the overall mean reflectance during whisker stimulation (R_{stim}) and subtracted the mean baseline reflectance ($R_{stim} - R_{baseline}$). Acquisition and processing of the images were implemented using “BV_Ana” software (MiCam02HR, SciMedia, Ltd) and Matlab (MathWorks, Natick, 2015). We recorded intrinsic signals from at least three barrels and estimated the location of the unmapped barrels by overlaying a template barrel map reconstructed from histology. At the end of the imaging session, we applied transparent Metabond dental acrylic directly on the S1 site to protect the thinned skull from contamination and infection and sealed the exposed skull with a silicone elastomer (Kwik-Cast, World Precision Instruments).

3.2.2.3 Surgery and craniotomies

On the day of recording, the head of the mouse was held in place with a head-post clamp to ensure that the animal would remain in the flat skull position. We covered the eyes with ophthalmic eye ointment (Puralube Vet Ointment) to prevent dehydration. The animal was then anesthetized using 2-3% isoflurane. Before performing the craniotomies, we thinned the skull above VPm and S1 carefully with a dental drill (0.1 mm diameter bit, Komet, USA) and irrigated the skull surface with Ringer's solution frequently to remove debris and prevent overheating. When the skull was thin enough to easily puncture, we made two small craniotomies above VPm (approximately 0.5 mm diameter; centered at 1.8 mm caudal and 1.8 mm lateral to bregma) and S1 (approximately 0.3-0.5 mm diameter, using the intrinsic imaging signal and the blood vasculature as a landmark). Each craniotomy was made by first penetrating the thinned skull using an insulin syringe needle tip (at approximately a 40–50-degree angle) to make numerous small holes outlining the edges of the craniotomies until the skull piece was loosely attached. The less perforated region of the circular skull piece was used as a pivot, and we levered the skull pieces off from the more perforated edge using fine-tip forceps (FST Dumont #5SF) to expose the brain surface. The craniotomies were constantly irrigated with Ringer's solution to maintain the integrity of brain tissue.

3.2.3 *Anesthetized electrophysiology*

3.2.3.1 Neuronal recordings.

Multielectrode silicon probes with 32-channel 'Poly-3' (A1x32-Poly3-5mm-25s-177, A1x32-Poly3-6mm-50s-177, or A1x32-Poly3-10mm-50s-177) were independently

lowered into the thalamus and cortex. To improve signal quality, we electroplated the silicon probes with the polymer PEDOT:PSS (Baião 2014) with a nanoZ device (Multi Channel Systems, Germany). The impedances of the contact sites were measured prior to each recording and ranged from 0.3-0.8 MOhms. Data were collected using a 64-channel electrophysiological data-acquisition system (TDT Model, etc. RZ2 Bioprocessor). Neuronal signals were amplified, and bandpass filtered (500Hz-5kHz) and digitized at ~25kHz per channel. Stimulus waveform and other continuous data were digitized at 10kHz per channel. Simultaneously, the local field potential (LFP) signals were obtained after bandpass filtering (0.5-200Hz). The LFPs were used to identify the primary whisker response (see Whisker Stimulation). For VPM recordings, the electrode was typically positioned 1.8 mm caudal and 1.8 mm lateral to bregma and lowered to a depth of ~ 3 – 3.5 mm. If VPM could not be functionally located using this method, the relative distance from the location of the barrel cortex (usually measured 1.0-1.2mm from the B1 or Beta barrel column to find whisker responsive thalamic regions) was used. For S1 recordings, a small craniotomy (diameter ~0.5 mm) was created at the desired location above the barrel cortex based on the intrinsic imaging signal, being careful to remain distant from blood vessels. The electrode was positioned at a 35 ° angle from the vertical axis (parallel to the barrel column) and cortical neurons were recorded at a stereotaxic depth of 300-600um from the cortical surface. After the first recording session, the probe(s) were removed, exposed tissue was covered with agarose, and the well was sealed with Kwik-Cast. Two or three recording sessions (one per day) were obtained from each mouse using the original craniotomy or from an additional craniotomy, but a different cortical column and barreloid was targeted each time.

3.2.4 *Sensory Stimulus*

3.2.4.1 *Transient stimulus*

To identify the single whisker of interest, all whiskers on the face were manually deflected while the extracellular signal was monitored. Once units were isolated by moving the electrode as close as possible to the responsive cells that primarily responded to a single whisker, controlled, single whisker stimulation was delivered in the rostral-caudal plane using a computer-controlled galvo-motor (galvanometer optical scanner model 6210H, Cambridge Technology). Whiskers were trimmed ~12 mm from the face. The primary whisker (PW) was defined as the whisker whose deflection evoked the maximal neuronal response with the shortest latency. The primary whisker was fed into the insertion hole at the end of an extension tube (inner diameter: ~200-300 μm , length: 15mm) that was connected to the rotor of the galvanometer stimulator. The stimulus probe was positioned at 10 mm from the vibrissal pad. The range of motion of the galvanometer was $\pm 20^\circ$, with a bandwidth of 200Hz. The galvanometer system was controlled using a custom developed hardware/software system (Matlab Real-Time Simulink System, MathWorks or the Real-time experiment Interface application (<http://rtxi.org/>)), with 1 kHz sampling rate. Sawtooth stimuli were delivered (exponential rise and decay waveforms lasting 17ms, with reported velocity defined by the average over the 8.5-ms rising phase; Wang et al., 2010) in the rostral-caudal direction either in isolation, or as part of a 10 Hz, adapting stimulus train with variable duration (1.5, 10-seconds). The stimuli typically consisted of a train of adapting stimuli (10 Hz frequency, 10s in duration, with either 300 deg/s or 800 deg/s

velocities) followed by an isolated test pulse (similar or different velocities) after some time interval after the adapting stimuli.

To probe the adaptation profile of neurons of interest across timescales, stimuli were designed to investigate the adaptation dynamics for two distinct durations of exposure (1.5 and 10-seconds) of adapting stimuli. For the control condition, the response of the first pulse in the adapting train for all three stimulus durations was compared. To probe the post-adaptation effect of variable duration of exposure to repetitive stimulation, the velocity tuning curves (isolated pulse delivered at variable velocities: 50, 125, 300, 600, 800, 900, 1200 deg/s) were measured under three different conditions (“control” condition with no adapting train, and “adapted” condition with either 1.5-s stimulus or 10-s stimulus). Isolated pulses were delivered immediately following the 10 Hz adapting train. All stimulus conditions were randomized across trials, and at least 20 trials per stimulus condition were typically obtained for different recovery periods and velocities. To examine the adaptation profile of each cell across timescales, each cell’s response to the 10-sec stimulus was analyzed. However, a subset of trials (20 trials at the minimum) was used to assess the recovery profile and velocity tuning properties.

For the 32-channel probe recording in thalamus, the LFP response was quantified in a 30 ms post-stimulus window for each channel to identify principal whiskers (PW). Well-isolated single units that showed whisker responsiveness were verified by calculating the LFP peak amplitude and peak latency in response to stimulation of different whiskers. A neuronal pair was verified to be topographically aligned when (1) they shared maximum response (SUs max FR and LFP amplitude) to the same primary whisker under punctate

stimulation, and (2) the latency difference of the whisker response was between 1-5 ms (LFP peak latency and SU mean FSL, or SU mean peak latency).

3.2.4.2 Weak sinusoidal stimulus

For the assessment of potential monosynaptic connectivity between thalamic and cortical neurons, the thalamocortical circuit was probed using a weak, desynchronizing sinusoidal whisker stimulus to elevate baseline firing rates in recorded units, as previously described (Liew et al. 2021). 4°, 2-4Hz weak sinusoidal deflections (Bruno and Sakmann 2006; Bruno and Simons 2002; Wang et al. 2010) were delivered for approximately 200-500 trials to obtain at least 2000 spikes for the cross-correlation analysis. Each trial consisted of 4-sec sinusoidal inputs and a 2-sec intertrial stimulus interval. Occasionally, the first 0.5-1 s of the trials were eliminated due to high firing rate at the onset of stimulus presentation.

3.2.5 *Optogenetic Stimulation of Neural Activity*

In a subset of experiments, experiments were performed on eight Ai32xNR133 transgenic mice to directly stimulate VPM neurons, bypassing sensory activation from the periphery. In these experiments, a 32-channel silicon optoelectrode was used (A1x32-Poly3-5 mm-25s-177-OA32LP, with attached 105 μ m optic fiber coupled to a 200- μ m optic fiber, Thorlabs). Optic fibers were coupled to a 470 nm LED (M470F3, Thorlabs). The sensory stimulus protocol as described above was presented, in addition to a set of “LED” trials in which a 10 Hz, 10-sec pulsatile input of 470nm light was delivered to VPM cell bodies (similar duration with sensory sawtooth stimuli), followed by probe stimuli of variable velocities: 50, 125, 300, 600, 800, 900, 1200 deg/s). Four randomly interleaved

conditions were utilized: (1) Control – no repetitive stimulation with probe stimulus, (2) 1.5-sec, 10 Hz adapting train, (3) 10-sec, 10 Hz adapting train, (4) 10-sec, 10 Hz LED pulses, all followed by probe stimuli to measure velocity tuning curves. Each condition was repeated for 20-30 trials.

3.2.6 Post-mortem histology

To verify recording sites and the angle of penetration that was optimal for locating VPM and S1, a small subset of animals was perfused after the paired recording experiment. To label each electrode recording track, the electrode was slowly retracted along its axis of entry at the conclusion of recording and a few drops of DiI (2.5mg/mL, in ethanol) was applied. The electrode was then inserted into the same penetration site, back along the same axis, and the electrode was left in the brain for at least 15 minutes. Following the end of the experiment, the animal was euthanized with an overdose of sodium pentobarbital (euthasol, 0.5 mL at 390mg/mL for rat, 0.1 mL at 390 mg/mL), a transcardial perfusion was performed, the brain was extracted, and the brain was fixed in 4% paraformaldehyde (PFA, Electron Microscopy Sciences) overnight. The brain was sliced in 100 um coronal sections and cytochrome oxidase staining was performed to reveal VPM (barreloid) and S1 (barrel). As an additional verification of the recording site, the overlap between the DiI stained recording track and the CO-stained regions was identified.

3.2.7 Analytical Methods

3.2.7.1 Spike sorting

In assessing potential synaptic connectivity using cross-correlation analysis, the clear isolation of single unit activity from extracellularly recorded voltage signals is critical. In all of our experiments, we performed extracellular single-unit recordings using either one or two 32-channel NeuroNexus probes, and performed spike sorting offline using the KiloSort software package (Harris et al. 2000). Well-isolated single units were classified using the following criteria: (1) Waveform signal-to-noise (SNR) ratio > 3, (2) ISI violation less than 1% for cortical units, and (3) ISI violation less than 2% for thalamic units.

3.2.7.2 VPm unit verification

It is important to take great care to distinguish different thalamic nuclei from one another, and particularly so in the mouse, where the regions are very small and very close together. After recording, a combination of measures was used to classify thalamic units as originating from VPm: (1) Average first-spike latency to punctate (non-adapting) stimuli, quantifying the average time between stimulus onset and the first spike fired during the neural response window (30 ms after stimulus onset) (Storchi et al. 2012). (2) Shift in average first-spike latency response to adapting stimuli, defined as the time difference between the average response to the first adapting stimulus and the last adapting stimulus (Masri et al. 2008). (3) Response reliability, defined as the percentage of trials where a response was detected within 20ms in response to each pulse of the repetitive stimulation (8-10Hz) (Mainen and Sejnowski 1995). Thalamic units with average first-spike latency of more than 12 ms, latency shift of more than 20ms, or response reliability of less than 20% were excluded (Liew et al. 2021).

3.2.7.3 Cortical unit classification

S1 layer IV is the major thalamocortical recipient from VPM projections, where a diversity of cell types receive these feedforward synaptic inputs (Bruno and Simons 2002). Here, we classified cortical units as fast-spiking units (FSUs) or regular-spiking units (RSUs) from the time interval between trough to peak (tt2p) of the spike waveform (Barthó et al. 2004).

3.2.7.4 Neuronal response analyses

Rostral-caudal pulse deflections were delivered using a simple exponential sawtooth in whisker angle (300 deg/s). In general, whisker evoked activity was quantified within a 30 ms window following stimulus onset, unless specified otherwise. Evoked response amplitudes were characterized from the trial-to-trial spike count in the window of interest following each deflection, and response latencies were defined as onset latencies of the first spike within the response window, averaged across trials. Normalized evoked response amplitude was defined as the spike count in the window of interest, divided by the response amplitude evoked by the first deflection. Adaptation ratio was computed as the averaged spike count elicited by the last three pulses for each cell, normalized to the averaged response to the first three deflections

3.2.7.5 Characterization of the adaptation dynamics with exponential models

In many cases, the adaptive reduction in response amplitudes was not well-characterized by a single exponential model. Therefore, the normalized evoked response for the 1.5-sec and 10-sec stimulus conditions was fitted with multi-exponential models

and the goodness of fit was quantified for each model. A bi-exponential model was sufficient to capture the adaptation dynamics observed in this study.

For a single term, the following exponential function was used: For a single term, exponential function, we used the following simple equation:

$$y(t) = a * e^{-\lambda * t}$$

where $y(t)$ is the normalized evoked response at time t , λ is the time constant of adaptation, and a is a scaling factor.

For a double term exponential function, the following equation was used:

$$y(t) = a * e^{-\lambda_1 * t} + b * e^{-\lambda_2 * t}$$

where $y(t)$ is the normalized evoked response at time t , λ_1 and λ_2 are the time constants of two timescales of adaptation, and a and b are scaling factors.

3.2.7.6 Velocity tuning analysis

To measure velocity tuning properties of thalamocortical neurons, we quantified the whisker response with respect to randomly presented angular deflection velocities of 50, 125, 300, 600, 900, 1200 deg/s, either in isolation (Control) or immediately following adapting stimuli (1.5-sec or 10-sec). Note that deflection was presented as an additional deflection following the 10 Hz (100 ms after the last pulse of adapting stimuli) after the adapting stimuli.

3.2.7.7 Spike cross-correlation analysis

For paired recordings in topographically aligned thalamocortical regions, spike cross-correlation analysis was performed to (1) infer monosynaptic connectivity, (2) compute synaptic efficacy on a subset of neuronal pairs, and (3) compute thalamic population synchrony. All analyses were performed on a trial-by-trial basis. Given a spike in a ‘reference’ neuron, the relative times of the spikes were computed from a ‘target’ neuron that occurred within a 25-millisecond window before and after each reference spike. All cross-correlograms were constructed using 0.5 milliseconds bin. Using a previously developed method for the monosynaptic connectivity inference (Liew et al. 2021), the thalamocortical circuit was externally driven with a weak whisker stimulus (see Methods: Weak sinusoidal stimulus), and then a histogram of cortical firing relative to thalamic spike times was constructed, often referred as the raw spike cross-correlogram. To correct for correlated stimulus-locked activity, a shuffle-corrected spike cross-correlogram was generated by randomizing the trials of the thalamic and cortical spiking activity relative to each other. This effectively destroys any elements of the cross-correlogram that are due to the stimulus. To conclude that a neuronal pair was ‘connected’, two criteria were adopted that were expanded from previous studies (Bruno and Sakmann 2006; Reid and Alonso 1995; Swadlow and Gusev 2001) based on both the raw and shuffle-corrected cross-correlogram: (Criterion 1) a notable sharp, millisecond-fine peak is observed within a narrow lag of 1-4 ms after a thalamic spike, that is the maximum in the raw cross-correlogram; and (Criterion 2) this fast ‘monosynaptic peak’ is significant or still present after accounting for (subtracting) stimulus-induced correlation (Liew et al. 2021).

For the synaptic efficacy computation, the number of spikes within a 1-3 ms window of the shuffled-corrected spike cross-correlogram was divided by the total number

of thalamic spikes used in the analysis. To quantify the effects of adaptation on synaptic transmission across the TC junction, synaptic efficacy was computed using the transient responses (80 ms after stimulus onset) from each individual deflection during persistent stimulation. Baseline synaptic efficacy was computed with a similar approach, but with spiking activity evoked by the weak sinusoidal stimulus.

To measure the level of presynaptic synchronization in thalamus, synchrony strength were computed using a central area under the raw cross-correlogram for all thalamic pairs that responded to the same principal whisker. Thalamic synchrony was computed for each thalamic pair using the total number of spikes within a 15 ms (± 7.5 ms) window of the cross-correlogram, divided by the total number of spikes in the raw cross-correlogram (± 25 ms window) (Borden et al. 2022; Wright et al. 2021b).

3.2.7.8 Receiver operator characteristic (ROC) analysis

To evaluate the functional consequences of the effects of adaptation over time scales, the theoretical detectability and discriminability of a sensory feature were calculated for significantly responsive FS and RS neurons by applying ideal observer analysis (Ollerenshaw et al. 2014; Wang et al. 2010; Whitmire et al. 2016; Wright et al. 2021b). For baseline activity, the spike count 30-ms before the stimulus onset on each trial was used, generating what was referred to as the Noise distribution. FS and RS evoked responses were quantified as the number of elicited spikes in response to transient stimuli within a 30 ms window. For each cortical unit, a spike count probability distribution was estimated from the empirical data, using the across-trial mean (μ) and standard deviation of spike count per stimulus. A parameterized ‘population’ distribution was constructed for each

cell using a Gamma distribution, $\Gamma(N\alpha, \Theta)$, where $\alpha = \mu^2/\sigma^2$, $\Theta = \sigma^2/\mu$, and N is the assumed number of identical neurons that share response properties similar to the neuron recorded experimentally. Results were reported using $N = 10$ and draw samples ($n = 1000$ trials) from the ‘population’ distribution, but results were qualitatively similar for $N = 1, 5$ and 20 . ROC curves were generated by sliding the threshold across the noise and signal distributions, generating a range of false alarm rates versus hit rates that reflect the degree of overlap of the distributions. The area under the ROC curve (AUROC) was used as a performance metric for theoretical detectability. Note that higher AUROC values indicate better performance, where an AUROC value of 1 corresponds to zero overlap between signal and noise distributions (an ideal detector) and an AUROC value of 0.5 corresponds to complete overlap between distributions, hence operating at chance. For theoretical discriminability, the ability of an ideal observer to discriminate between seven different velocities was quantified based on the observed cortical activity. As described above, the spike count distributions were parameterized with a Gamma distribution, and a performance matrix was determined by the amount of overlap between the different velocity distributions. Although the thalamic and cortical activity was recorded in response to seven velocities (see Methods: Sensory Stimulus), for simplicity the analysis was restricted to 5 different velocities (125, 300, 600, 900 and 1200 deg/s). Thus, the performance matrix is a 5x5 matrix, in which the (i,j) element is the probability of assigning the observed response to stimulus s_j when the real stimulus is s_i . The theoretical discrimination performance was calculated as the sum of all diagonal elements of the performance matrix. The accuracy of the observer is then compared to the correct stimulus

classification. Given that the five velocities were each presented with equal probability, operating at chance discrimination corresponds to a probability of 0.2.

3.3 Results

3.3.1 *Diversity of adaptation dynamics in the thalamus and cortex*

We recorded extracellularly using multi-channel silicon probes in the vibrissa lemniscal pathway of the isoflurane-anesthetized, head-fixed mouse. We simultaneously measured population single-unit activity in the ventro-posteromedial thalamus (VPm) and primary somatosensory “barrel” cortex (S1 Layer 4) in response to repetitive, precise deflections of a single whisker on the contralateral side of the face using a computer-controlled actuator (Figure 3-1A; also see Methods). Well-isolated, sensory responsive single units in VPm thalamus and S1 cortical layer 4 were identified, and cortical single units were further parsed into RS (putative excitatory) and FS (putative inhibitory) neurons based on properties of the spike waveform (Figure 3-1A; also see Methods). We measured the effects of adaptation induced by 10 Hz repetitive stimulation (each pulse was a transient, 300 deg/s sawtooth sensory feature) on spiking activity in VPm and cortical S1 layer 4 FS and RS cells, as shown on Figure 3-1A right. For all responsive, well-isolated single units that we have recorded in the thalamus and cortex, we parsed them into three distinct categories based on a statistical test (Wilcoxon signed-rank test) comparing the evoked response of the first and last pulse of the adapting stimulus: increased-firing, decreased-firing and no change (Figure 3-1B). Figure 3-1B showed evoked response for all data (VPm: $n = 161$, FS: $n = 127$, RS: $n = 57$), randomly down sampled to 60% of the data for better visualization. Cells that showed significant response (either increased or

decreased firing rate) were color coded (VPm – blue, FS – red, RS – yellow) and gray data points indicate cells that showed no significant change in response. Despite variability across neurons, we found that most responsive neurons across these regions exhibit the largest responses to the first few pulses in the stimulus train and adapt strongly to persistent, ongoing sensory stimuli, as evident in the peri-stimulus time histograms (PSTHs) of representative neurons for each cell type (Figure 3-1A) and population-averaged mean evoked response (Figure 3-1B), each normalized to its control (response to the first deflection). Notably, more than 75% of the neurons showed significant reduction in firing rate over the time course of repetitive stimulation, while the remaining cells either showed increased firing or no change (Figure 3-1C, VPm (n = 161); FS (n = 127); RS (n = 57)). For the remainder of the study, our analysis focused exclusively on cells that showed a significant decrease in firing rate. At the thalamocortical junction, sensory thalamic neurons in the VPm adapted to a lesser degree than cortical layer 4 FS and RS neurons in terms of response amplitude (Figure 3-1D), whereas the decrease in responsiveness over time for cortical neurons was generally more pronounced in the RS than FS population. Note that as we assessed the adaptation responses for each sub-population of neurons, we consistently observed a drastic reduction in response amplitude that occurred between 0 to 1.5 seconds, and a more gradual reduction in responsiveness that occurred later in time (1.5 to 10 seconds, Figure 3-1E), potentially suggesting distinct adaptation dynamics over multiple timescales. Hence, we focused the quantification of adaptive dynamics at these two time points as compared to control (Figure 3-1D, gray lines indicate three time points of interest, Control, 1.5-sec, and 10-sec adaptation) throughout the rest of the study. In general, all thalamocortical cell types exhibit significant reduction in response amplitude

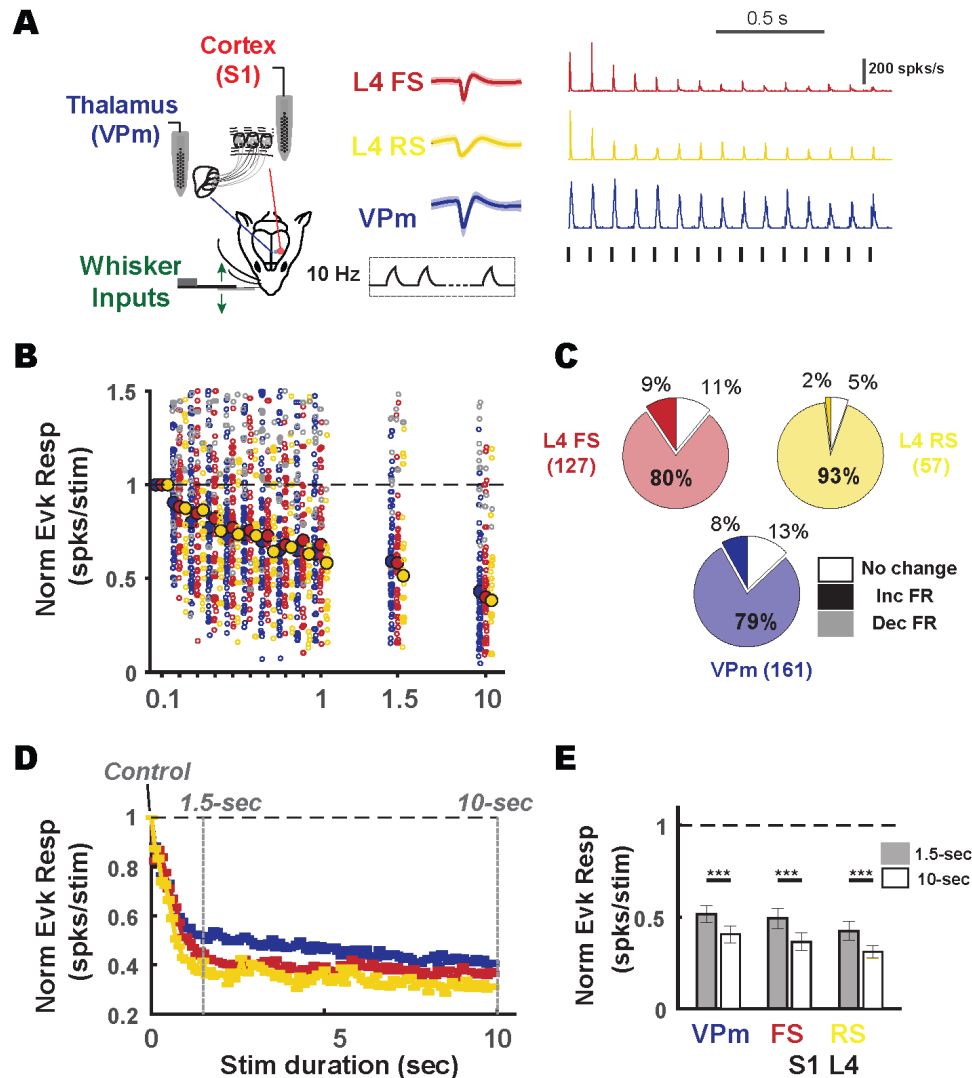


Figure 3-1. Experimental approach and differential adaptation across VPm – S1. A. Experimental setup. We performed extracellular recordings in the ventral posteromedial (VPm) nucleus of the thalamus and in layer IV of primary somatosensory cortex (S1) in anesthetized mouse using 32-channel silicon probes. Precise deflections were delivered to single whisker using computer-controlled actuator. Mean waveforms (\pm SEM) for typical, well-isolated FS (red), RS (yellow) and VPm (blue) neurons. Adaptation was induced using a train of sawtooth punctate sensory stimuli (300 deg/s) delivered in 10Hz. Shown also are example peri-stimulus time histograms (PSTHs) for example cells on the left in response to 10Hz repetitive stimulation. **B.** At each time point (vertical distribution at each x-value), every circle corresponds to the evoked response (quantified as spikes per stimulus within 30-ms window after stimulus onset) of an individual neuron. Filled colored circles indicate neurons with statistically significant difference comparing first

deflection and last deflection in the adapting train. Red, yellow and blue correspond to FS, RS, and VPm neuron respectively. Gray circles represent neurons with no statistically significant change. Solid, darker colored circles represent the mean evoked response for each cell type. All cells generally showed decline in responsiveness over the time course of repetitive stimulation. Note that evoked response for each cell was normalized to the maximum response of first three deflections. **C.** Bar charts showed distribution of responsive neurons that showed increased, decreased, and no change in firing rate in (C). Majority of putative inhibitory neurons (FS, red), putative excitatory neurons (RS, yellow) and thalamic neurons (VPm, blue) decreased in firing rate in response to repetitive stimulation. [FS – 77% (N = 127), RS - 90% (N = 57), and VPm – 83% (N = 161)]. **D.** Population-averaged mean evoked response for VPm, FS and RS in (C) during exposure to 10-second (sec) adaptation. **E.** Thalamocortical neurons exhibit additional reduction in evoked response comparing 1.5-sec and 10-sec adaptation.

3.3.2 *Signature of adaptation dynamics with multiple timescales in the thalamus and cortex*

Neurons in VPm thalamus generally exhibited short-latency, transient spiking activity in response to the first punctate stimulus (Control) in the adapting train (Figure 3-2A, Grand PSTH, n = 119 VPm units). For subsequent stimulation, we observed a monotonic decrease in thalamic spiking response as a function of adaptation duration, as shown in the right two panels of Figure 3-2A. Notably, adaptation dynamics in the VPm thalamus did not show saturation at 1.5-sec and continued to progress over a longer timescale. In addition to the rapid reduction in response and increased response latency in the first 1.5 seconds, we observed a further reduction in evoked responses (Figure 3-2B) and a corresponding increase in spiking latencies (Figure 3-2C) when we compared the 1.5-sec adapted condition with the 10-sec adapted condition. To further quantify the effects of adaptation on a cell-by-cell basis, we measured the normalized evoked response for each cell (evoked response for each deflection was normalized to the first pulse) and also computed the adaptation ratio, defined as ratio of mean spike count for the last three pulses

divided by the mean spike count for the first three pulses. Both metrics indicated significant reduction in response amplitude over time. To characterize the timescale of the decay in responsiveness of thalamic neurons, we fitted the normalized population-averaged mean evoked response as a function of stimulus duration with exponential models (see Methods). Although adaptation is widely characterized as a simple, single exponential delay, we found that the declining profile of the adaptation response over the 10-sec repetitive stimulation was better characterized with a dual-exponential ($R^2 = 0.99$) compared to a single-exponential function ($R^2 = 0.83$), shown in Figure 3-2F. This trend was even more evident when plotted on log-linear axes (Figure 3-2G), where we observed two linear regimes, suggestive of two distinct timescales. Note that we also observed two distinct timescales on a cell-by-cell basis for the thalamic population (data not shown).

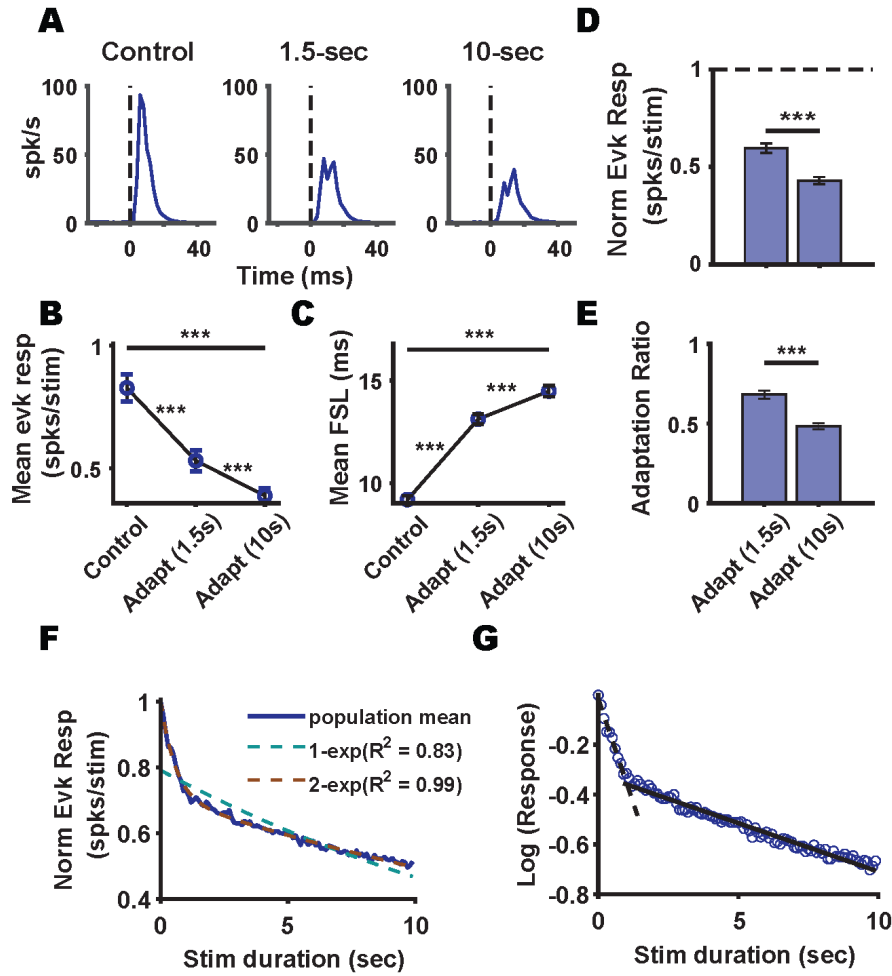


Figure 3-2. Adaptation dynamics of thalamic population in response to repetitive stimulation.

A. Grand-averaged PSTHs for all responsive VPM neurons (N = 119) over the time course of stimulation, showing three specific time points [left to right: Control (1st deflection), 1.5-sec adapted (15th deflection) and 10-sec adapted (100th deflection)]. **B.** Mean evoked firing rate for all responsive VPM neurons. N = 119 neurons, Control: 0.83 ± 0.06 spk/stim, 1.5-sec adapted: 0.53 ± 0.04 spk/stim, 10-sec adapted: 0.39 ± 0.03 spk/stim. Control versus 1.5-sec adapted: $p = 6.75 \times 10^{-12}$; 1.5-sec adapted versus 10-sec adapted: $p = 2.15 \times 10^{-15}$, Control versus 10-sec adapted: $p = 5.10 \times 10^{-19}$, Wilcoxon signed-rank test. *** $p < 0.0005$, ** $0.0005 \leq p < 0.005$, Wilcoxon signed-rank test. **C.** Mean first-spike latencies. N = 119 neurons, Control: 9.2 ± 0.18 ms, 1.5-sec adapted: 13.1 ± 0.25 ms, 10-sec adapted: 14.5 ± 0.27 ms (mean \pm SEM). Control versus 1.5-sec adapted: $p = 5.29 \times 10^{-21}$; 1.5-sec adapted versus 10-sec adapted: $p = 4.95 \times 10^{-15}$, Control versus 10-sec adapted: $p = 3.11 \times 10^{-21}$, Wilcoxon signed-rank test. *** $p < 0.0005$, ** $0.0005 \leq p < 0.005$, Wilcoxon signed-rank test. **D.** Population-averaged normalized evoked response for two adapted states across all VPM neurons (n = 119). Control versus 1.5-sec adaptation: 0.60 ± 0.02 , Control vs 10-sec adaptation: 0.43 ± 0.02 . Difference between 1.5-sec and 10-sec, $p = 3.48 \times 10^{-16}$, Wilcoxon signed-rank test. **E.** Population-averaged adaptation ratio for two adapted states, 1.5-sec

adapted, and 10-sec adapted (N = 119). Adaptation ratio, defined as the ratio of the mean spike count for the last three pulses divided by the mean spike count for the first three pulses. Percentage: Control versus 1.5-sec adaptation: $68 \pm 2.6 \%$, Control vs 10-sec adaptation: $48 \pm 1.9 \%$ Difference between 1.5-sec and 10-sec, $p = 9.17 \times 10^{-20}$, Wilcoxon signed-rank test. **F.** Population-averaged normalized evoked response for VPM neurons (N = 119) fitted with single exponential (green dashed line) and bi-exponential models (brown dashed line). Note that bi-exponential function best fits the data ($R^2 = 0.99$) as compared to single-exponential ($R^2 = 0.83$). **G.** Log-linear plot of normalized evoked response measured from grand-averaged PSTHs for all responsive VPM neurons shown in (A) over the time course of 10-sec repetitive stimulation. Black, dashed lines denote the linear fit over two timescales, suggesting bi-exponential behavior ($\tau_1 = 0.57$ s, $\tau_2 = 27.8$ s).

To capture the transformation across the thalamocortical junction, we recorded from the downstream VPM-recipient cells in S1 cortical layer 4. Figure 3-3A and Figure 3-3B illustrate that the gradual decline in the neuronal response over the time course of repetitive stimulation was generalized to all recorded S1 layer 4 FS (n = 101) and RS (n = 53) neurons, as shown in the Grand PSTHs for control (first deflection), 1.5-sec adapted (15th deflection), and 10-sec adapted (100th deflection) conditions. This is summarized by the mean stimulus evoked firing rate at these time points and the corresponding adaptation ratio, in Figure 3-3C and Figure 3-3D, respectively. Consistent with previous studies (Gabernet et al. 2005b; Heiss et al. 2008; Simons and Carvell 1989), the RS population adapted more than the FS population, as reflected in the mean evoked rate (Figure 3-3C) and adaptation ratio in Figure 3-3D (1.5-sec adapted (FS: $70 \pm 0.3 \%$, RS: $64 \pm 4.5 \%$), 10-sec adapted (FS: $47 \pm 2.2 \%$, RS: $44 \pm 2.6 \%$). 1.5-sec vs 10-sec adapted, FS: $p = 3.77 \times 10^{-17}$, FS: $p = 1.29 \times 10^{-8}$, Wilcoxon signed-rank test.). Note that both the cortical FS and RS populations showed a much greater degree of attenuation in response amplitude than the VPM population, as observed qualitatively in Figure 3-1D. However, similar to VPM, the overall reduction in responsiveness for both FS and RS neurons was still better characterized with bi-exponential models, as illustrated in Figure 3-3E and F.

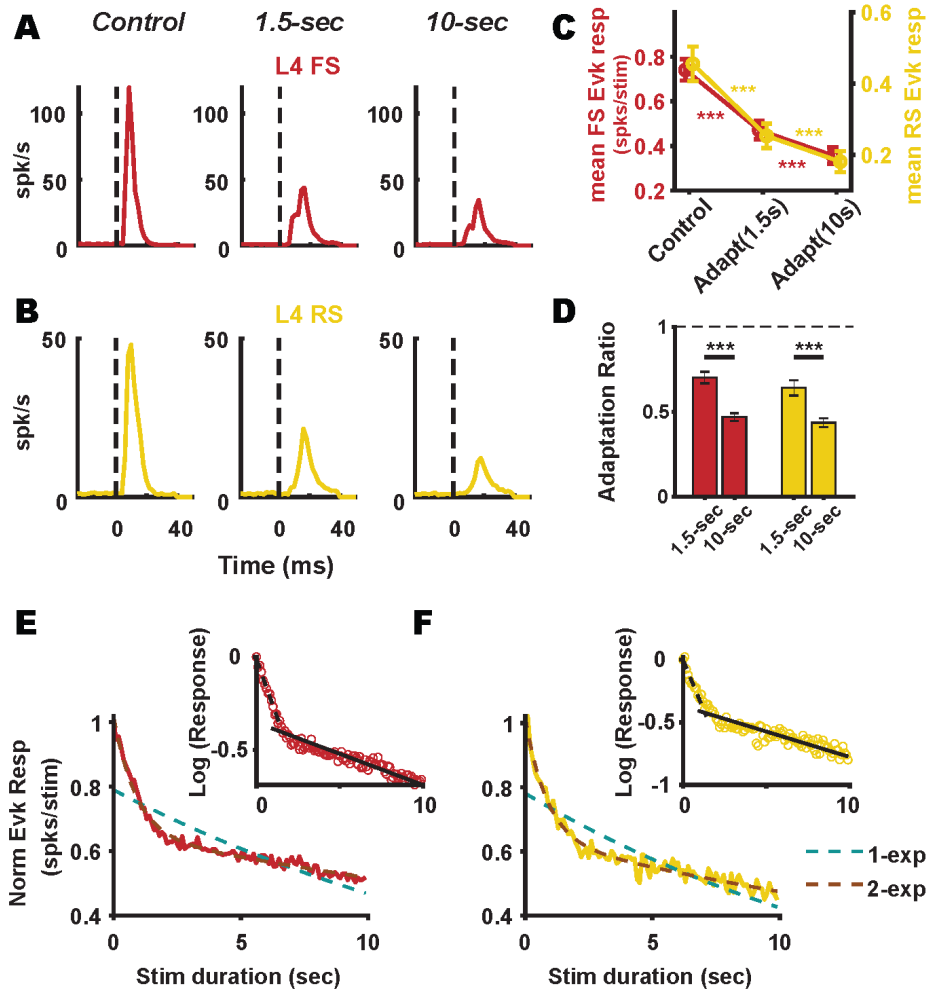


Figure 3-3. Evolution of adaptation dynamics of cortical cells during exposure to repetitive stimulation.

A. Grand-averaged PSTHs for all responsive S1 layer 4 FS neurons ($N = 101$) over the time course of stimulation, showing three specific time points [left to right: Control (1st deflection), 1.5-sec adapted (15th deflection) and 10-sec adapted (100th deflection)]. **B.** Same as (A) but for RS neurons ($N = 53$). **C.** Mean evoked firing rate for all responsive S1 layer 4 FS (red, $N = 101$) and RS (yellow, $N = 53$) neurons over the time course specified in (A). $***p < 0.0005$, $**0.0005 \leq p < 0.005$, Wilcoxon signed-rank test. **D.** Population-averaged adaptation ratio for two adapted states, 1.5-sec adapted, and 10-sec adapted for FS (red, $N = 101$) and RS (yellow, $N = 53$). 1.5-sec adapted (FS: $70 \pm 0.3\%$, RS: $64 \pm 4.5\%$), 10-sec adapted (FS: $47 \pm 2.2\%$, RS: $44 \pm 2.6\%$). 1.5-sec vs 10-sec adapted, FS: $p = 3.77 \times 10^{-17}$, RS: $p = 1.29 \times 10^{-8}$, Wilcoxon signed-rank test. $***p < 0.0005$, $**0.0005 \leq p < 0.005$, Wilcoxon signed-rank test. **E.** Population-averaged normalized evoked response for S1 layer 4 FS neurons ($N = 101$) fitted with single and bi-exponential models (green and brown lines denote fitting). Note that bi-exponential function best fits the data ($R^2 = 0.98$, R^2 (1-exp): 0.74). Inset: Log-linear plot of normalized evoked response measured from grand-averaged PSTHs for all responsive FS neurons shown in (A) over the time course of 10-sec repetitive stimulation. Black and dashed lines denote the linear fit over two

timescales, suggesting bi-exponential behavior ($\tau_1 = 0.88$ s, $\tau_2 = 43.3$ s). **F.** Population-averaged normalized evoked response for S1 layer 4 RS neurons ($N = 53$) fitted with single and bi-exponential models (green and brown lines denote fitting). Note that bi-exponential function best fits the data ($R^2 = 0.97$) as compared to single exponential ($R^2 = 0.75$). Inset: Log-linear plot of normalized evoked response measured from grand-averaged PSTHs for all responsive RS neurons shown in (B) over the time course of 10-sec repetitive stimulation. Black and dashed lines denote the linear fit over two timescales, suggesting bi-exponential behavior ($\tau_1 = 0.85$ s, $\tau_2 = 33.9$ s).

3.3.3 *Role of thalamocortical synaptic depression and thalamic synchrony as adaptation mechanisms across timescales*

The clear observation of multiple timescales of adaptation across the thalamocortical circuit opens up the possibility of the involvement of multiple distinct mechanisms underlying the adaptation dynamics. We have identified three distinct mechanisms that could contribute to cortical adaptation that we observed in S1 layer 4, summarized in the conceptual framework (Figure 3-4). The multi-timescale adaptive dynamics identified in both the FSU and RSU populations could be due to 1) a drop in synchronous inputs from the thalamic population, 2) depression of thalamocortical synapses, and/or 3) intracortical interactions in the local cortical microcircuit. Note that these potential mechanisms are not mutually exclusive, and thus the observations here could be a complex integration of these candidate mechanisms.

Previous studies in this particular pathway have suggested that depression of the thalamocortical (TC) synapse (Chung et al. 2002) and the loss of synchrony across the thalamic population (Wang et al. 2010) could both play a significant role in adaptation in the primary sensory cortex. Work in the visual pathway has previously shown that the recurrent network in the primary sensory cortex also contributes to the feedforward excitation exhibited in the excitatory cells, however this intracortical mechanism

dominates the later part (~40ms after stimulus onset) of the sensory-evoked response (Reinhold et al. 2015). Therefore, in this work, we focused on the first two mechanisms that were thalamic-centric.

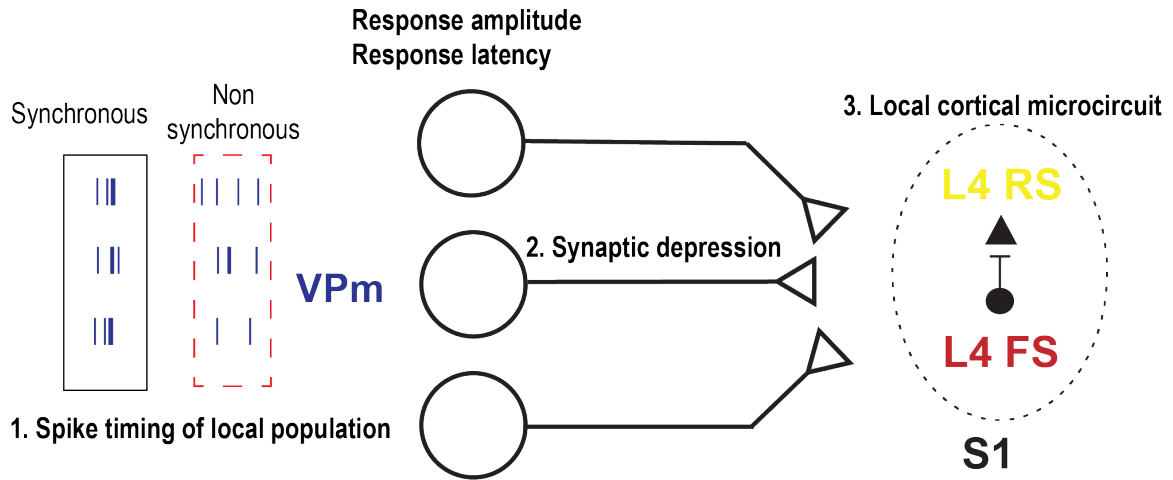


Figure 3-4. Conceptual framework of potential mechanisms underlying cortical adaptation.

Rapid adaption is observed throughout the thalamocortical circuit, but the signatures of the adaptation are distinctly different between thalamus and cortex, and within cortex between excitatory and inhibitory neurons. Three potential mechanisms that can transform thalamic activity and contribute to cortical adaptation include 1) changes in spike timing of the local thalamic population, 2) depression of thalamocortical synapses, and 3) intracortical interactions between the excitatory and inhibitory sub-populations.

First, in order to evaluate the dynamics of the thalamocortical (TC) synapse, we examined the adaptation dynamics in putatively connected VPm-S1 pairs using previously established methods for identifying monosynaptic connectivity from recorded spiking activity across thalamus and cortex (Liew et al. 2021). Figure 3-5A shows raster plots of a representative example a L4 FS neuron in S1, a L4 RS neuron in S1, and a VPm neuron, respectively, that were recorded simultaneously in response to a weak sinusoidal whisker stimulus. Note that the firing rate of all cells was elevated but not stimulus-locked in general. Out of 192 pairs of VPm-S1 neurons that were recorded simultaneously in

topographically-aligned regions, we identified 44 pairs that were likely to be monosynaptically connected (Figure 3-5B), inferred using a stringent cross-correlation analysis of spiking activity (see Methods). Figure 3-5B shows an example of a synaptically connected VPM-FS pair and a VPM-RS pair. Overall, in these recordings we observed significantly more monosynaptically connected VPM-FS (86%) than VPM-RS (13%) pairs, potentially due to the intrinsic elevated firing rates of the FS neurons. After inferring the likelihood of monosynaptic connectivity, we assessed synaptic efficacy in this subset of connected VPM-S1 pairs. Synaptic efficacy is a measure designed to capture the strength of a particular synapse and is defined as the probability of an S1 neuron spike following a spike of the pre-synaptic VPM neuron. Specifically, synaptic efficacy is calculated as the number of synchronous spikes of the S1 neuron within the 1-3 ms window following each thalamic spike, divided by the number of thalamic spikes in the shuffled-corrected cross-correlogram. To evaluate the change in synaptic efficacy over the time course of adaptation, we calculated TC efficacy at each deflection of the repetitive stimulation. Note that to eliminate the stimulus-driven correlation during the efficacy computation, we shuffled the trials of cortical spiking and subtracted that of the raw cross-correlograms. The efficacy values were then computed using the shuffled-corrected cross-correlograms. To estimate the effects of a single presynaptic (thalamic) spike on cortical spiking (Swadlow and Gusev 2001), we selected a brief window (1-3 ms lag), indicated by the shaded region in Figure 3-5D for this computation. This was necessary to estimate the effects of a single presynaptic (thalamic) spike on cortical spiking (Swadlow and Gusev 2001). Figure 3-5D shows the grand-averaged shuffled-corrected cross-correlograms generated from the spiking responses (quantified using spikes within an 80 ms window after stimulus onset),

evaluated for the Control, 1.5-sec adapted (15th deflection), and 10-sec adapted (last deflection) conditions of the 10-Hz repetitive stimulation. We observed a significant drop in efficacy values during the initial adaptation period (41% drop at 1.5-sec adapted), followed by a gradual decline over time (10% additional drop at 10-sec). We found that this reduction exhibits a monotonic decreasing trend ($p = 1.12e-4$, Mann-Kendall Trend Test). It is important to note that this metric is not likely purely a function of TC synaptic depression, but also reflects stimulus-driven synchronization of the thalamic population. However, the result does suggest that TC synaptic depression likely plays a role in the initial 0 -1.5 seconds of cortical adaptation, more so than over longer timescales.

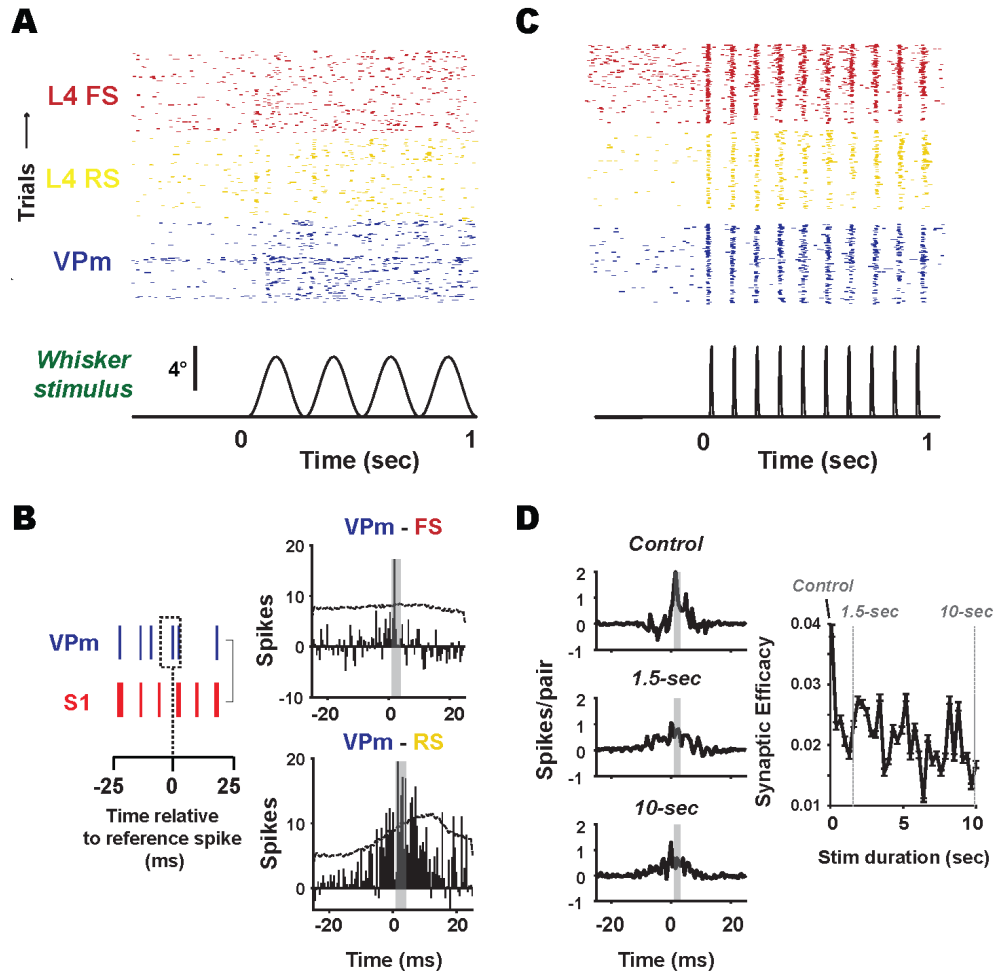


Figure 3-5. Adaptation reduces synaptic efficacy monotonically in synaptically connected thalamocortical neurons.

A. Raster plots show example spiking activity of simultaneously recorded L4 RS, FS and VPM neuron. For monosynaptic connectivity inference, low velocity sinusoidal input (4Hz, mean velocity: 25-50 deg/s) was used to elevate spiking activity across the thalamus and cortex. **B.** Schematic shows how cross-correlogram was computed for each VPM-S1 pair and a representative example of VPM-FS and VPM-RS pair respectively. **C.** Same as A but transient, adapting sawtooth stimulus, followed by a single velocity probe (stimulus used in Figure 3-6 and Figure 3-7). **D.** Using subpopulation of VPM-S1 pairs that showed putative monosynaptic connection, we estimated synaptic efficacy during the 10-sec repetitive stimulation. Shown are the grand-averaged shuffled-corrected (removed stimulus-correlation) cross-correlograms generated from the spiking responses (quantified using 80 ms window after stimulus onset) of 44 pairs of putatively monosynaptically connected VPM-S1 neuronal pairs in response to Control (1st deflection), 1.5-sec adapted (15th deflection) and 10-sec adapted (100th deflection), total evaluated VPM-S1 pairs = 192. Shown is synaptic efficacy over time course of repetitive stimulation. Synaptic efficacy was monotonically reduced by repetitive stimulation ($p = 1.12 \times 10^{-4}$, Mann-Kendall Trend Test). Synaptic efficacy, defined as number of synchronous spikes within 1-3 ms

window divided by number of thalamic spikes in the shuffled-corrected cross-correlograms of each stimulation (see Methods).

In addition to the adaptive properties of the thalamocortical synapse, there is growing evidence for a role of thalamic spike timing and synchrony in cortical adaptation (Usrey et al., 2000; Swadlow and Gusev, 2001; Bruno and Sakmann, 2006; Wang et al., 2010; Ollerenshaw et al., 2014; Wright et al., 2021), yet this has not been investigated systematically over multiple timescales. It has been previously shown that sensory adaptation increases thalamic response latencies and decreases the timing precision of stimulus-driven thalamic spiking over relatively fast time scales (Bolori et al. 2010). Here, we found that repetitive stimulation over a longer 10-sec period continued to modulate thalamic spike timing, increasing the jitter in response latency even further in the thalamic population, as shown qualitatively in Figure 3-6A. Notably, repetitive stimulation over 10-sec caused a monotonic increase in mean first-spike latency jitter in the thalamic population (Figure 3-6B and C, $n = 119$ neurons), reflecting a loss in thalamic timing precision. Given that we simultaneously recorded activity from numerous pairs of VPM neurons (Figure 3-6D, $n = 272$ pairs), we further quantified the effects of the loss in timing precision on the population synchrony. For each recorded thalamic pair, we generated the spike cross-correlogram (see Methods). We defined thalamic synchrony as the number of spikes that were within ± 7.5 ms around zero lag, divided by the total number of spikes within the cross-correlogram (CCG). A schematic of the synchrony calculation is shown in Figure 3-6D. We found that thalamic population synchrony was rapidly decreased over the first 1.5 seconds, but was also significantly reduced over the longer time course of the 10-sec adaptation (Figure 3-6E), likely having an appreciable impact on the corresponding cortical

response, given that S1 processing has previously been shown to be highly sensitive to the change in timing of thalamic inputs (Bruno and Sakmann 2006; Ollerenshaw et al. 2014; Pinto et al. 2000; Swadlow and Gusev 2001; Wang et al. 2010). We assessed the change in thalamic synchrony in response to five different velocities including 300 deg/s (red), 450 deg/s (green), 600 deg/s (brown), 900 deg/s (pink), and 1200 deg/s (blue), as shown in color-coded horizontal bars on the left and right axes of Figure 3-6F for the Control and 10-sec adaptation conditions. We found that the distributions of thalamic population synchrony for these different velocities become more separated in the 10-sec adapted condition as compared to Control (Color-coded horizontal bars on the left depicted measures of synchrony for 5 different velocities probed right after Control condition, Red (300 deg/s): 0.88 ± 0.01 , Green (450 deg/s): 0.86 ± 0.01 , Brown (600 deg/s): 0.84 ± 0.01 , Pink(900 deg/s): 0.87 ± 0.01 , Blue (1200 deg/s): 0.87 ± 0.01). Color-coded horizontal bars on the right are measures of synchrony for 5 different velocities after the 10-sec adaptation (Red (300 deg/s): 0.48 ± 0.02 , Green (450 deg/s): 0.57 ± 0.01 , Brown (600 deg/s): 0.66 ± 0.01 , Pink (900 deg/s): 0.71 ± 0.01 , Blue (1200 deg/s): 0.67 ± 0.01). Given the sensitivity of the downstream cortical layer 4 thalamorecipient neurons to the relative timing of convergent thalamic inputs, these results suggest that the adaptation further increases cortical sensitivity to velocity through this synchrony mechanism.

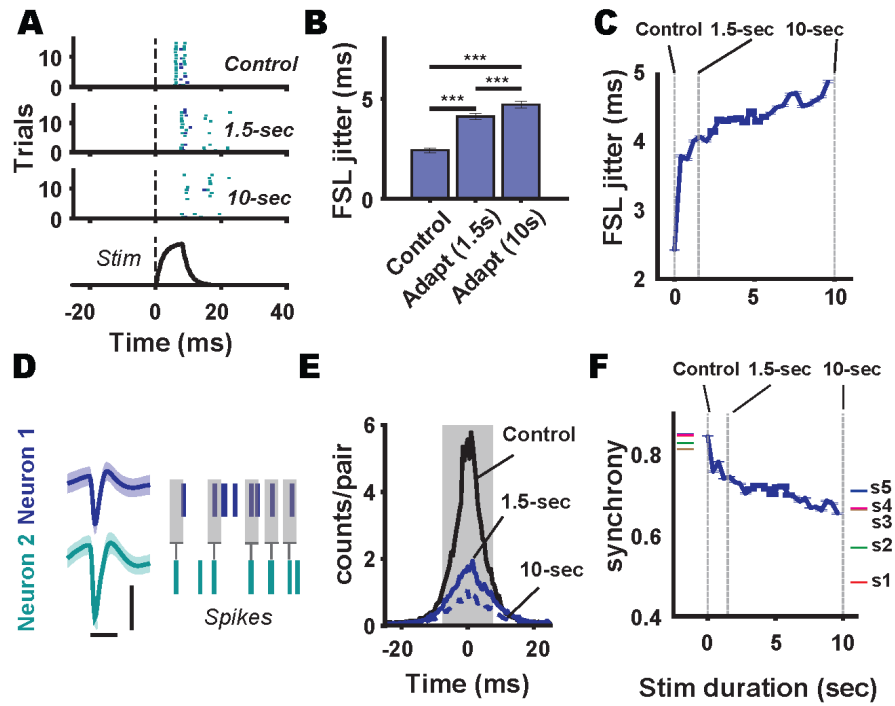


Figure 3-6. Adaptation reduces timing precision and pairwise synchrony in the thalamic population.

A. Spiking activity ($n = 10$ trials) of an example VPM neuron pair (Neuron 1 and Neuron 2) in response to the 10 Hz repetitive stimulation, comparing control (1st deflection), 1.5-sec adapted (15th deflection) and 10-sec adapted (100th deflection). Shown below the raster-plot is the punctate whisker deflection for the 300 deg/s stimulus. **B.** Population-averaged first spike latency jitter in response to control (1st deflection), 1.5-sec adapted (15th deflection) and 10-sec adapted (100th deflection) condition ($N = 119$). Note that there was a significant increase in jitter of the first spike latency over the time course of repetitive stimulation. $***p < 0.0005$, $**0.0005 \leq p < 0.005$, Wilcoxon signed-rank test. ($N=119$, Control: 2.4 ± 0.12 ms, 1.5-sec adapted: 4.1 ± 0.15 ms, 10-sec adapted: 4.7 ± 0.16 ms, mean \pm SEM). Control versus 1.5-sec adapted: $p = 3.08 \text{ e-}17$; 1.5-sec adapted versus 10-sec adapted: $p = 7.39 \text{ e-}7$, Control versus 10-sec adapted: $p = 2.67 \text{ e-}18$, Wilcoxon signed-rank test. **C.** Population-averaged first spike latency jitter as a function of stimulus duration. **D.** Spike waveforms of example VPM neuron pair (Neuron 1 and Neuron 2) in A. Vertical scale bar: 100 μ V. Horizontal scale bar: 1 ms. Schematic shows how the spike cross-correlogram between Neuron 1 and Neuron 2 was constructed. A count of spikes of Neuron 1 was tabulated at specific time delays (± 7.5 ms) with respect to the spikes of Neuron 2 (see Methods). **E.** Grand-averaged cross-correlograms for thalamic pairs that were simultaneously recorded ($n = 272$ pairs, $N = 119$ neurons) comparing control (1st deflection), 1.5-sec adapted (15th deflection) and 10-sec adapted (100th deflection) conditions. Population-averaged thalamic synchrony ($N = 119$), Control: 0.84 ± 0.01 , 1.5-sec adapted: 0.74 ± 0.01 , 10-sec adapted: 0.67 ± 0.02 . $***p < 0.0005$, $**0.0005 \leq p < 0.005$, Wilcoxon signed-rank test. Control versus 1.5-sec adapted: $p = 4.24 \text{ e-}17$; 1.5-sec adapted versus 10-sec adapted: $p = 2.38 \text{ e-}4$, Control versus 10-sec adapted: $p = 2.16 \text{ e-}20$, Wilcoxon signed-rank test. **F.** Population-averaged thalamic synchrony over the 10-sec repetitive stimulation. Note that thalamic population synchrony decreased monotonically with time. Synchrony was measured as the number of spikes within the central peak (± 7.5 ms) divided by total number of spikes within the cross-correlogram (CCG). Color-coded horizontal bars on the left depicted measures of synchrony for 5 different velocities probed right after Control condition, Red (300 deg/s): 0.88 ± 0.01 , Green (450 deg/s): 0.86 ± 0.01 , Brown (600 deg/s): 0.84 ± 0.01 , Pink(900 deg/s): 0.87 ± 0.01 , Blue (1200 deg/s): 0.87 ± 0.01 . Color-coded horizontal bars on the right are measures of synchrony for 5 different velocities after 10-sec adaptation. Red (300 deg/s): 0.48 ± 0.02 , Green (450 deg/s): 0.57 ± 0.01 , Brown (600 deg/s): 0.66 ± 0.01 , Pink (900 deg/s): 0.71 ± 0.01 , Blue (1200 deg/s): 0.67 ± 0.01 .

3.3.4 *Selective activation of synaptic depression of thalamocortical synapse removes multi-timescale adaptive dynamics*

While having simultaneous access to thalamic and cortical activity during sensory stimulation provided a framework to monitor dynamical changes of thalamocortical synapse as well as spike timing within the local thalamic population, teasing apart the

relative contribution of each mechanism presents technical challenges because thalamic firing also affects the dynamics of the thalamocortical synapse. Hence, to determine the role of a single mechanism on cortical adaptation alone, we must factor out the contribution of other potentially interacting mechanism by setting the variable constant or unchanged. Using optogenetic method with selective Channelrhodopsin 2 (ChR2) expression in the VPM/VPL thalamus, we were able to directly recruit thalamic firing (and thalamic synchrony) therefore engaging synaptic depression of thalamocortical synapse with millisecond precision (Figure 3-7A).

To isolate the contribution of short-term synaptic depression of thalamocortical synapse on cortical activity over time, we interleaved 10-sec, light-evoked trials with 10-sec repetitive whisker stimulation and quantified thalamic and cortical responses during this manipulation. During light-evoked trials, thalamic firing was engaged rapidly, and the activity level remained relatively constant after initial activation for about 1.5 seconds (Figure 3-7B). This was evidently showed when we observed no significant difference in mean evoked firing rate (Figure 3-7C, Left) and mean first-spike latency (Figure 3-7C, Right) when we compared across 1.5-sec and 10-sec adaptation conditions during light-evoked trials. Additionally, we found that thalamic synchrony was also held constant during this later phase of adaptation (Figure 3-7D, E) as we observed no significant change from 1.5-sec to 10-sec adapted condition during light-evoked trials. These results suggest that our manipulation was able to selectively engage thalamocortical synaptic depression while holding thalamic firing rate and synchrony constant during the later phase of the adaptation condition (1.5 to 10 sec period), creating a regime where we can estimate how

cortical activity was changed when synaptic depression of thalamocortical synapse was the only mechanism that was activated.

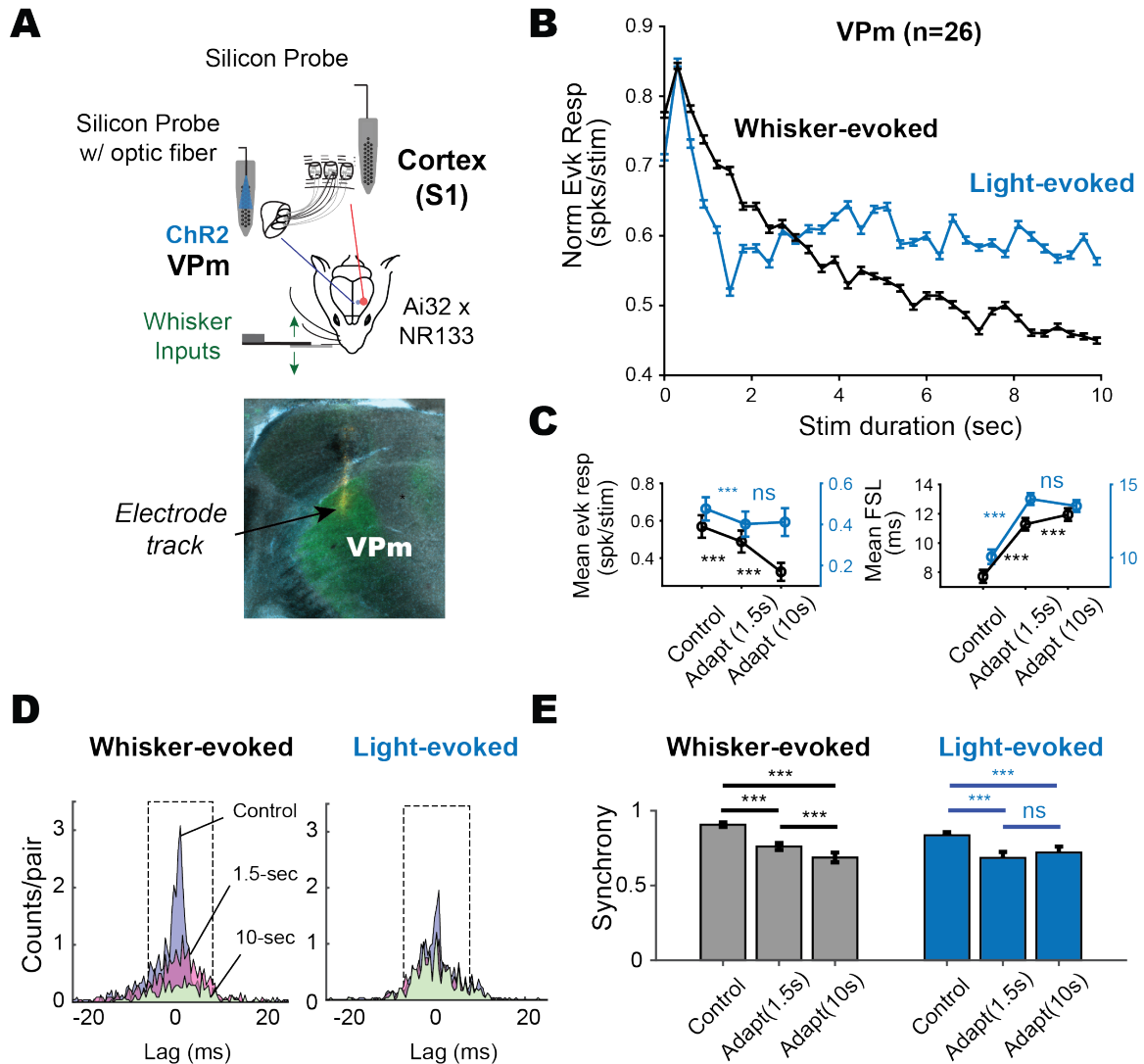


Figure 3-7. Optogenetic manipulation of short-term synaptic depression of thalamocortical synapse.

A. Schematic of experimental approach. Activating ChR2-expressing VPM thalamic neurons with 10 Hz repetitive light pulses to selectively engage synaptic depression of thalamocortical synapses while recording from thalamic and cortical activity. Bottom: histological section showed expression of ChR2 on VPM nuclei, overlaid with fluorescent

signal (DiI) recovered from electrode track. **B.** Adaptation of thalamic population ($N = 26$) during 10-sec repetitive whisker stimulation (shown in black) versus 10-sec repetitive optogenetic stimulation (shown in blue). Note the continuous reduction in whisker-evoked responses disappeared with light stimulation. **C.** Left: Mean evoked response of thalamic population ($N = 26$) across three stimulus conditions comparing whisker-evoked and light-evoked trials. Note that there is no significant changes in evoked firing rate comparing 1.5-sec versus 10-sec adaptation condition during light condition. Right: Mean first-spike latencies across three stimulus conditions. Note that there is no significant change in mean first-spike latency comparing 1.5-sec versus 10-sec adaptation. $***p < 0.0005$, $**0.0005 \leq p < 0.005$, paired sample t-test. **D.** Grand-averaged cross-correlograms of thalamic population comparing three stimulations condition for whisker vs light-evoked responses. Note that during light condition, synchronous firing. **E.** Significant reduction in thalamic synchrony across three stimulus conditions for whisker-evoked trials (related to Figure 3-6F). During light-evoked condition, thalamic synchrony dropped initially and remain unchanged from 1.5-sec to 10-sec condition.

Interestingly, we found that when thalamic firing and synchrony were controlled for and remained unchanged during the later phase of the adaptation, the multi-timescale adaptation dynamics in both FS and RS population were removed (showed qualitatively on Figure 3-8A, B). We found that reduction in response amplitude and increase in response latency were eradicated in both cortical FS (Figure 3-8C) and RS (Figure 3-8D) during light-evoked condition, suggesting that reduction in thalamic synchrony, combined with drop in thalamic firing rate are the major drivers that contribute to the adaptation dynamics of the later part of the repetitive stimulation.

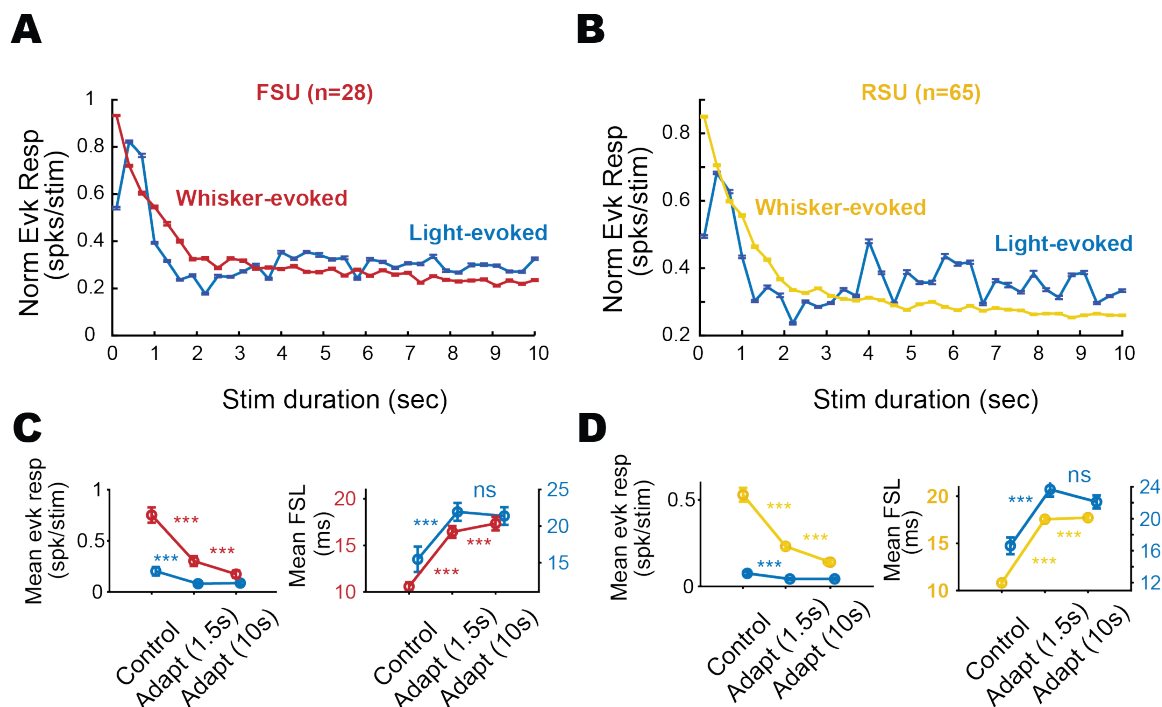


Figure 3-8. Contribution of short-term depression of thalamocortical synapse to cortical adaptation.

A. Adaptation profile for FS population (N = 28) during whisker-evoked (red) and light-evoked (blue) condition. **B.** Same as A but for RS population (N = 65). **C.** Left: Mean evoked response across three stimulus conditions comparing whisker and light-evoked condition for FS population (N = 28). There is no significant change comparing 1.5-sec and 10-sec adaptation condition. Right: Mean first-spike latencies across three stimulus conditions for FS population (N = 28). Note that there is no significant change in mean first-spike latencies comparing 1.5-sec and 10-sec adaptation condition during light-evoked trials. **D.** Same as C but for RS population (N = 65).

3.3.5 Adaptation over multiple timescales differentially modulates velocity tuning properties in the cortex

Previous studies of the vibrissa pathway have shown that adaptation as brief as 1-2 seconds is sufficient to reduce overall responsiveness of the thalamic and cortical population, shifting the neuronal responses towards an adaptive trade-off that favors sensory discrimination over detection (Ollerenshaw et al. 2014; Wang et al. 2010;

Whitmire et al. 2016). Here, our results corroborate these findings for short time scales, but show further effects of the adaptive dynamics at longer timescales (10-sec) (Figure 3-2, Figure 3-3). When we examined the cortical responses over the time course of repetitive stimulation using a classical signal detection framework, we found that adaptation in general pushed the distribution of evoked response (presence of signal) closer to the noise distribution over time (Figure 3-9A, B). The evoked spike count (signal) probability distributions were estimated from the observed cortical spike counts within a 30 ms post-stimulus window for a 300 deg/s stimulus, and the noise distributions were estimated from baseline activity 30 ms prior to stimulus onset. Shown in Figure 3-9A, B are examples of the corresponding signal and noise distributions for a typical cortical FSU and RSU, respectively. Specifically, for each S1 layer 4 FS and RS unit, we generated a spike count distribution by drawing samples ($n = 1000$ trials) from a ‘population’ distribution parameterized by the empirical across-trial mean (μ) and SD (σ). Plotted are the parametric fits of the empirical data (see Methods) using a Gamma(γ) distribution, $\Gamma(N*\alpha, \Theta)$, where $\alpha = \mu^2/\sigma^2$, $\Theta = \sigma^2/\mu$, and N is the assumed number of neurons within the population with similar response properties (Britten et al., 1992; Stuttgen and Schwarz, 2008; Wang et al., 2010, Wright et al., 2021). For the analyses presented here, we used an N value of 10. To predict the potential impact of adaptation on stimulus detectability, here we take the perspective of an ideal observer of the cortical spiking activity and ask to what extent we can detect the presence of a signal from background noise in the Non-Adapted and Adapted conditions (Figure 3-9C, top). Using the parametric distributions specified above (also see Methods), a sliding threshold was used to generate a Receiver Operator Characteristics (ROC) curve (Figure 3-9C, bottom), which shows the hit rate versus false alarm rate for an

ideal observer of the neuronal activity. ROC curves are shown for typical FS (Figure 6D, left) and RS (Figure 6E, left) neurons in S1 for the Control (solid), 1.5 sec adapted (dashed), and 10 sec adapted (dotted) cases. For both the FS and RS examples, the adaptation brought the ROC curve closer to the diagonal, reflective of a loss in detection performance. The area under the ROC curve (AUROC) was used as a performance metric for theoretical detectability, where an AUROC value of 1 corresponds to zero overlap between signal and noise distribution (an ideal detector) and an AUROC value of 0.5 corresponds to complete overlap between distributions, hence a random detector operating at chance. With increasing adaptation, we found that both FS and RS cells exhibit a significant decrease in detectability. For the FS neuron, the AUROC of the FS population across the Control, 1.5-sec adaptation, and 10-sec adaptation cases are shown in the right panel of Figure 3-9D, revealing a significant decrease in detectability with adaptation (AUROC for control: 0.94 ± 0.01 , 1.5-sec adapted: 0.93 ± 0.01 , 10-sec adapted: 0.82 ± 0.03 . Control versus 1.5-sec adapted: $p = 0.0418$, 1.5-sec versus 10-sec, $p = 8.73\text{e-}8$, Control versus 10-sec adapted: $p = 2.11\text{e-}6$). For the RS neuron, the corresponding summary statistics for the population are shown in the right panel of Figure 3-9E, also revealing a significant loss in detectability with adaptation (AUROC for control: 0.94 ± 0.02 , 1.5-sec adapted: 0.83 ± 0.03 , 10-sec adapted: 0.69 ± 0.04 . Control versus 1.5-sec adapted: $p = 0.0027$ 1.5-sec versus 10-sec, $p = 2.16\text{e-}4$, Control versus 10-sec adapted: $p = 8.09\text{e-}5$). Note that for both FS and RS population, ROC analysis demonstrated an overall degradation of detection performance from the Control to the 1.5-sec adaptation and continues to the 10-sec adaptation. Further, we found that the theoretical detectability is generally higher with FS spiking activity, despite a significant degradation of performance over the time course of adaptation. The

theoretical detectability of RS cells, on the other hand was impacted to a much greater extent with adaptation, as shown in population averaged detection performance (AUROC) in the right panel of Figure 3-9E.

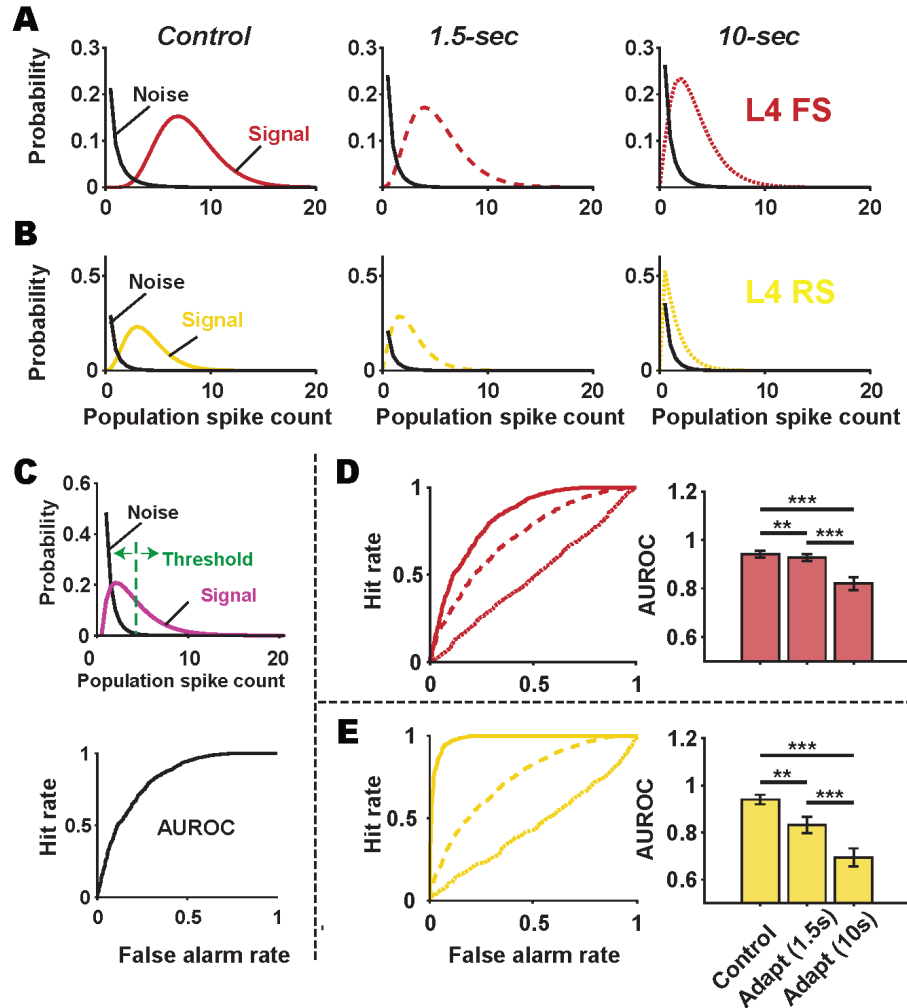


Figure 3-9. Adaptation degrades stimulus detection for ideal observer of cortical activity.

A. Population spike count distribution for noise (black) and signal (red) for FS cells in the Control (1st deflection), 1.5-sec adapted (15th deflection) and 10-sec adapted (100th deflection) condition. Plotted are the parametric fits using gamma distribution from FS population grand PSTH. Noise distributions were estimated from baseline activity 30 ms prior to stimulus onset. The evoked spike count (signal) probability distributions were estimated from the observed cortical spike counts within a 30 ms post-stimulus window for a 300 deg/s stimulus. **B.** Same as in A but for RS cells. **C.** Schematic depicting the computation of ROC analysis. Detectability was quantified as the area under the receiver

operator characteristic's curve (AUROC). **D.** Performance (AUROC) in the detection task comparing the Control (1st deflection), 1.5-sec adapted (15th deflection) and 10-sec adapted (100th deflection) condition. Shown on the left are an example ROC curve for a FS neuron in response to 300 deg/s stimulus and summary of the FS population on the right (N = 55). AUROC for control: 0.94 ± 0.01 , 1.5-sec adapted: 0.93 ± 0.01 , 10-sec adapted: 0.82 ± 0.03 . Note that detection performance was degraded over the time course and a drastic reduction from 1.5-sec to 10-sec adaptation condition. Control versus 1.5-sec adapted: $p = 0.0418$, 1.5-sec versus 10-sec, $p = 8.73e-8$, Control versus 10-sec adapted: $p = 2.11e-6$. *** $p < 0.0005$, ** $0.0005 \leq p < 0.005$, Wilcoxon signed-rank test. **E.** Same as D but for RS cells (N=25). AUROC for control: 0.94 ± 0.02 , 1.5-sec adapted: 0.83 ± 0.03 , 10-sec adapted: 0.69 ± 0.04 . Control versus 1.5-sec adapted: $p = 0.0027$ 1.5-sec versus 10-sec, $p = 2.16e-4$, Control versus 10-sec adapted: $p = 8.09e-5$. *** $p < 0.0005$, ** $0.0005 \leq p < 0.005$, Wilcoxon signed-rank test.

To evaluate the functional consequences of the adaptation on stimulus discrimination across multiple timescales, we quantified the velocity tuning properties in the thalamus and cortex using six different velocities (schematic shown in Figure 3-10A, velocities (s1-s6): 125, 300, 450, 600, 900, 1200 deg/s). To investigate the effects of 1.5-sec adaptation versus the 10-sec adaptation, we presented two type of adaptation trials with distinct stimulus duration (1.5 sec and 10 sec correspondingly, at 300 deg/s, presented with 10 Hz frequency), and then followed by probe stimuli of different velocities (s1-s6) as the last pulse of deflections. We observed that adaptation generally attenuated the response magnitude, reducing the velocity sensitivity for most velocities for the FS population (Figure 3-10B, n = 55) and all velocities for the RS population (Figure 3-10C, n = 25). Taking the perspective of an ideal observer, we examined to what extent adaptation over these different timescales affect discrimination between different sensory inputs (whisker deflections at different velocities). Shown in Figure 3-11A and B are parametric fits of the experimentally observed distributions for the FS and RS populations, respectively. Qualitatively, we observed that population spike counts were relatively high in the control conditions and the distributions were highly overlapped and unordered. However, 1.5-sec

adaptation attenuated the population spikes counts and the distributions become more separated and ordered, as shown in the FS population tuning curves. This effect is even more prominent for the 10-sec adaptation, as shown in the right most panel of Figure 3-11A. For the RS population, we observed a general reduction in response amplitude for all velocities, and specifically adaptation further shifted the 300 deg/s distribution to the left and potentially separated it from the rest the velocity distributions (Figure 3-11B). To quantify this effect, we compared the performance of the ideal observer in discriminating between different deflection velocities under Control, 1.5-sec and 10-sec adapted conditions. Figure 3-11C shows a schematic of how the performance matrix was constructed to compare the separability of the different velocity distributions. The performance matrix displays the probability of inferring a particular velocity given the actual velocity presented. The overall discrimination performance is a metric that reflects the accuracy of the ideal observer versus correct stimulus classifications. For the experimentally measured FS and RS distributions, we found a significant increase in discrimination performance for both the 1.5-sec and the 10-sec adapted conditions, as compared to control for FS population but only 10-sec adapted conditions for RS population (Figure 3-11D). We suspected that our quantification for RS population is lacking sufficient sample size. However, in general, our data suggest that adaptation over multiple timescales potentially facilitate better discrimination performance by reducing the overlap between stimulus distributions, and as a tradeoff, reducing the overall sensitivity to repetitive stimulation.

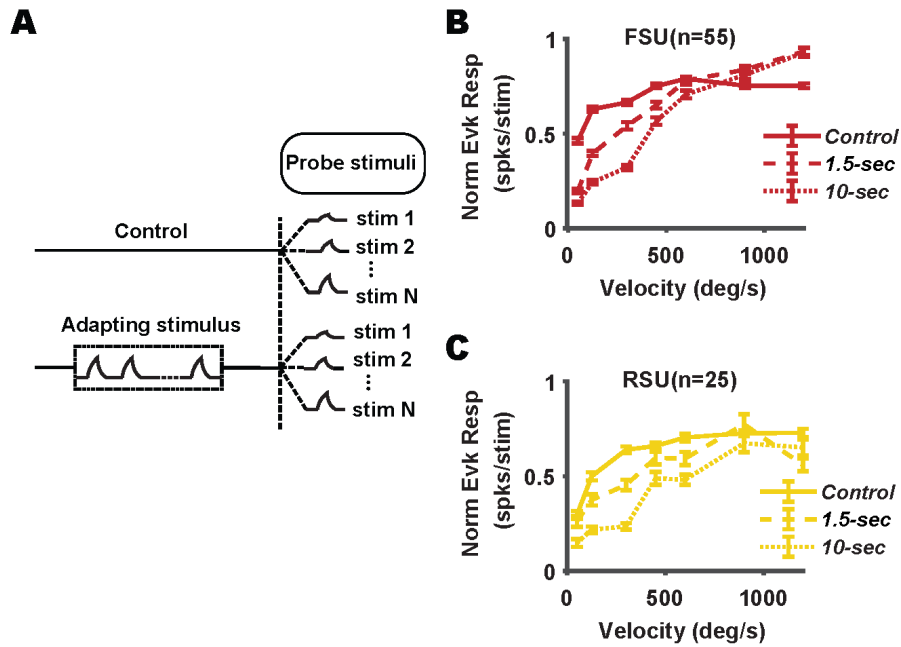


Figure 3-10 Adaptation modulates velocity sensitivity of cortical population.

A. Schematic shows the experimental design for probing the neuronal response to different stimulus velocities, either in the presence or absence of preceding adapting stimulus. **B.** The velocity tuning properties for FS population ($N = 55$) during Control (preceded by no stimulus), 1.5-sec adapted (preceded by 15th deflection) and 10-sec adapted (preceded by 100th deflection) conditions. **C.** Same as B but for RS population ($N = 25$).

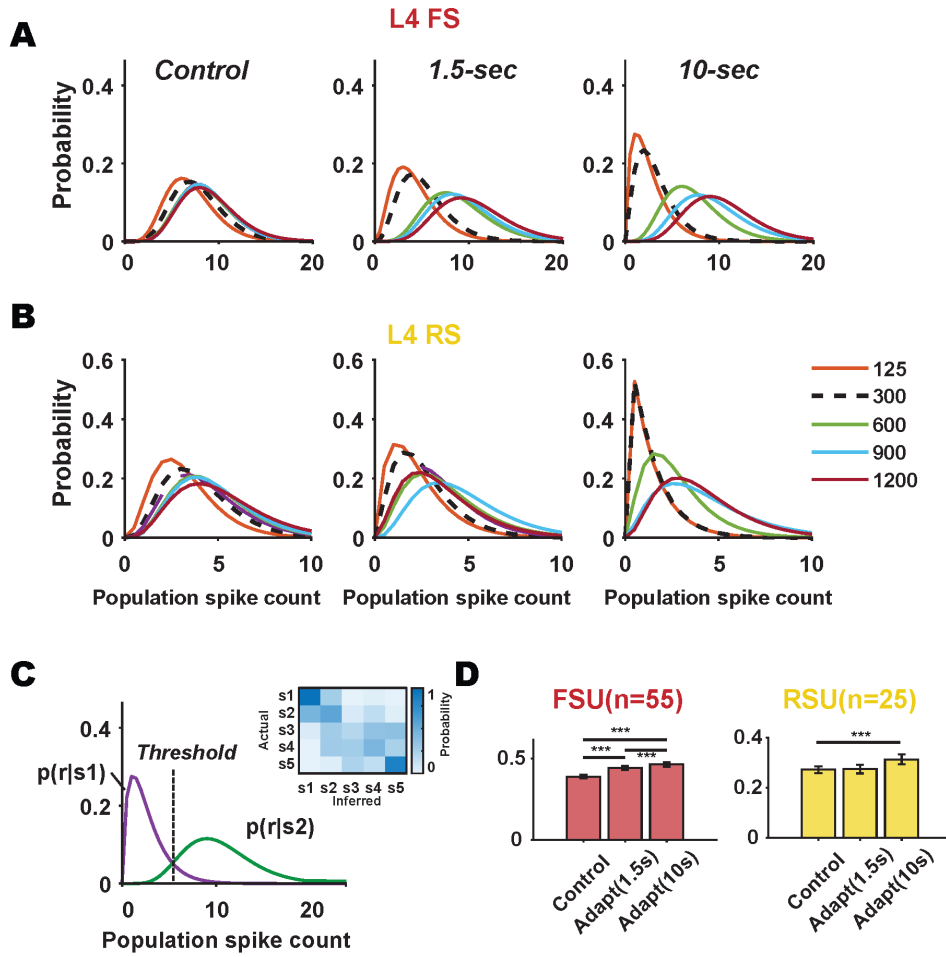


Figure 3-11. Adaptation enhances stimulus discrimination for ideal observer of cortical activity.

A. Parametric distribution of FS population, fitted using Grand PSTHs of cortical neurons ($N = 55$), comparing Control, 1.5-sec adapted and 10-sec adapted conditions. **B.** Same as **A** but for RS population ($N = 25$). **C.** Schematic for theoretical discriminability of different stimulus distributions using performance matrix. **D.** Discrimination performance for FS and RS population. Performance for FS: control: 0.39 ± 0.01 , 1.5-sec adapted: 0.44 ± 0.01 , 10-sec adapted: 0.46 ± 0.01 . Control versus 1.5-sec adapted: $p = 5.48e-5$, 1.5-sec versus 10-sec, $p = 0.0019$, Control versus 10-sec adapted: $9.4e-8$. $***p < 0.0005$, $**0.0005 \leq p < 0.005$, Wilcoxon signed-rank test. Performance for RS: control: 0.27 ± 0.01 , 1.5-sec adapted: 0.28 ± 0.01 , 10-sec adapted: 0.31 ± 0.02 . , Control versus 10-sec adapted: 0.003

3.4 Discussion

The rodent somatosensory pathway is a model system that has been widely utilized to investigate changes in coding strategy and adaptation due to its well-studied anatomical architecture and the convergent nature of thalamocortical projections. Here, we examined how the time course of repetitive stimulation affects the adaptive dynamics in the thalamocortical circuit and found that the adaptive changes in responsiveness to individual whisker deflections over time exhibited dynamics across multiple timescales. This, along with other studies that have shown multiple timescales of adaptation with various duration of repetitive stimulation (Dragoi et al. 2000; Latimer et al. 2019; Patterson et al. 2013), white noise stimulus (Fairhall et al. 2000) and modeling approaches (Latimer and Fairhall 2020) further points to the evidence of brain's mechanisms to cope with changes across distinct timescales. We assessed neuronal firing activity in the thalamocortical circuit in response to repetitive stimulation across the specific timeframe of 10 seconds, for which the pathway exhibited two distinct timescales of dynamics: the first, a rapid transient adaptation in the first 1.5 seconds, and the second, a slower, longer duration adaptation over approximately 10 seconds. Here, the ability to record simultaneously from the thalamic VPM population as well as both the cortical L4 FS and RS populations allowed us to examine the effects of adaptation on spiking response amplitudes, spike timing, as well as neuronal mechanism such as population synchrony and synaptic mechanisms across the thalamocortical junction. While multi-time-scale dynamics have been reported at the level of single-ion channels (Gilboa et al. 2005), at the synaptic level in studies of short-term synaptic plasticity (Zucker and Regehr 2002), and also at the neuronal level (Latimer et al. 2019), we demonstrate here that adaptation across multiple timescales is potentially

a consequence of the interaction between distinct mechanisms, as opposed to associating a specific mechanism with a particular timescale.

To elucidate the differential adaptation across thalamus and cortex, numerous studies have identified potential mechanisms that could underlie this phenomenon. The major identified drivers of rapid cortical sensory adaptation include 1) cellular mechanisms, such as intrinsic properties of cortical neurons, 2) synaptic mechanisms that involve depression of thalamocortical (TC) and intracortical (IC) synapses, and 3) neuronal population mechanisms such as thalamic population synchrony, as well as intracortical balance of excitation and inhibition (E-I balance). One prominent view is that short-term depression of thalamocortical synapses plays a dominant role in this type of cortical adaptation (Castro-Alamancos 2004b; Chung et al. 2002; Katz et al. 2006). This was experimentally demonstrated using selective depression of TC and IC synapses via electrical stimulation in simultaneous, paired extracellular recordings under anesthesia. However, the rapid synaptic depression of the TC synapse reported in Chung et al. (2002) did not rule out the contribution of thalamic population synchrony to S1 adaptation. In fact, many lines of evidence have pointed to the role of thalamic spike timing and synchrony in S1 processing either under anesthesia (Pinto et al. 2000; Wang et al. 2010; Whitmire et al. 2016) or wakefulness (Wright et al. 2021b). Additionally, the adaptive shift in excitation-inhibition (E-I) balance in the cortex has also been explored extensively. The more profound depression of intracortical inhibitory synapses as compared to excitatory synapses during persistent stimulation has been shown to skew the E-I balance towards excitation (Gabernet et al. 2005b; Heiss et al. 2008). This reduction in feedforward inhibition was shown to expand the cortical window of integration and likely to affect how inputs are summed

across multiple timescales of adaptation. In this study, the evidence suggests that synaptic depression of the TC synapse (Figure 3-4), along with an adaptive reduction in thalamic synchrony (Figure 3-5), both likely contribute to the adaptation at a fast timescale (0-1.5 seconds). However, the monotonic desynchronization of the thalamic population (2-10 seconds) beyond the first few seconds could play a more dominant role in modulating cortical adaptation at a longer timescale. These results together suggest the possibility of a complex interaction between distinct mechanisms, and that multiple mechanisms can be co-activated over distinct periods of time to contribute to the cellular dynamics that we observed.

Given the nature of how single empirical phenomena often arise from multiple contributing biophysical mechanisms, studying adaptation across multiple timescales is not without its challenges. In this study, we were able to capture multiple timescales of adaptation using a 10 Hz repetitive stimulation over 10 seconds. It is important to note, however, that adaptation is a change in function that takes time to develop and also dissipate. It has been shown that the temporal scales over which adaptive dynamics build up and recover are distinct, and also highly dependent upon the duration of exposure to repetitive stimulation (Chung et al. 2002; Dragoi et al. 2000; Patterson et al. 2013). In general, brief exposure produces adaptation that develops and recovers rapidly (Nelson 1991a, Bonds 1991, Müller et al. 1999), while more prolonged stimulation can result in slower and more lasting forms of changes (Greenlee et al., 1991). Additionally, thalamic and cortical neurons also exhibit diverse timescales of responsiveness to repeated stimulation (Chung et al. 2019). Therefore, as a rule of thumb, an inter-trial interval of at least 4 times the duration of adapting stimulus train (10 seconds) was utilized in this study,

while acquiring at least 100 trials of repeated measurements of the adaptation dynamics. As a control, we also assessed the difference between the magnitude of the response to the first deflection of the adapting train at the beginning and end of a stimulus block. We did not observe a significant difference in this measure (data not shown), suggesting that the majority of the neurons returned to the baseline condition prior to the initiation of the next trial, although longitudinal effects cannot be completely ruled out. For a subset of the data, we also probed the recovery for each thalamic and cortical neuron and found that most of the cells showed a full recovery to the baseline condition (data not shown).

Given that this study was performed in the somatosensory pathway of the isoflurane-anesthetized rodents, it is important to acknowledge some of the limitations in the findings. The large majority of studies of the role of short-term depression of thalamocortical and intracortical synapses have been conducted under anesthesia (Chung et al. 2002; Heiss et al. 2008). On the other hand, the adaptive changes in synchronous thalamic firing have recently been reported to play a more prominent role than synaptic depression in the TC and IC synapse under wakefulness (Wright et al. 2021a). One possibility is that the overlap between distinct mechanisms during wakefulness is smaller compared to the condition under anesthesia. It was reported that the thalamocortical circuit may be in an elevated baseline firing state during wakefulness (Castro-Alamancos 2004a), hence this suggests that TC synapses might already be adapted. Our findings here suggest the possibility that when the cell is at its baseline condition, it may first engage the synaptic mechanism, causing synaptic depression. At the same time, the TC circuit may engage neuronal mechanism such as desynchronization of firing activity within the thalamic population in a distinct but overlapping timescales. Hence, when synaptic depression is fully engaged,

thalamic desynchronization may dominate and exert a greater effect on regulating the nature of information conveyed downstream to cortical targets.

Finally, the results here suggest that although multiple mechanisms may interact and transition dynamically at various timescales, adaptation over the time course that we examined in this study improve theoretical discrimination at the expense of detection. This similarity in function supports the possibility of a unifying framework across disparate mechanisms and timescales, which is to allow the brain to maintain a flexible representation in response to stimulus statistics that span a wide range in our natural environment. Moreover, these results further support Barlow's efficient coding hypothesis such that the reduction in responsiveness of neuronal response in the TC circuit is not a negative attribute that signifies a loss of sensitivity to stimuli, but merely a mechanism that mediate an adaptive trade-off in coding strategy to put the brain (in this case the primary sensory cortex) in a state that optimizes neural coding efficiency.

CHAPTER 4. CONCLUSIONS AND FUTURE DIRECTIONS

4.1 Overview of thesis result

To summarize, this thesis work has two primary contributions. First, we established advanced techniques to perform simultaneous, multi-electrode recordings of neuronal population in the rodent thalamocortical circuit. This work produced a novel statistical approach for inferring synaptic connectivity across the brain regions. Specifically, we developed a signal-detection based classification of synaptic connectivity of simultaneously recorded neurons in the thalamus and S1 cortex. This framework provides an assessment of classification confidence that is highly applicable to the large-scale recording approaches that are emerging in the field. Importantly, we developed tools that track signaling across brain structures and laid out a framework that examines causal flow of information transmission in early sensory processing.

In the second part of the thesis, we investigated the neural mechanisms that underlie an important sensory phenomenon that emerges in this early sensory circuit: rapid sensory adaptation. While this phenomenon has been well-studied over very rapid timescales of hundreds of milliseconds, the neural mechanisms underlying adaptation over longer time scales (such as the regime that span 10's of seconds) remain underexplored. Here, utilizing the previously developed methodology (Chapter 2), we demonstrated that the thalamus and the thalamorecipient layer 4 excitatory and inhibitory neurons in S1 exhibit differential adaptation dynamics, and that the neuronal dynamics across these different regions and cell types show common signatures of multiple timescales in response to sensory adaptation.

With this in mind, what follows is a discussion of the key results, limitations of the current approach, as well as some ideas for future work.

4.1.1 Key conditions for synaptic connectivity inference

Despite many novel and emerging tools in electrophysiology, identification of functional connections in an intact brain remains a challenging endeavor. Specifically, it is a multi-step process that requires extensive experimental preparation and an optimized stimulus paradigm to warrant a successful recording. These multi-condition constraints include targeting regions that share overlapping receptive fields (i.e. respond to the same primary whisker in our study (Alonso et al. 2001)), having simultaneous access to neuronal activity of both regions with single-cell resolution, and gathering a minimum amount of spiking or subthreshold activities for evaluating the effect of presynaptic spiking on postsynaptic activity (Bruno and Sakmann 2006; Wang et al. 2010). The first and second constraints are experimentally-related, therefore we have laid out a work-flow to address these challenges that is potentially applicable to other sensory modalities. The third constraint is a more difficult problem to solve because it involves making an inference given some information about the spiking activity of two parallel spike trains. Here we narrow our discussion to solving this problem with pairs of neuronal spike trains recorded from brain regions with limited information about the exact anatomy. For instance, we recorded from pairs of neurons from the topographically aligned VPM and S1 regions where the feedforward VPM projections to S1 layer 4 were known to be numerous. However, the exact connectivity can only be estimated based on statistical evaluation, which is often data intensive. As mentioned before, previous studies have used electrical

stimulation to conduct collision tests that involve comparing the timing of anti-dromic activation with stimulus evoked activity to verify origins of projection (Kathleen Kelly 2001; Swadlow 1989). Although this is a powerful and attractive approach, as it helps to more confidently assess connectivity and establish causal relationships, it does not scale well to assessing connectivity at the population level, where selective stimulation of individual neurons is not typically possible. Previous studies have also met the third constraint by collecting spontaneous activity for an extended period of time (Swadlow 2003; Swadlow and Gusev 2001), however this is time-consuming, and the amount of data required for statistical inference remains arbitrary. Alternatively, some studies utilized weak, desynchronizing stimuli to elevate the firing rate across the brain regions (Bruno and Sakmann 2006; Wang et al. 2010). However, to our knowledge there has been no study prior to this that systematically tested the relationship between stimulus parameters and connectivity inference. As we systematically explored the data-length effect on the connectivity inference, we discovered another challenge that resembles a ‘Catch-22’, where stimulus-evoked activity could compromise the connectivity inference by producing correlated neural activity. Therefore, to fill this gap in knowledge, we have methodically explored the trade-off between network activity levels needed for the data-driven inference and likelihood of misclassification of connectivity as a function of the synchronization of the presynaptic population. Our results showed while the amount of spiking was a strong determinant of the accuracy of the inference of connectivity, synchronous spiking across the neuronal pair could result in both Type 1 (false alarm) and Type 2 (miss) errors, thus playing an important role in experimental design.

4.1.2 Multiple timescales of adaptation in the TC circuit

Extensive work has been done to study sensory adaptation because of its perceptual and behavioral relevance. Short-term adaptation that typically manifests in reduced response amplitudes after repeated stimulation had been documented at subcortical and cortical levels (Ahissar et al. 2000a; Bruno and Simons 2002; Chung et al. 2002; Khatri et al. 2009; Khatri et al. 2004; Ollerenshaw et al. 2014; Pinto et al. 2000; Simons and Carvell 1989; Wang et al. 2010). Importantly, differential adaptation effects that were observed across the thalamus and cortex suggest complex interaction between these brain structures. Mechanisms that are thalamic in origin and recurrent interactions at the level of the cortical network are both thought to be candidates that underlie adaptation at the short timescales (Castro - Alamancos and Oldford 2002; Chung et al. 2002; Gabernet et al. 2005b; Malina et al. 2013), however the role of TC synaptic depression on S1 adaptation has been widely accepted as the major underlying mechanism. Recent work under wakefulness, on the other hand, suggests that adaptive changes in thalamic spiking synchrony, in addition to robust engagement of feedforward cortical inhibition, also plays an important role in mediating rapid adaptation in mouse barrel cortex (Wang et al. 2010; Wright et al. 2021a). While adaptation across mechanisms and timescales has been proposed as a unifying theoretical framework that may integrate numerous disparate experimental observations (Drew and Abbott 2006), the large majority of studies of sensory adaptation focus on a single timescale (Chung et al. 2002; Khatri et al. 2004; Kheradpezhohu et al. 2017; Patterson et al. 2013), likely targeting one specific mechanism. What is not well understood is the interaction between the mechanisms of adaptation across different timescales that would be relevant in ethological contexts. To fill this gap, our goal was to find commonalities in these mechanisms across different timescales and determine the functional relationships

with each other. Our results clearly showed evidence of at least two timescales in the adaptation dynamics that exhibited differential functional properties across the thalamocortical circuit, affecting both the response magnitude and spike timing. Our results suggest that thalamic synchrony potentially plays a more prominent role in the second, longer timescale over 5-10 seconds, whereas short-term synaptic depression, as measured through identified monosynaptically connected pairs and optogenetic manipulation of the thalamocortical circuit, contributes more in the first, short timescale over the first few hundreds of milliseconds.

4.1.3 Functional consequences of adaptation on detection and discrimination

Previous work in the lab has shown strong evidence that thalamic spike-timing can have fairly dramatic effects on the downstream cortical representation (Borden et al. 2022; Wang et al. 2010; Wright et al. 2021a) and behavioral performance (Ollerenshaw et al. 2014), mediating an adaptive trade-off between detectability and discriminability. In this work, we seek to determine if multiple timescales of adaptation also contribute this trade-off in representation that could ultimately have profound behavioral consequences. Indeed, in Chapter 3, when we quantified the velocity tuning curves and the theoretical detectability and discriminability using ideal observer of cortical activity over 10-sec repetitive stimulation, we found that it further improved discrimination performance between different velocities of whisker stimulation at the expense of detectability, pointing to additional adaptive changes beyond a single, short timescale that has been extensively studied. In our experiments, the multiple timescales of adaptation are more clearly shown in the FS than RS population; this kind of differential effect could have profound impact

on Excitatory-Inhibitory (E/I) balance in cortex, which has been shown to play a critical role in shaping the selectivity of cortex to sensory inputs. The similarity in adaptation function across timescales further supports the possibility of a unifying framework across disparate mechanisms and timescales, which is to allow the brain to maintain a flexible representation in response to stimulus statistics that span a wide range in our natural environment.

4.2 Limitations

While the experimental technique and methodology used in these studies was designed specifically to track neuronal dynamics across brain structures (Chapter 2) and monitor changes of neural coding over time (Chapter 3), there were several caveats or concerns that should be outlined here for future reference.

4.2.1 Stimulus paradigm limitations

4.2.1.1 Anesthetized Recordings

Though the work here was designed to ultimately explore the role of the thalamocortical circuit in the context of behavior, most of the investigation was done under anesthesia. This was a practical and logical experimental decision because, in Chapter 2, our goals were to optimize the experimental techniques and stimulus parameters to record from topographically aligned regions in the TC circuit and to identify monosynaptic connection across those brain regions, where we needed robust control of experimental conditions. Although there are obvious differences in activity and the function of this circuit in the anesthetized versus non-anesthetized conditions, the statistical framework and

dependence on data we believe to be independent of these differences. We believe that the experiments conducted here represent a critical step for extending this approach to awake, behaving conditions (see Future Directions).

4.2.1.2 Whisker stimulation paradigm

In this study, we used a single, passive whisker stimulation paradigm to probe the circuitry, which has its own limitation. Given that the mice often actively move their entire whisker pad in synchronization to sweep across any surface, it is unlikely for a single whisker to be stimulated in isolation. Although studying neural responses to naturalistic stimuli is incredibly important for learning about the evolved function of the sensory system in question, in these studies the precisely controlled activation the circuit through single whisker deflections was critical in developing the framework for targeting topographically aligned circuits and establishing monosynaptic connectivity across multiple brain regions. However, I believe that this work can be expanded into more complex, ethological sensory paradigms to examine the effects of adaptation over multiple timescales on cross-whisker adaptation in the future.

4.2.2 *Large-scale surveying of neuronal dynamics over time*

The advent of recording technologies has enabled large-scale monitoring of neuronal ensemble, opening up a greater avenue for studying brain function, especially when causal relationships can be identified across brain regions. These modern measurement techniques also introduce less sampling bias as compared to traditional, “neuron at a time” single-unit extracellular recording, hence allowing examination of a greater diversity of the cell population. Additionally, the yield per experiment is much

higher, with comparable single-unit quality to single-units obtained from single electrode extracellular recordings, providing ample sampling of the neuronal population. However, as mentioned in the Chapter 2 Discussion, the data that we obtained are of greater variability and exhibit a much greater diversity in waveform signal-to-noise ratio (SNR) as compared to traditional techniques. Additionally, with high-channel count introduces complexity of analysis at all levels. Spike sorting has always been a technical challenge to faithfully isolate individual neurons and separate activity across simultaneously recorded neurons within the neuronal population, especially with large datasets. It involves a subjective process that requires manual curation of the dataset to improve the spike classification. This is much more complex than the traditional single-cell electrophysiology. However, this issue can potentially be alleviated with more training, and adopting approaches such as a double-blinded curation process, as well as ensuring trends in data are sampled from different and sufficiently large numbers of recording sessions and animals.

4.2.3 Tracking of synaptic transmission using extracellular spiking

In this work, one of our main goals was to establish the presence of monosynaptic connectivity across the TC structures. The gold standard of studying and assessing synaptic connectivity involves direct manipulation of pre-synaptic neurons to observe a measurable postsynaptic effect. Hence, connectivity studies are often performed using intracellular recordings (Jouhanneau et al. 2015; Jouhanneau et al. 2018; Pala and Petersen 2015). However, intracellular recording in deep structures such as the thalamus is incredibly challenging technically (Stoy et al. 2017) and any combination of paired recording that

involves intracellular recording adds another layer of complexity to the experiments. Furthermore, intracellular approaches are ultimately limited to a very small number of neurons and do not scale to the circuit level. Extracellular recordings offer solutions to some of these issues, and thus offer promise in this direction. Despite losing the resolution of subthreshold and suprathreshold activity from a single cell, we gain more information about network signaling with large-scale, extracellular recording. In our work, we confronted the diversity in data quality that the large-scale recording introduces and developed a statistical approach for signal-detection based inference of connectivity, which provided an assessment of classification confidence that we believe can be used to compare across disparate datasets and findings in the field.

4.3 Speculations of findings & future directions

4.3.1 Decoupling thalamocortical interactions across timescales

4.3.1.1 Isolating thalamic contributions from recurrent cortical network

Previous work by Chung et al. (2002) used electrical stimulation in VPM and S1 to compare the relative contributions of thalamocortical (TC) and intracortical (IC) synapses on S1 adaptation, involving non-specific circuit activation and potentially synchronized neuronal activity far beyond the site of stimulation (Millard et al. 2015). The advent of optogenetic tools, however, provides selective activation of specific cell-type in a reversible, temporally precise manner. In Chapter 3, we utilized a transgenic mouse line (Ai32xNR133) with selective expression of Channelrhodopsin 2 (ChR2) in the VPM/VPL thalamus to specifically engage thalamocortical (TC) synaptic depression by stimulating the cell bodies of VPM neurons, bypassing sensory adaptation dynamics cascaded from the

periphery. In this manipulation, we were able to control for thalamic firing rate and synchrony, holding both constant at the longer timescales (1.5 – 10 seconds) while depressing the thalamocortical synapse. This causal manipulation allowed us to tease apart the role of two thalamic-dependent mechanisms (i.e., synaptic depression and thalamic synchrony) that are usually coupled within the timescales that we have explored in this work. In future work, a different transgenic mouse line could be used that specifically targets the recurrent network in S1 to study transformation at the level of cortex. Previous work in this direction has shown that selectively activating cortical inhibitory interneurons using Parvalbumin (PV)-expressing mouse lines can silence recurrent excitatory circuits in the cortex, isolating feedforward thalamic excitation only in layer 4 cortical cells (Li et al. 2013; Lien and Scanziani 2013; Reinhold et al. 2015). This is a particularly important circuit to study and a natural extension of this work because the recurrent circuits in the cortical network likely affect how each cortical neuron integrates and transforms sensory input in time, particularly after the first several tens of milliseconds (thalamic contributions drop to less than 50% and marked increase of cortical amplifications after about 40 ms from stimulus onset) (Reinhold et al. 2015).

4.3.1.2 Corticothalamic interactions and sensory adaptation

In this work, we focused specifically on the feedforward sensory processing in the thalamocortical circuit. However, increasing evidence indicates that corticothalamic feedback also plays a crucial role in modulating thalamic sensory response (Alitto and Usrey 2003; Briggs and Usrey 2009; Crandall et al. 2015; Happel et al. 2022), suggesting a complex dynamic interaction between the feedforward and feedback pathways. It was

previously found that corticothalamic (CT) feedback accounts for 30-44% of projections to the sensory thalamus and CT axons outnumbered TC axons by about 10:1 (Erişir et al. 1997a; Erişir et al. 1997b; Guillery 1969; Liu et al. 1995; Van Horn et al. 2000). Despite the massive input to the thalamus, an understanding of the impact of L6 CT neurons on sensory processing remains elusive. This is primarily because corticothalamic neurons show diverse spiking patterns and the modulatory effect of L6 CT cells to the thalamus is bidirectional (suppressive or enhancing) and potentially state dependent (Dash et al. 2022). Advances in optogenetic tools and Ntsr1-Cre mouse line (Gong et al. 2007) have helped alleviate the challenges of selectively manipulating CT activity in a temporally precise manner. One study that is directly relevant to this work showed that activation of L6 CT cells under anaesthesia decreases adaptation in the VPM neurons in response to 8-Hz whisker deflection in the short (~ 1 s) timescale (Mease et al. 2014), suggesting that L6 CT neurons can strategically alter thalamocortical transformations during sensory adaptation. Work from the visual and somatosensory pathways also showed that the net facilitative or suppression effect of L6 CT activation on thalamic targets is frequency dependent and this is potentially due to state-dependent engagement of distinct synaptic and neural mechanisms of thalamocortical synapses of first order and higher order thalamic nuclei (Crandall et al. 2015; Kirchgeßner et al. 2020). Techniques developed in Chapter 2 to target connectivity could be extended to studying connectivity of corticothalamic feedback and to expand what we found in Chapter 3. I further envision studying the role of L6 CT neurons using the adaptation paradigm explored in this work and potentially during wakefulness. This presents an opportunity to investigate how feedback projections directly affect thalamocortical transformations, and perhaps shed new insights on how L6 CT

neurons can change thalamic and cortical sensitivity to bottom-up sensory processing. I would predict that L6 CT neurons might play a critical role in dynamically shifting the engagement of different mechanisms underlying sensory adaptation across timescales, given the numerous feedback projections to multiple thalamic targets, and potentially mediate both short and long-term changes in the thalamocortical circuitry by changing the sensitivity and selectivity of thalamocortical neurons to different stimulus features.

4.3.2 Extension of findings to awake conditions

4.3.2.1 Synaptic connectivity under wakefulness

As mentioned, we envision broad applicability of the experimental and computational approaches for inferring monosynaptic connectivity in awake, paired recordings conditions. However, as discussed in the Chapter 2 Discussion, one has to pinpoint the optimal experimental conditions for awake rodents. Specifically, the relationship between mean firing rate and thalamic synchrony must be determined in this context. It was known that the baseline firing rate for both thalamic and cortical neurons is higher under wakefulness (Crochet and Petersen 2006; Urbain et al. 2015). However, it is unclear if thalamic synchrony also increases monotonically with the mean firing rate when the animal is awake and behaving.

Additionally, the effect of whisking will likely affect the relationship between stimulus strength and measured synchrony explored in this study, potentially confounding the monosynaptic connectivity inference. However, given the techniques and experimental parameters explored in this study, we believe this we have at a minimum, laid the foundation for capturing connectivity during wakefulness. Ideally, a non-synchronizing

stimulus (sensory or optical) should be used to elevate the mean firing rate across the aligned thalamocortical brain regions, while whisker videography should be in place to record whisker movement. Given that the effects of whisking on thalamic synchrony are unclear and could increase trial-to-trial variability, epochs of whisking should likely be excluded from the analysis for monosynaptic connectivity inference.

Separately, optogenetic tools for identifying functional connectivity are gaining traction as genetic tools for targeting specific cell types in mice are rapidly growing. However, optogenetic tools alone are not sufficient for connectivity studies, as control experiments or additional constructs (pharmacology intervention) are still required to distinguish between monosynaptic versus polysynaptic light-evoked responses in the target population, primarily when optogenetic stimulation of long-range projections is used (Lee et al. 2020). One possibility is to use optogenetic tools in addition to the experimental and analytical framework that we have developed here. Specifically, I envision that optogenetic tools combined with transgenic mouse lines can be used effectively to examine synaptic efficacy in connected pairs. For example, using a transgenic mouse line (Ai32xNR133) that restricts expression of Channelrhodopsin 2 (ChR2) to VPM/VPL thalamus, it was reported that step input of illumination can elevate firing activity of thalamic neurons without causing synchronization (Wright et al. 2021a), potentially providing an optimal firing regime that would minimize false classification and accelerate the data collection process.

Lastly, chronic implantation of probes can be a good resort for studying functional connectivity during wakefulness. Okun et al. (2016) showed stable V1 recordings over

several months after probe implantation. Combined with the experimental approach for targeting the topographically aligned regions specified here, chronic implantation of silicon probes in either or both of the regions of interest could drastically reduce the preparation for identifying synaptic connectivity. Additionally, this approach produces an invaluable dataset for longitudinal studies that are critical for animal learning and behavior. However, note that this described procedure is not without its challenge because probe implantation often causes inflammation and tissue scarring. However, the advancement of neural electrodes or probe technology is rapidly accelerating, with better materials and techniques continually being discovered in the field (Lu et al. 2019), potentially providing a viable solution in the near future.

4.3.3 Results that are generalizable to larger context

Thalamocortical transformations and sensory adaptation across timescales are both ubiquitous features that are conserved across most sensory modalities. Thus, the knowledge gap filled by this work may be extended easily to other pathways and ethologically relevant contexts. For instance, work by Latimer et al. (2019) has demonstrated that adaptive responses in the somatosensory, visual and auditory cortex generally exhibit similar signatures of systematic reduction in response amplitude and frequency-dependent modulation when a common pulsatile stimulus set was used. Interestingly, this particular study has also shown that these adaptive responses can emerge when modeled with filters encompassing multiple timescales. This suggests that our findings in this work are likely to generalize across the thalamocortical circuit of other sensory pathways.

In a broader perspective, the repetitive stimulation used in this study is somewhat similar to the acute stimulation used in rehabilitation medicine to promote recovery in stroke patients (Saito et al. 2018). Although the persistent stimulation that was used in rehabilitation spanned a much longer timescale (minutes to hours), this work has laid the foundation for bridging the mechanistic understanding of changes in neural representations across distinct stages of the early sensory pathway as well as different timescales.

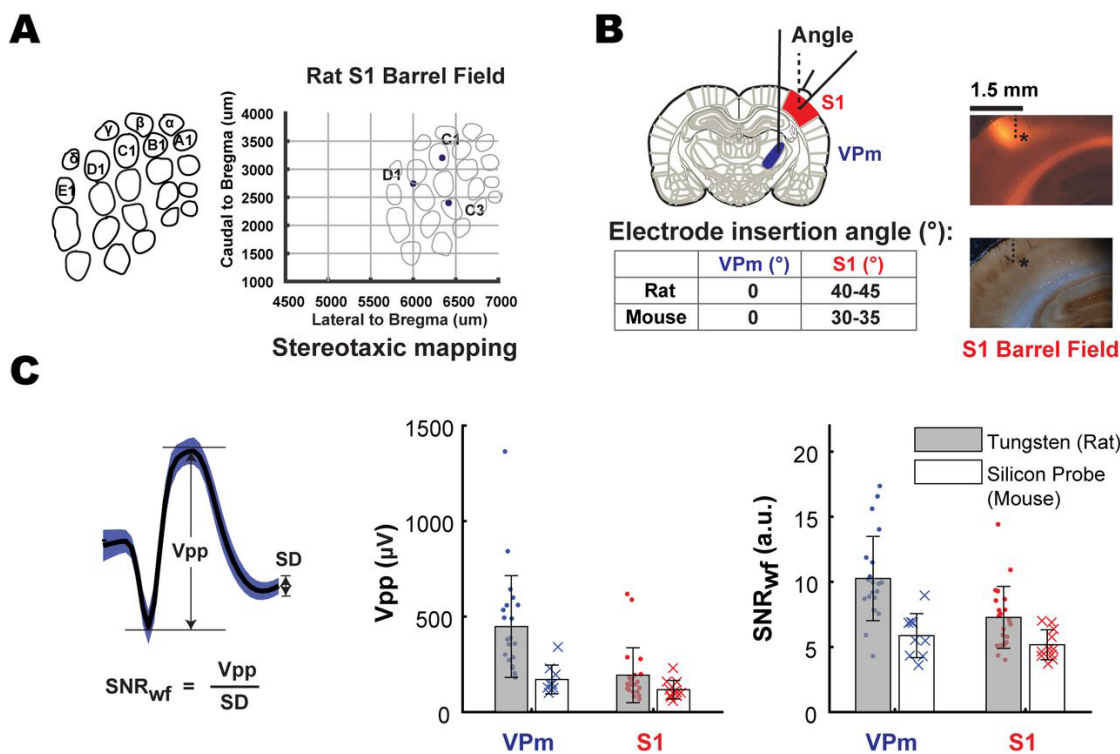
Furthermore, in this work, we focused exclusively on the reduction in responses, which is observed in the majority (~80%) of the thalamocortical neurons that we have recorded from. However, note that repetitive stimulation in the sensory pathway could result in both depressive and facilitative effects depending on stimulus frequency, pattern of stimulation as well as diversity in the neuronal subset (Barros-Zulaica et al. 2019; Kheradpezhough et al. 2017). Additionally, post-adaptation facilitation has also been reported in the rat somatosensory cortex (Cohen-Kashi Malina et al. 2013). Therefore, for future work, it will be important to 1) study much longer stimulus durations (10 seconds and beyond) to further expand the time spectrum, and 2) increase complexity of whisker stimuli (i.e., cross whisker adaptation paradigm) and track changes in the neighboring brain regions (such as activation that correspond to adjacent whiskers) in the thalamocortical circuit.

4.4 Concluding remarks

Bridging across different scales has been a central theme of this dissertation. We first expanded the scale of neural networks that we can record from simultaneously to gain insights about sensory coding and how brain structures (like the thalamocortical network)

transform sensory input over time. Secondly, we bridged across timescales, with a goal to uncover fundamental principles about the brain's coding strategies to deal with changes in the sensory environment. However, what we explored here, is only a limited investigation of the spatiotemporal scales of the transformation of sensory representation. Future work should continue to expand across spatial scales such as extending investigation in sensorimotor interaction, and multi-sensory integration across sensory modalities. Additionally, it is also critical to link observations across temporal scales that span multiple levels such as from genes and proteins interacting at the molecular level (milliseconds), to signaling across neuronal populations (millisecond-to-seconds), to neural mechanisms and behavior (seconds, hours to minutes) and social interactions (days, years, lifetime). While we are in the era where the theoretical and experimental tools to investigate neural circuitry are greatly expanded, bridging across scales to gain a holistic perspective of the inner workings of the nervous system is important because this enables us to develop and test theories about the governing principles of the brain. The iterative process of testing our hypotheses about brain computation is the only way to complete the puzzles presented by the brain. I would love to push in this direction to build an understanding of distributed neural representations across all spatiotemporal scales inherent in the brain and ultimately contribute to interventions that promote restoration of normal brain function.

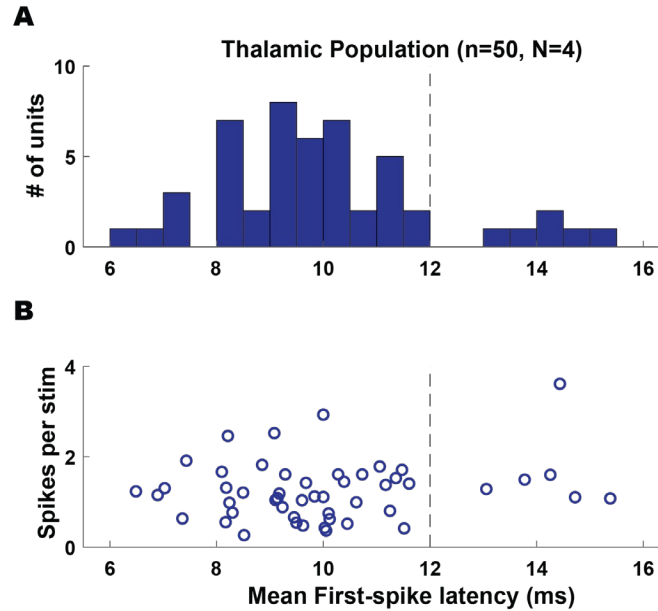
APPENDIX A



Figure_A-1 VPm-S1 targeting and unit isolation quality.

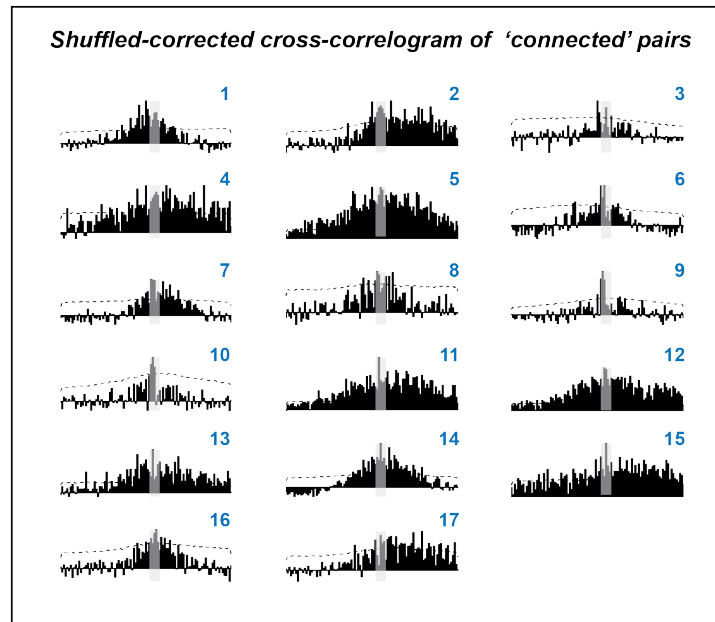
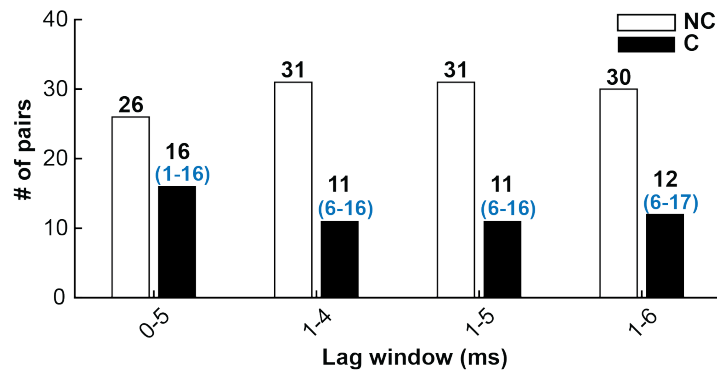
A. S1 targeting in rat (similar concept to IOS imaging in mouse, related to main Figure 2-2A): Prior to actual recording, location of S1 barrels was determined using functional measure (electrophysiology) and co-registered with stereotaxic coordinates relative to bregma. We mapped three distinct locations of the barrels and fitted a barrel map template using the triangulation method. This functional map was later used to guide electrode placement for targeting a desired barrel column. **B.** The optimal electrode insertion angle for targeting VPm and S1 in rat and mouse respectively. Histological images showed fluorescent electrode track (top) targeting S1 L4 (cytochrome oxidase staining at the bottom, see Methods) in a rat. Note: * and dotted line were plotted on both images to help registering location of fluorescent signal to barrels revealed by cytochrome oxidase staining. **C.** Schematic shows the wave-form characteristics of an example single-unit. Peak-to-peak amplitude (V_{pp}) was defined as the voltage difference between the peak and trough of the mean waveform. Signal-to-noise ratio (SNR_{wf}) of the waveform was defined as the ratio of the peak-to-peak voltage of the mean waveform divided by the standard deviation of the waveform. Single-units recorded using Tungsten microelectrodes in rats have slightly higher peak-to-peak amplitude and signal-to-noise ratio (V_{pp} : VPm (rat): $448 \pm 266 \mu V$, $n = 22$ neurons; VPm (mouse): $170 \pm 75.3 \mu V$, $n = 9$ neurons; S1 (rat): $170 \pm 75.3 \mu V$, $n = 22$, S1 (mouse): $117 \pm 48.6 \mu V$, $n = 11$; SNR_{wf} : VPm (rat): 10.3 ± 3.24 a.u., $n = 22$ neurons; VPm (mouse): 5.87 ± 1.69 a.u., $n = 9$ neurons; S1 (rat): 7.27 ± 2.38 a.u., $n =$

22, S1 (mouse): 5.17 ± 1.15 a.u., $n = 11$). All thalamic units have ISI violation $<2\%$ and cortical units have ISI violation $<1\%$.



Figure_A-2. Distribution of thalamic evoked responses to punctate whisker stimulation in mice.

A. Distribution of mean first-spike latency of evoked responses of thalamic population in response to 1st pulse of a repetitive (8-10Hz) transient stimulation (related to Figure 2-2D, not-adapted response). We found that majority of these cells (44 out of 50) exhibited short first-spike latency (9.43 ± 1.32 ms, mean \pm SEM). However, there were a small set of cells (6 out of 50) that exhibited longer latencies (13-15 ms), which could be secondary whisker responses (more likely) or POM responses (less likely). **B.** Corresponding averaged spikecount per stimulus as a function of mean first-spike latency for all units shown in A (1.25 ± 0.66 spikes/stim, mean \pm SEM, $n = 50$, single-unit and multi-unit data, excluding any neurons exhibiting reliability $<20\%$). Dotted line depicted latency cut-off for VPM neuron classification (see Methods).



Figure_A-3. Comparison of different lag windows for connectivity analysis for rat and mouse data.

Top: Distribution of 'not-connected' (NC) and 'connected' (C) pairs based on different selections of lag window on the cross-correlograms. The parenthesized numbers (blue) correspond to a collection of indexed cross-correlograms shown below. **Bottom:** Shuffled-corrected cross-correlograms for 'connected' pairs, pooled across all four lag windows. Note that each cross-correlogram is indexed from 1-17, depicting the total number of 'connected' pairs by any definition of lag windows. Note that cross-correlograms (index: 6-16) are the same pairs that were classified as 'connected' in Figure 2-4E, also shown in Figure 2-5).

REFERENCES

- Adibi M.** Whisker-Mediated Touch System in Rodents: From Neuron to Behavior. *Frontiers in Systems Neuroscience* 13: 2019.
- Adibi M, and Lampl I.** Sensory Adaptation in the Whisker-Mediated Tactile System: Physiology, Theory, and Function. *Frontiers in neuroscience* 15: 770011-770011, 2021.
- Agmon A, and O'Dowd DK.** NMDA receptor-mediated currents are prominent in the thalamocortical synaptic response before maturation of inhibition. *Journal of Neurophysiology* 68: 345-349, 1992.
- Ahissar E, Sosnik R, and Haidarliu S.** Transformation from temporal to rate coding in a somatosensory thalamocortical pathway. *Nature* 406: 302-306, 2000a.
- Ahissar E, Sosnik R, and Haidarliu S.** Transformation from temporal to rate coding in a somatosensory thalamocortical pathway. *Nature* 406: 302-306, 2000b.
- Ahrens MB, Orger MB, Robson DN, Li JM, and Keller PJ.** Whole-brain functional imaging at cellular resolution using light-sheet microscopy. *Nature Methods* 10: 413-420, 2013.
- Alitto HJ, and Usrey WM.** Corticothalamic feedback and sensory processing. *Curr Opin Neurobiol* 13: 440-445, 2003.
- Alitto HJ, Weyand TG, and Usrey WM.** Distinct properties of stimulus-evoked bursts in the lateral geniculate nucleus. *Journal of Neuroscience* 25: 514-523, 2005.
- Alonso J-M, and Martinez LM.** Functional connectivity between simple cells and complex cells in cat striate cortex. *Nat Neurosci* 1: 395-403, 1998.
- Alonso J-M, Usrey WM, and Reid RC.** Rules of Connectivity between Geniculate Cells and Simple Cells in Cat Primary Visual Cortex. *The Journal of Neuroscience* 21: 4002, 2001.
- Angulo MC, Rossier J, and Audinat E.** Postsynaptic glutamate receptors and integrative properties of fast-spiking interneurons in the rat neocortex. *J Neurophysiol* 82: 1295-1302, 1999.
- Baião PdAA.** Nanostructuring silicon probes via electrodeposition: Characterization of electrode coatings for acute in vivo neural recordings. 2014.

- Barlow HB.** Possible principles underlying the transformation of sensory messages. *Sensory communication* 1: 217-234, 1961.
- Barros-Zulaica N, Villa AEP, and Nuñez A.** Response Adaptation in Barrel Cortical Neurons Facilitates Stimulus Detection during Rhythmic Whisker Stimulation in Anesthetized Mice. *eNeuro* 6: 2019.
- Barthó P, Hirase H, Monconduit L, Zugaro M, Harris KD, and Buzsáki G.** Characterization of Neocortical Principal Cells and Interneurons by Network Interactions and Extracellular Features. *Journal of neurophysiology* 92: 600-608, 2004.
- Beierlein M, Fall CP, Rinzel J, and Yuste R.** Thalamocortical bursts trigger recurrent activity in neocortical networks: layer 4 as a frequency-dependent gate. *Journal of Neuroscience* 22: 9885-9894, 2002.
- Berényi A, Somogyvári Z, Nagy AJ, Roux L, Long JD, Fujisawa S, Stark E, Leonardo A, Harris TD, and Buzsáki G.** Large-scale, high-density (up to 512 channels) recording of local circuits in behaving animals. *Journal of Neurophysiology* 111: 1132-1149, 2014.
- Boloori A-R, Jenks RA, Desbordes G, and Stanley GB.** Encoding and decoding cortical representations of tactile features in the vibrissa system. *Journal of Neuroscience* 30: 9990-10005, 2010.
- Borden PY, Ortiz AD, Waiblinger C, Sederberg AJ, Morrisette AE, Forest CR, Jaeger D, and Stanley GB.** Genetically expressed voltage sensor ArcLight for imaging large scale cortical activity in the anesthetized and awake mouse (erratum). *Neurophotonics* 4: 039801, 2017.
- Borden PY, Wright NC, Morrisette AE, Jaeger D, Haider B, and Stanley GB.** Thalamic bursting and the role of timing and synchrony in thalamocortical signaling in the awake mouse. *bioRxiv* 2021.2007.2009.451656, 2022.
- Briggs F, and Usrey WM.** Parallel Processing in the Corticogeniculate Pathway of the Macaque Monkey. *Neuron* 62: 135-146, 2009.
- Bruno RM, and Sakmann B.** Cortex is driven by weak but synchronously active thalamocortical synapses. *Science* 312: 1622-1627, 2006.
- Bruno RM, and Simons DJ.** Feedforward mechanisms of excitatory and inhibitory cortical receptive fields. *The Journal of neuroscience : the official journal of the Society for Neuroscience* 22: 10966-10975, 2002.
- Butts DA, Weng C, Jin J, Yeh CI, Lesica NA, Alonso JM, and Stanley GB.** Temporal precision in the neural code and the timescales of natural vision. *Nature* 449: 92-95, 2007.

- Buzsáki G.** Large-scale recording of neuronal ensembles. *Nat Neurosci* 7: 446-451, 2004.
- Buzsáki G, Stark E, Berényi A, Khodagholy D, Kipke DR, Yoon E, and Wise KD.** Tools for probing local circuits: high-density silicon probes combined with optogenetics. *Neuron* 86: 92-105, 2015.
- Castejon C, Barros-Zulaica N, and Nuñez A.** Control of somatosensory cortical processing by thalamic posterior medial nucleus: a new role of thalamus in cortical Function. *PloS one* 11: e0148169, 2016.
- Castro-Alamancos MA.** Absence of rapid sensory adaptation in neocortex during information processing states. *Neuron* 41: 455-464, 2004a.
- Castro-Alamancos MA.** Dynamics of sensory thalamocortical synaptic networks during information processing states. *Progress in neurobiology* 74: 213-247, 2004b.
- Castro - Alamancos MA, and Oldford E.** Cortical sensory suppression during arousal is due to the activity - dependent depression of thalamocortical synapses. *The Journal of physiology* 541: 319-331, 2002.
- Chance FS, and Abbott LF.** Input-specific adaptation in complex cells through synaptic depression. *Neurocomputing* 38-40: 141-146, 2001.
- Chen Z, Putrino DF, Ghosh S, Barbieri R, and Brown EN.** Statistical Inference for Assessing Functional Connectivity of Neuronal Ensembles With Sparse Spiking Data. *IEEE Transactions on Neural Systems and Rehabilitation Engineering* 19: 121-135, 2011.
- Chistiakova M, Bannon NM, Bazhenov M, and Volgushev M.** Heterosynaptic plasticity: multiple mechanisms and multiple roles. *The Neuroscientist : a review journal bringing neurobiology, neurology and psychiatry* 20: 483-498, 2014.
- Chung JE, Joo HR, Fan JL, Liu DF, Barnett AH, Chen S, Geaghan-Breiner C, Karlsson MP, Karlsson M, Lee KY, Liang H, Magland JF, Pebbles JA, Tooker AC, Greengard LF, Tolosa VM, and Frank LM.** High-Density, Long-Lasting, and Multi-region Electrophysiological Recordings Using Polymer Electrode Arrays. *Neuron* 101: 21-31.e25, 2019.
- Chung S, Li X, and Nelson SB.** Short-Term Depression at Thalamocortical Synapses Contributes to Rapid Adaptation of Cortical Sensory Responses In Vivo. *Neuron* 34: 437-446, 2002.
- Cohen-Kashi Malina K, Jubran M, Katz Y, and Lampl I.** Imbalance between Excitation and Inhibition in the Somatosensory Cortex Produces Postadaptation Facilitation. *The Journal of Neuroscience* 33: 8463-8471, 2013.
- Constantinople CM, and Bruno RM.** Deep Cortical Layers Are Activated Directly by Thalamus. *Science* 340: 1591-1594, 2013.

- Crandall Shane R, Cruikshank Scott J, and Connors Barry W.** A Corticothalamic Switch: Controlling the Thalamus with Dynamic Synapses. *Neuron* 86: 768-782, 2015.
- Crochet S, and Petersen CCH.** Correlating whisker behavior with membrane potential in barrel cortex of awake mice. *Nat Neurosci* 9: 608-610, 2006.
- Cruikshank SJ, Lewis TJ, and Connors BW.** Synaptic basis for intense thalamocortical activation of feedforward inhibitory cells in neocortex. *Nat Neurosci* 10: 462-468, 2007a.
- Cruikshank SJ, Lewis TJ, and Connors BW.** Synaptic basis for intense thalamocortical activation of feedforward inhibitory cells in neocortex. *Nat Neurosci* 10: 462-468, 2007b.
- Csicsvari J, Hirase H, Czurko A, and Buzsáki G.** Reliability and state dependence of pyramidal cell-interneuron synapses in the hippocampus: an ensemble approach in the behaving rat. *Neuron* 21: 179-189, 1998.
- Dash S, Autio DM, and Crandall SR.** State-Dependent Modulation of Activity in Distinct Layer 6 Corticothalamic Neurons in Barrel Cortex of Awake Mice. *The Journal of Neuroscience* 42: 6551-6565, 2022.
- Debanne D, Boudkkazi S, Campanac E, Cudmore RH, Giraud P, Fronzaroli-Molinieres L, Carlier E, and Caillard O.** Paired-recordings from synaptically coupled cortical and hippocampal neurons in acute and cultured brain slices. *Nature protocols* 3: 1559-1568, 2008.
- del Mar Quiroga M, Morris AP, and Krekelberg B.** Adaptation without plasticity. *Cell Rep* 17: 58-68, 2016.
- Denning KS, and Reinagel P.** Visual control of burst priming in the anesthetized lateral geniculate nucleus. *Journal of Neuroscience* 25: 3531-3538, 2005.
- Diamond ME, Armstrong - James M, and Ebner FF.** Somatic sensory responses in the rostral sector of the posterior group (POm) and in the ventral posterior medial nucleus (VPM) of the rat thalamus. *Journal of Comparative Neurology* 318: 462-476, 1992.
- Díaz-Quesada M, Martini FJ, Ferrati G, Bureau I, and Maravall M.** Diverse thalamocortical short-term plasticity elicited by ongoing stimulation. *Journal of Neuroscience* 34: 515-526, 2014.
- Dragoi V, Sharma J, and Sur M.** Adaptation-induced plasticity of orientation tuning in adult visual cortex. *Neuron* 28: 287-298, 2000.
- Drew PJ, and Abbott LF.** Models and properties of power-law adaptation in neural systems. *Journal of neurophysiology* 96: 826-833, 2006.

- English DF, McKenzie S, Evans T, Kim K, Yoon E, and Buzsáki G.** Pyramidal Cell-Interneuron Circuit Architecture and Dynamics in Hippocampal Networks. *Neuron* 96: 505-520.e507, 2017.
- Erişir A, Van Horn SC, Bickford ME, and Sherman SM.** Immunocytochemistry and distribution of parabrachial terminals in the lateral geniculate nucleus of the cat: a comparison with corticogeniculate terminals. *Journal of Comparative Neurology* 377: 535-549, 1997a.
- Erişir A, Van Horn SC, and Sherman SM.** Relative numbers of cortical and brainstem inputs to the lateral geniculate nucleus. *Proceedings of the National Academy of Sciences* 94: 1517-1520, 1997b.
- Fairhall A, Lewen G, Bialek W, and van Steveninck R.** Multiple timescales of adaptation in a neural code. *Advances in neural information processing systems* 13: 2000.
- Fanselow Erika E, Sameshima K, Baccala Luiz A, and Nicolelis Miguel AL.** Thalamic bursting in rats during different awake behavioral states. *Proceedings of the National Academy of Sciences* 98: 15330-15335, 2001.
- Feldman DE.** Synaptic mechanisms for plasticity in neocortex. *Annual review of neuroscience* 32: 33-55, 2009.
- Felsen G, Shen Y-s, Yao H, Spor G, Li C, and Dan Y.** Dynamic modification of cortical orientation tuning mediated by recurrent connections. *Neuron* 36: 945-954, 2002.
- Fiáth R, Márton AL, Mátyás F, Pinke D, Márton G, Tóth K, and Ulbert I.** Slow insertion of silicon probes improves the quality of acute neuronal recordings. *Scientific Reports* 9: 111, 2019.
- Fiáth R, Raducanu BC, Musa S, Andrei A, Lopez CM, van Hoof C, Ruther P, Aarts A, Horváth D, and Ulbert I.** A silicon-based neural probe with densely-packed low-impedance titanium nitride microelectrodes for ultrahigh-resolution in vivo recordings. *Biosensors and Bioelectronics* 106: 86-92, 2018.
- Franklin K, and Paxinos G.** *The mouse brain in stereotaxic coordinates, compact. The coronal plates and diagrams.* Amsterdam: Elsevier Academic Press, 2008.
- Fujisawa S, Amarasingham A, Harrison MT, and Buzsaki G.** Behavior-dependent short-term assembly dynamics in the medial prefrontal cortex. *Nat Neurosci* 11: 823-833, 2008.
- Furuta T, Kaneko T, and Deschenes M.** Septal neurons in barrel cortex derive their receptive field input from the lemniscal pathway. *The Journal of neuroscience : the official journal of the Society for Neuroscience* 29: 4089-4095, 2009.

- Gabernet L, Jadhav SP, Feldman DE, Carandini M, and Scanziani M.** Somatosensory integration controlled by dynamic thalamocortical feed-forward inhibition. *Neuron* 48: 315-327, 2005a.
- Gabernet L, Jadhav SP, Feldman DE, Carandini M, and Scanziani M.** Somatosensory integration controlled by dynamic thalamocortical feed-forward inhibition. *Neuron* 48: 315-327, 2005b.
- Gil Z, and Amitai Y.** Properties of Convergent Thalamocortical and Intracortical Synaptic Potentials in Single Neurons of Neocortex. *The Journal of Neuroscience* 16: 6567-6578, 1996.
- Gilboa G, Chen R, and Brenner N.** History-dependent multiple-time-scale dynamics in a single-neuron model. *The Journal of neuroscience : the official journal of the Society for Neuroscience* 25: 6479-6489, 2005.
- Ginzburg II, and Sompolinsky H.** Theory of correlations in stochastic neural networks. *Physical review E, Statistical physics, plasmas, fluids, and related interdisciplinary topics* 50: 3171-3191, 1994.
- Gollnick CA, Millard DC, Ortiz AD, Bellamkonda RV, and Stanley GB.** Response reliability observed with voltage-sensitive dye imaging of cortical layer 2/3: the probability of activation hypothesis. *Journal of neurophysiology* 115: 2456-2469, 2016.
- Gong S, Doughty M, Harbaugh CR, Cummins A, Hatten ME, Heintz N, and Gerfen CR.** Targeting Cre recombinase to specific neuron populations with bacterial artificial chromosome constructs. *Journal of Neuroscience* 27: 9817-9823, 2007.
- Gray CM, Maldonado PE, Wilson M, and McNaughton B.** Tetrodes markedly improve the reliability and yield of multiple single-unit isolation from multi-unit recordings in cat striate cortex. *Journal of neuroscience methods* 63: 43-54, 1995.
- Guido W, Lu S-M, and Sherman SM.** Relative contributions of burst and tonic responses to the receptive field properties of lateral geniculate neurons in the cat. *Journal of neurophysiology* 68: 2199-2211, 1992.
- Guillery R.** A quantitative study of synaptic interconnections in the dorsal lateral geniculate nucleus of the cat. *Z Zellforsch* 96: 39-48, 1969.
- Gutnisky DA, and Dragoi V.** Adaptive coding of visual information in neural populations. *Nature* 452: 220, 2008.
- Happel MFK, Hechavarria JC, and de Hoz L.** Editorial: Cortical-Subcortical Loops in Sensory Processing. *Frontiers in Neural Circuits* 16: 2022.
- Hardingham N, Glazewski S, Pakhotin P, Mizuno K, Chapman PF, Giese KP, and Fox K.** Neocortical long-term potentiation and experience-dependent synaptic

plasticity require alpha-calcium/calmodulin-dependent protein kinase II autophosphorylation. *The Journal of neuroscience : the official journal of the Society for Neuroscience* 23: 4428-4436, 2003.

Harris KD, Henze DA, Csicsvari J, Hirase H, and Buzsáki G. Accuracy of tetrode spike separation as determined by simultaneous intracellular and extracellular measurements. *J Neurophysiol* 84: 401-414, 2000.

Heiss JE, Katz Y, Ganmor E, and Lampl I. Shift in the balance between excitation and inhibition during sensory adaptation of S1 neurons. *Journal of Neuroscience* 28: 13320-13330, 2008.

Heynen AJ, and Bear MF. Long-term potentiation of thalamocortical transmission in the adult visual cortex in vivo. *The Journal of neuroscience : the official journal of the Society for Neuroscience* 21: 9801-9813, 2001.

Hull C, and Scanziani M. It's about time for thalamocortical circuits. *Nat Neurosci* 10: 400-402, 2007.

Insel TR, Landis SC, and Collins FS. Research priorities. The NIH BRAIN Initiative. *Science* 340: 687-688, 2013.

Isaacson JS, and Scanziani M. How inhibition shapes cortical activity. *Neuron* 72: 231-243, 2011.

Jiang X, Shen S, Cadwell CR, Berens P, Sinz F, Ecker AS, Patel S, and Tolias AS. Principles of connectivity among morphologically defined cell types in adult neocortex. *Science* 350: 2015.

Jouhanneau J-S, Kremkow J, Dorn AL, and Poulet JFA. In Vivo Monosynaptic Excitatory Transmission between Layer 2 Cortical Pyramidal Neurons. *Cell Rep* 13: 2098-2106, 2015.

Jouhanneau J-S, Kremkow J, and Poulet JFA. Single synaptic inputs drive high-precision action potentials in parvalbumin expressing GABA-ergic cortical neurons in vivo. *Nature Communications* 9: 1540, 2018.

Jouhanneau J-S, and Poulet JFA. Multiple Two-Photon Targeted Whole-Cell Patch-Clamp Recordings From Monosynaptically Connected Neurons in vivo. *Frontiers in Synaptic Neuroscience* 11: 2019.

Juavinett AL, Bekheet G, and Churchland AK. Chronically-implanted Neuropixels probes enable high yield recordings in freely moving mice. *bioRxiv* 406074, 2018.

Jun JJ, Steinmetz NA, Siegle JH, Denman DJ, Bauza M, Barbarits B, Lee AK, Anastassiou CA, Andrei A, Aydın Ç, Barbic M, Blanche TJ, Bonin V, Couto J, Dutta B, Gratiy SL, Gutnisky DA, Häusser M, Karsh B, Ledochowitsch P, Lopez CM, Mitelut C, Musa S, Okun M, Pachitariu M, Putzeys J, Rich PD,

- Rossant C, Sun W-l, Svoboda K, Carandini M, Harris KD, Koch C, O'Keefe J, and Harris TD.** Fully integrated silicon probes for high-density recording of neural activity. *Nature* 551: 232-236, 2017.
- Kandel ER, Schwartz JH, Jessell TM, Siegelbaum S, Hudspeth AJ, and Mack S.** *Principles of neural science*. McGraw-hill New York, 2000.
- Kathleen Kelly GEC, Jed A. Hartings, Daniel J. Simons, M.** Axonal conduction properties of antidromically identified neurons in rat barrel cortex. *Somatosensory & motor research* 18: 202-210, 2001.
- Katz Y, Heiss JE, and Lampl I.** Cross-whisker adaptation of neurons in the rat barrel cortex. *Journal of Neuroscience* 26: 13363-13372, 2006.
- Kawaguchi Y, and Kubota Y.** Correlation of physiological subgroupings of nonpyramidal cells with parvalbumin-and calbindinD28k-immunoreactive neurons in layer V of rat frontal cortex. *Journal of neurophysiology* 70: 387-396, 1993.
- Khatri V, Bruno RM, and Simons DJ.** Stimulus-specific and stimulus-nonspecific firing synchrony and its modulation by sensory adaptation in the whisker-to-barrel pathway. *Journal of neurophysiology* 101: 2328-2338, 2009.
- Khatri V, Hartings JA, and Simons DJ.** Adaptation in thalamic barreloid and cortical barrel neurons to periodic whisker deflections varying in frequency and velocity. *J Neurophysiol* 92: 3244-3254, 2004.
- Kheradpezhough E, Adibi M, and Arabzadeh E.** Response dynamics of rat barrel cortex neurons to repeated sensory stimulation. *Scientific Reports* 7: 11445, 2017.
- Kirchgessner MA, Franklin AD, and Callaway EM.** Context-dependent and dynamic functional influence of corticothalamic pathways to first- and higher-order visual thalamus. *Proceedings of the National Academy of Sciences* 117: 13066-13077, 2020.
- Knott GW, Quairiaux C, Genoud C, and Welker E.** Formation of Dendritic Spines with GABAergic Synapses Induced by Whisker Stimulation in Adult Mice. *Neuron* 34: 265-273, 2002.
- Kobayashi R, and Kitano K.** Impact of network topology on inference of synaptic connectivity from multi-neuronal spike data simulated by a large-scale cortical network model. *Journal of computational neuroscience* 35: 109-124, 2013.
- Kobayashi R, Kurita S, Kurth A, Kitano K, Mizuseki K, Diesmann M, Richmond BJ, and Shinomoto S.** Reconstructing neuronal circuitry from parallel spike trains. *Nature Communications* 10: 4468, 2019.

- Kodandaramaiah SB, Flores FJ, Holst GL, Singer AC, Han X, Brown EN, Boyden ES, and Forest CR.** Multi-neuron intracellular recording in vivo via interacting autpatching robots. *Elife* 7: e24656, 2018.
- Landisman CE, and Connors BW.** VPM and PoM nuclei of the rat somatosensory thalamus: intrinsic neuronal properties and corticothalamic feedback. *Cereb Cortex* 17: 2853-2865, 2007.
- Latimer KW, Barbera D, Sokoletsky M, Awwad B, Katz Y, Nelken I, Lampl I, Fairhall AL, and Priebe NJ.** Multiple Timescales Account for Adaptive Responses across Sensory Cortices. *The Journal of Neuroscience* 39: 10019-10033, 2019.
- Latimer KW, and Fairhall AL.** Capturing Multiple Timescales of Adaptation to Second-Order Statistics With Generalized Linear Models: Gain Scaling and Fractional Differentiation. *Frontiers in Systems Neuroscience* 14: 2020.
- Lee C, Lavoie A, Liu J, Chen SX, and Liu B-h.** Light Up the Brain: The Application of Optogenetics in Cell-Type Specific Dissection of Mouse Brain Circuits. *Frontiers in Neural Circuits* 14: 2020.
- Lee S-H, Kwan AC, Zhang S, Phoumthipphavong V, Flannery JG, Masmanidis SC, Taniguchi H, Huang ZJ, Zhang F, Boyden ES, Deisseroth K, and Dan Y.** Activation of specific interneurons improves V1 feature selectivity and visual perception. *Nature* 488: 379, 2012.
- Lefort S, Tómm C, Floyd Sarria JC, and Petersen CC.** The excitatory neuronal network of the C2 barrel column in mouse primary somatosensory cortex. *Neuron* 61: 301-316, 2009.
- Lepperød ME, Stöber T, Hafting T, Fyhn M, and Kording KP.** Inferring causal connectivity from pairwise recordings and optogenetics. *bioRxiv* 463760, 2018.
- Lesica NA, and Stanley GB.** Encoding of natural scene movies by tonic and burst spikes in the lateral geniculate nucleus. *Journal of Neuroscience* 24: 10731-10740, 2004.
- Li Y-t, Ibrahim LA, Liu B-h, Zhang LI, and Tao HW.** Linear transformation of thalamocortical input by intracortical excitation. *Nat Neurosci* 16: 1324-1330, 2013.
- Lien AD, and Scanziani M.** Cortical direction selectivity emerges at convergence of thalamic synapses. *Nature* 558: 80-86, 2018.
- Lien AD, and Scanziani M.** Tuned thalamic excitation is amplified by visual cortical circuits. *Nat Neurosci* 16: 1315-1323, 2013.

- Liew YJ, Pala A, Whitmire CJ, Stoy WA, Forest CR, and Stanley GB.** Inferring thalamocortical monosynaptic connectivity in vivo. *Journal of Neurophysiology* 125: 2408-2431, 2021.
- Liu XB, Honda C, and Jones E.** Distribution of four types of synapse on physiologically identified relay neurons in the ventral posterior thalamic nucleus of the cat. *Journal of Comparative Neurology* 352: 69-91, 1995.
- London M, Roth A, Beeren L, Häusser M, and Latham PE.** Sensitivity to perturbations in vivo implies high noise and suggests rate coding in cortex. *Nature* 466: 123-127, 2010.
- Lu L, Fu X, Liew Y, Zhang Y, Zhao S, Xu Z, Zhao J, Li D, Li Q, Stanley GB, and Duan X.** Soft and MRI Compatible Neural Electrodes from Carbon Nanotube Fibers. *Nano Letters* 19: 1577-1586, 2019.
- Lütcke H, Gerhard F, Zenke F, Gerstner W, and Helmchen F.** Inference of neuronal network spike dynamics and topology from calcium imaging data. *Frontiers in Neural Circuits* 7: 2013.
- Mainen Z, and Sejnowski T.** Reliability of spike timing in neocortical neurons. *Science* 268: 1503-1506, 1995.
- Malina KC-K, Jubran M, Katz Y, and Lampl I.** Imbalance between excitation and inhibition in the somatosensory cortex produces postadaptation facilitation. *Journal of Neuroscience* 33: 8463-8471, 2013.
- Malinow R, and Malenka RC.** AMPA receptor trafficking and synaptic plasticity. *Annual review of neuroscience* 25: 103-126, 2002.
- Masri R, Bezdudnaya T, Trageser JC, and Keller A.** Encoding of stimulus frequency and sensor motion in the posterior medial thalamic nucleus. *J Neurophysiol* 100: 681-689, 2008.
- Matsumura M, Chen D-f, Sawaguchi T, Kubota K, and Fetz EE.** Synaptic Interactions between Primate Precentral Cortex Neurons Revealed by Spike-Triggered Averaging of Intracellular Membrane Potentials In Vivo. *The Journal of Neuroscience* 16: 7757, 1996.
- Mease RA, Krieger P, and Groh A.** Cortical control of adaptation and sensory relay mode in the thalamus. *Proceedings of the National Academy of Sciences* 111: 6798-6803, 2014.
- Millard DC, and Stanley GB.** Anatomically based Bayesian decoding of the cortical response to intracortical microstimulation. In: *2013 6th International IEEE/EMBS Conference on Neural Engineering (NER)2013*, p. 1457-1460.

- Millard DC, Whitmire CJ, Gollnick CA, Rozell CJ, and Stanley GB.** Electrical and Optical Activation of Mesoscale Neural Circuits with Implications for Coding. *The Journal of Neuroscience* 35: 15702-15715, 2015.
- Miller LM, Escabi MA, Read HL, and Schreiner CE.** Functional convergence of response properties in the auditory thalamocortical system. *Neuron* 32: 151-160, 2001.
- Muniak MA, Ray S, Hsiao SS, Dammann JF, and Bensmaia SJ.** The Neural Coding of Stimulus Intensity: Linking the Population Response of Mechanoreceptive Afferents with Psychophysical Behavior. *The Journal of Neuroscience* 27: 11687, 2007.
- Nowak L, and J B.** Cross correlograms for neuronal spike trains. Different types of temporal correlation in neocortex, their origin and significance. 2000, p. 53-96.
- Okatan M, Wilson MA, and Brown EN.** Analyzing functional connectivity using a network likelihood model of ensemble neural spiking activity. *Neural computation* 17: 1927-1961, 2005.
- Okun M, Lak A, Carandini M, and Harris KD.** Long Term Recordings with Immobile Silicon Probes in the Mouse Cortex. *PloS one* 11: e0151180-e0151180, 2016.
- Ollerenshaw DR, Zheng HJ, Millard DC, Wang Q, and Stanley GB.** The adaptive trade-off between detection and discrimination in cortical representations and behavior. *Neuron* 81: 1152-1164, 2014.
- Ostojic S, Brunel N, and Hakim V.** How Connectivity, Background Activity, and Synaptic Properties Shape the Cross-Correlation between Spike Trains. *The Journal of Neuroscience* 29: 10234-10253, 2009.
- Pala A, and Petersen CC.** In vivo measurement of cell-type-specific synaptic connectivity and synaptic transmission in layer 2/3 mouse barrel cortex. *Neuron* 85: 68-75, 2015.
- Paninski L, Pillow JW, and Simoncelli EP.** Maximum likelihood estimation of a stochastic integrate-and-fire neural encoding model. *Neural computation* 16: 2533-2561, 2004.
- Patterson CA, Wissig SC, and Kohn A.** Distinct Effects of Brief and Prolonged Adaptation on Orientation Tuning in Primary Visual Cortex. *The Journal of Neuroscience* 33: 532, 2013.
- Paxinos G, and Watson C.** The rat brain in stereotaxic coordinates. *Qingchuan Zhuge translate* 32: 2007.
- Perkel DH, Gerstein GL, and Moore GP.** Neuronal spike trains and stochastic point processes. II. Simultaneous spike trains. *Biophysical journal* 7: 419-440, 1967.

- Petersen CC.** The functional organization of the barrel cortex. *Neuron* 56: 339-355, 2007.
- Pfeffer CK, Xue M, He M, Huang ZJ, and Scanziani M.** Inhibition of inhibition in visual cortex: the logic of connections between molecularly distinct interneurons. *Nat Neurosci* 16: 1068-1076, 2013.
- Phillips J, Johnson K, and Hsiao S.** Spatial pattern representation and transformation in monkey somatosensory cortex. *Proceedings of the National Academy of Sciences* 85: 1317-1321, 1988.
- Pinto DJ, Brumberg JC, and Simons DJ.** Circuit Dynamics and Coding Strategies in Rodent Somatosensory Cortex. *Journal of Neurophysiology* 83: 1158-1166, 2000.
- Poulet JF, Fernandez LM, Crochet S, and Petersen CC.** Thalamic control of cortical states. *Nat Neurosci* 15: 370-372, 2012.
- Raducanu BC, Yazicioglu RF, Lopez CM, Ballini M, Putzeys J, Wang S, Andrei A, Welkenhuysen M, Helleputte Nv, Musa S, Puers R, Kloosterman F, Hoof Cv, and Mitra S.** Time multiplexed active neural probe with 678 parallel recording sites. In: *2016 46th European Solid-State Device Research Conference (ESSDERC)2016*, p. 385-388.
- Reid RC, and Alonso JM.** Specificity of monosynaptic connections from thalamus to visual cortex. *Nature* 378: 281-284, 1995.
- Reinagel P, Godwin D, Sherman SM, and Koch C.** Encoding of visual information by LGN bursts. *Journal of neurophysiology* 81: 2558-2569, 1999.
- Reinagel P, and Reid RC.** Temporal Coding of Visual Information in the Thalamus. *The Journal of Neuroscience* 20: 5392, 2000.
- Reinhold K, Lien AD, and Scanziani M.** Distinct recurrent versus afferent dynamics in cortical visual processing. *Nat Neurosci* 18: 1789-1797, 2015.
- Rios G, Lubenov EV, Chi D, Roukes ML, and Siapas AG.** Nanofabricated Neural Probes for Dense 3-D Recordings of Brain Activity. *Nano Letters* 16: 6857-6862, 2016.
- Saito K, Otsuru N, Inukai Y, Kojima S, Miyaguchi S, Tsuiki S, Sasaki R, and Onishi H.** Inhibitory Mechanisms in Primary Somatosensory Cortex Mediate the Effects of Peripheral Electrical Stimulation on Tactile Spatial Discrimination. *Neuroscience* 384: 262-274, 2018.
- Salinas E, Hernandez A, Zainos A, and Romo R.** Periodicity and firing rate as candidate neural codes for the frequency of vibrotactile stimuli. *The Journal of neuroscience : the official journal of the Society for Neuroscience* 20: 5503-5515, 2000.

- Sedigh-Sarvestani M, Vigeland L, Fernandez-Lamo I, Taylor MM, Palmer LA, and Contreras D.** Intracellular, &em>In Vivo&em>, Dynamics of Thalamocortical Synapses in Visual Cortex. *The Journal of Neuroscience* 37: 5250, 2017.
- Sheikhattar A, Miran S, Liu J, Fritz JB, Shamma SA, Kanold PO, and Babadi B.** Extracting neuronal functional network dynamics via adaptive Granger causality analysis. *Proceedings of the National Academy of Sciences* 115: E3869, 2018.
- Sherman SM.** Tonic and burst firing: dual modes of thalamocortical relay. *Trends in neurosciences* 24: 122-126, 2001.
- Sherman SM, and Guillery RW.** Functional organization of thalamocortical relays. *Journal of Neurophysiology* 76: 1367-1395, 1996.
- Simons DJ, and Carvell GE.** Thalamocortical response transformation in the rat vibrissa/barrel system. *J Neurophysiol* 61: 311-330, 1989.
- Sitnikova EY, and Raevskii VV.** The lemniscal and paralemniscal pathways of the trigeminal system in rodents are integrated at the level of the somatosensory cortex. *Neuroscience and behavioral physiology* 40: 325-331, 2010.
- Sosnik R, Haidarliu S, and Ahissar E.** Temporal frequency of whisker movement. I. Representations in brain stem and thalamus. *Journal of Neurophysiology* 86: 339-353, 2001.
- Steriade M, and Llinás RR.** The functional states of the thalamus and the associated neuronal interplay. *Physiological reviews* 68: 649-742, 1988.
- Stevenson IH, Rebesco JM, Miller LE, and Körding KP.** Inferring functional connections between neurons. *Curr Opin Neurobiol* 18: 582-588, 2008.
- Storchi R, Bale MR, Biella GEM, and Petersen RS.** Comparison of latency and rate coding for the direction of whisker deflection in the subcortical somatosensory pathway. *Journal of neurophysiology* 108: 1810-1821, 2012.
- Stoy WA, Kolb I, Holst GL, Liew Y, Pala A, Yang B, Boyden ES, Stanley GB, and Forest CR.** Robotic navigation to subcortical neural tissue for intracellular electrophysiology in vivo. *Journal of Neurophysiology* 118: 1141-1150, 2017.
- Swadlow H, Waxman S, and Rosene D.** Latency variability and the identification of antidromically activated neurons in mammalian brain. *Experimental brain research* 32: 439-443, 1978.
- Swadlow HA.** Efferent neurons and suspected interneurons in S-1 vibrissa cortex of the awake rabbit: receptive fields and axonal properties. *Journal of Neurophysiology* 62: 288-308, 1989.

- Swadlow HA.** Fast-spike interneurons and feedforward inhibition in awake sensory neocortex. *Cerebral Cortex* 13: 25-32, 2003.
- Swadlow HA, and Gusev AG.** The impact of 'bursting' thalamic impulses at a neocortical synapse. *Nat Neurosci* 4: 402-408, 2001.
- Takahashi T, Svoboda K, and Malinow R.** Experience strengthening transmission by driving AMPA receptors into synapses. *Science* 299: 1585-1588, 2003.
- Temereanca S, Brown EN, and Simons DJ.** Rapid changes in thalamic firing synchrony during repetitive whisker stimulation. *The Journal of neuroscience : the official journal of the Society for Neuroscience* 28: 11153-11164, 2008.
- Temereanca S, and Simons DJ.** Functional Topography of Corticothalamic Feedback Enhances Thalamic Spatial Response Tuning in the Somatosensory Whisker/Barrel System. *Neuron* 41: 639-651, 2004.
- Urbain N, Salin PA, Libourel P-A, Comte J-C, Gentet LJ, and Petersen CC.** Whisking-related changes in neuronal firing and membrane potential dynamics in the somatosensory thalamus of awake mice. *Cell Rep* 13: 647-656, 2015.
- Van Essen DC, Ugurbil K, Auerbach E, Barch D, Behrens TE, Bucholz R, Chang A, Chen L, Corbetta M, Curtiss SW, Della Penna S, Feinberg D, Glasser MF, Harel N, Heath AC, Larson-Prior L, Marcus D, Michalareas G, Moeller S, Oostenveld R, Petersen SE, Prior F, Schlaggar BL, Smith SM, Snyder AZ, Xu J, and Yacoub E.** The Human Connectome Project: a data acquisition perspective. *NeuroImage* 62: 2222-2231, 2012.
- Van Horn SC, Erişir A, and Sherman SM.** Relative distribution of synapses in the A - laminae of the lateral geniculate nucleus of the cat. *Journal of Comparative Neurology* 416: 509-520, 2000.
- Wang Q, Webber RM, and Stanley GB.** Thalamic synchrony and the adaptive gating of information flow to cortex. *Nat Neurosci* 13: 1534-1541, 2010.
- Wang X, Wei Y, Vaingankar V, Wang Q, Koepsell K, Sommer FT, and Hirsch JA.** Feedforward Excitation and Inhibition Evoke Dual Modes of Firing in the Cat's Visual Thalamus during Naturalistic Viewing. *Neuron* 55: 465-478, 2007.
- Wark B, Lundstrom BN, and Fairhall A.** Sensory adaptation. *Current opinion in neurobiology* 17: 423-429, 2007.
- Welker E, Rao S, Dorfl J, Melzer P, and van der Loos H.** Plasticity in the barrel cortex of the adult mouse: effects of chronic stimulation upon deoxyglucose uptake in the behaving animal. *The Journal of Neuroscience* 12: 153-170, 1992.
- Whitmire CJ, Liew YJ, and Stanley GB.** Thalamic state influences timing precision in the thalamocortical circuit. *J Neurophysiol* 125: 1833-1850, 2021.

- Whitmire CJ, and Stanley GB.** Rapid Sensory Adaptation Redux: A Circuit Perspective. *Neuron* 92: 298-315, 2016.
- Whitmire CJ, Waiblinger C, Schwarz C, and Stanley GB.** Information Coding through Adaptive Gating of Synchronized Thalamic Bursting. *Cell Rep* 14: 795-807, 2016.
- Wilent WB, and Contreras D.** Dynamics of excitation and inhibition underlying stimulus selectivity in rat somatosensory cortex. *Nat Neurosci* 8: 1364-1370, 2005.
- Wright NC, Borden PY, Liew YJ, Bolus MF, Stoy WM, Forest CR, and Stanley GB.** Rapid Cortical Adaptation and the Role of Thalamic Synchrony during Wakefulness. *The Journal of neuroscience : the official journal of the Society for Neuroscience* 41: 5421-5439, 2021a.
- Wright NC, Borden PY, Liew YJ, Bolus MF, Stoy WM, Forest CR, and Stanley GB.** Rapid Cortical Adaptation and the Role of Thalamic Synchrony During Wakefulness. *bioRxiv* 2020.2010.2008.331660, 2021b.
- Yu C, Derdikman D, Haidarliu S, and Ahissar E.** Parallel thalamic pathways for whisking and touch signals in the rat. *PLoS biology* 4: e124, 2006.
- Yu J, and Ferster D.** Functional Coupling from Simple to Complex Cells in the Visually Driven Cortical Circuit. *The Journal of Neuroscience* 33: 18855, 2013.
- Yuan J, Gong H, Li A, Li X, Chen S, Zeng S, and Luo Q.** Visible rodent brain-wide networks at single-neuron resolution. *Frontiers in Neuroanatomy* 9: 2015.
- Zaytsev YV, Morrison A, and Deger M.** Reconstruction of recurrent synaptic connectivity of thousands of neurons from simulated spiking activity. *Journal of computational neuroscience* 39: 77-103, 2015.
- Zhang W, and Bruno RM.** High-order thalamic inputs to primary somatosensory cortex are stronger and longer lasting than cortical inputs. *Elife* 8: e44158, 2019.
- Zucker RS, and Regehr WG.** Short-term synaptic plasticity. *Annual review of physiology* 64: 355-405, 2002.